2007-10-24

Error Sensor Placement for Active Control of an Axial Cooling Fan

Benjamin M. Shafer
Brigham Young University - Provo

ERROR SENSOR PLACEMENT FOR ACTIVE CONTROL OF AN AXIAL COOLING FAN

by

Benjamin Michael Shafer

A thesis submitted to the faculty of

Brigham Young University

in partial fulfillment of the requirements for the degree of

Master of Science

Department of Physics and Astronomy

Brigham Young University

December 2007

BRIGHAM YOUNG UNIVERSITY

GRADUATE COMMITTEE APPROVAL

of a thesis submitted by

Benjamin M. Shafer

This dissertation has been read by each member of the following graduate committee and by majority vote has been found to be satisfactory.

Date	Kent L. Gee, Chair
Date	Scott D. Sommerfeldt
Date	Craig C. Smith

BRIGHAM YOUNG UNIVERSITY

As chair of the candidate's graduate committee, I have read the thesis of Benjamin M. Shafer in its final form and have found that (1) its format, citations, and bibliographical style are consistent and acceptable and fulfill university and department style requirements; (2) its illustrative materials including figures, tables, and charts are in place; and (3) the final manuscript is satisfactory to the graduate committee and is ready for submission to the university library.

_____ _____

Date

Kent L. Gee
Chair, Graduate Committee

Accepted for the Department

_____

J. Ward Moody
Graduate Coordinator

Accepted for the College

_____

Thomas W. Sederberg
Associate Dean, College of Physical and Mathematical Sciences

ABSTRACT

ERROR SENSOR PLACEMENT FOR ACTIVE CONTROL OF AN AXIAL COOLING FAN

Benjamin M. Shafer

Department of Physics and Astronomy

Master of Science

Recent experimental achievements in active noise control (ANC) for cooling fans have used near-field error sensors whose locations are determined according to a theoretical condition of minimized sound power. A theoretical point source model, based on the condition previously stated, reveals the location of near-field pressure nulls that may be used to optimize error sensor placement. The actual locations of these near-field pressure nulls for both an axial cooling fan and a monopole loudspeaker were measured over a two-dimensional grid with a linear array of microphones. The achieved global attenuation for each case is measured over a hemisphere located in the acoustic far field of the ANC system. The experimental results are compared to the theoretical pressure null locations in order to determine the efficacy of the point source model. The results closely matched the point source model with a loudspeaker as the primary source, and the

sound power reduction was greatly reduced when error sensors were placed in non-ideal locations.

A weakness of the current near-field modeling process is that a point monopole source is used to characterize the acoustic noise from an axial cooling fan, which may have multipole characteristics. A more complete characterization of fan noise may be obtained using a procedure based on the work of Martin and Roure [J. Sound Vib. **201** (5), 577–593 (1997)]. Pressure values are obtained over a hemisphere in the far field of a primary source and the contributions from point source distributions up to the second order, centered at the primary source, may be calculated using a multipole expansion. The source information is then used in the aforementioned theoretical near-field calculation of pressure. The error sensors are positioned using the complete fan characterization. The global far-field attenuation for the multipole expansion model of fan noise is compared to that of previous experiments. Results show that the multipole expansion model yields a more accurate representation the near field, but is not successful in achieving greater sound power reductions in the far field.

ACKNOWLEDGMENTS

I thank the following individuals and organizations for their invaluable assistance and encouragement:

- Dr. Kent Gee for the many hours of his time spent helping me gain a more complete understanding of acoustics and develop the ability to research on a professional level
- Dr. Scott Sommerfeldt for his wealth of knowledge in acoustics and noise control and for setting aside time in his schedule to share this knowledge with me and help me apply it to my research
- Dr. Craig Smith for helping me understand the principles of signal processing and analysis and for teaching me the importance of obtaining a conceptual understanding of electrical and physical phenomena
- Brigham Young University acoustics faculty, graduate students, undergraduate students, especially Dr. Tim Leishman, Micah Shepherd, Ryan Chester, Buye Xu, Cole Duke, Connor Duke, and Emily Egan for helping me make my measurements and for their encouragement and interest in my research.
- My wife Whitney, for the sacrifices she made to care for me and support me in completing the research and thesis work, and my boys, Joel and Kadin, for giving me a reason to be happy to come home at the end of a long day.

TABLE OF CONTENTS

LIST OF TABLES

LIST OF FIGURES

CHAPTER 1

INTRODUCTION

1.1. SCOPE

The work of this thesis is focused on the active cancellation of unwanted noise from cooling fans. Active noise control (ANC) requires the correct use of error sensors, which may be located using various methods. Many methods for near-field error sensor placement require a physical model of the primary noise source. One modeling method currently used for near-field error sensor placement, point-source modeling, is analyzed experimentally. A new model of fan noise based on a distribution of point sources is presented, analyzed, and compared to the point-source model.

1.2. NOISE AND NOISE CONTROL

The industrial community is constantly making progress in the design of the most common machinery and equipment currently used in both the workplace and at home. Computers, for example, are continuously being redesigned for faster and more efficient task management and computation. Many such commonplace appliances have been similarly engineered. Due to the generation of heat by the fast-pace mechanisms in computers and other appliances, it is necessary to integrate cooling devices, such as fans, into the design and construction of these appliances (See Figure 1-1). However, the cooling fans that are used to keep equipment from overheating create acoustic noise that is both difficult to suppress and annoying to hear.

Figure 1-1: A common axial cooling fan installation (left side of the machine) inside a computer case[1].

1.2.1. ACOUSTIC NOISE

Any device that causes the surrounding fluid to vibrate radiates energy in the form of sound. The ability of the human ear to perceive sound allows a listener to experience an amalgam of both positive and negative emotions. The type of emotion that a listener will experience when subjected to a given sound depends on the nature of the sound that is perceived. For example, most sounds that are born from music and speech are pleasant to hear and create a positive effect on human emotion[2]. Noise from machinery and electronic equipment is often piercing and annoying to hear[2,3].

Acoustic noise is a continuing source of concern in the home, industry, and community. In the home, acoustic noise is mostly the cause of annoyance to the listener. In industry and the community, noise can be annoying and, when sufficiently high in amplitude, damaging to the human ear. For this and other reasons, many standards have been written and designed that address issues in the causation,

duration, and cessation of various types of noise[3]. The negative effects of acoustic noise are evident in both the home and the workplace. Studies have shown that human performance can be negatively affected by acoustic noise. Thus, certain criteria have been developed in order to correctly classify, quantify, and suppress it[2,3].

1.2.2. FAN NOISE: GENERAL CONCEPTS

As stated in Section 1.1 of this thesis, fan noise is an increasingly important problem as technology advances. Cooling fans are required accessories in many electronic devices that create heat. Small axial fans are commonly used in such applications because of their compact dimensions and ability to efficiently move air through an enclosure[4–7]. The movement of air through the enclosure surrounding the fan and its individual components creates acoustic noise that is both discrete (tonal) and broadband[8–10].

The individual parts of an axial fan are the rotor blades, hub, wheel rotor

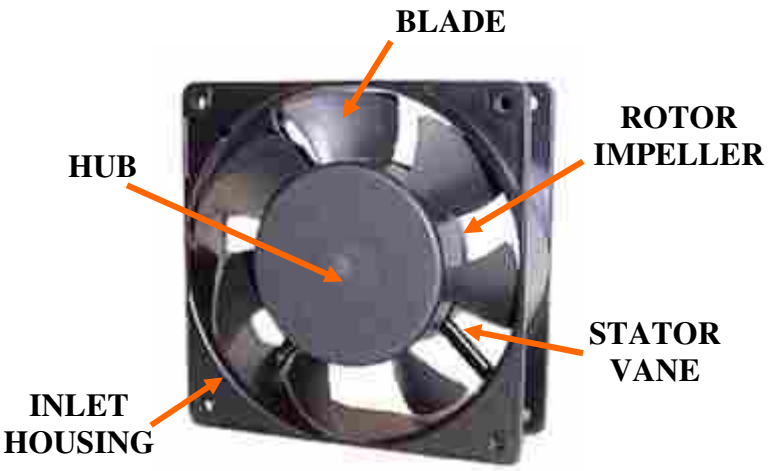

Figure 1-2: A diagram of the most common type of axial cooling fan currently used in computer-type applications[11].

impeller, inlet/outlet housing, and stator vanes or support struts[9]. An axial cooling fan is photographed and labeled in Figure 1-2. Many fans are designed with electronics for tachometer output and pulse width modulation. The tachometer signal may be used as a reference signal for monitoring the speed of the fan rotor. Pulse width modulation allows for control of the fan speed. Each part of the cooling fan is designed to optimize the movement of air from the inlet side of the fan to the outlet.

Although there are many advantages that result from the use of the design of these small air-moving devices, one disadvantage is that they create both broadband and tonal noise. For most axial cooling fans the noise that they create is a cause of annoyance to the listener. The human ear is generally more sensitive to discrete tones than broadband noise[2,9]. Axial fans produce both broadband noise and discrete tones with harmonics and can thus cause discomfort to people within an audible distance to the fan. Also, because of the sensitivity of the human ear to discrete tones, it does not require nearly as much energy for the tonal noise that the fan produces to be perceived as loud to the listener[3].

1.2.3. NOISE CONTROL FOR FANS

The frequency range of noise-producing sources is an important factor when determining how to suppress the radiated noise. An acoustic source that produces high frequencies can be suppressed using passive control techniques—or techniques that do not require the use of additional acoustic sources. Many passive control devices, such as acoustic tile or insulation, are only effective at high frequencies[12–14]. For instance, when a broadband acoustic source is placed inside of an enclosure that is lined with thick absorbing materials, the higher frequencies that the source

produces can be made relatively inaudible to the listener outside the enclosure. Low-frequency noise is much more difficult to passively suppress than high-frequency noise because the wavelength of low-frequency noise is usually large relative to the source, its surroundings, and the thickness of most acoustically absorbing materials[13,14].

Because of the frequency range of a cooling fan and spatial constraints in its installation, it is not possible to control fan noise using a solely passive technique. Some devices with cooling fans are so compact that passive control devices cannot physically be installed to suppress the fan noise. For example, the fan used to cool the CPU of a computer cannot be covered by acoustically absorbing material because a great amount of airflow is needed for the cooling process.

Active noise control (ANC) is an excellent candidate for the cancellation of fan noise[15]. ANC systems are primarily used to attenuate low-frequency noise, well within the spectrum of fan noise. Also, an ANC system does not require a large geographical area, especially when compared to the amount of passive absorbing material required to attenuate similar frequencies. An ANC system does, however, require the use of hardware, such as a Digital Signal Processor (DSP) and many other electronic filters and amplifiers.

1.3. ACTIVE FAN NOISE CONTROL

1.3.1. ACOUSTIC COUPLING

Global attenuation of acoustic energy from a primary noise source can be achieved by means of acoustic coupling[16,17]. When a source radiates acoustically, the energy is propagated into the surrounding environment. Assuming that the radius of

this source is small compared to a wavelength of the acoustic wave, the source radiates like a point monopole source. Suppose a second acoustic point source is placed in close proximity to the primary source. Assuming that the distance between the sources is small relative to a wavelength of sound, the sources will couple acoustically. Depending on the phase of the second acoustic source, a portion of the radiated acoustic energy from the two sources will be transferred between them instead of propagated out into the surroundings. If both point sources have the same magnitude source strength and the second source is completely out of phase with the first, they will couple to create an acoustic dipole, which radiates much less acoustic energy than a single point monopole source with the same source strength[18].

The coupling of a general distribution of acoustic sources may be directly applied in ANC for cooling fans. In order to actively control the noise from a cooling fan, the control sources must be placed as close as possible to the fan to create an environment where, with appropriate source strength magnitudes and phases, the sources couple acoustically. As the control sources properly couple with the fan, the radiated sound power of the fan becomes attenuated globally.

1.3.2. ERROR SENSORS

The objective of the ANC system is to minimize the acoustic signal at the location of one or more error sensors[16,19]. In ANC for an axial cooling fan, the control actuators are usually loudspeakers and the error sensors are usually microphones. The signal that the microphone receives is due to the steady-state acoustic effects of the primary noise source and the control actuators as well as the broadband noise floor of the environment in which the ANC system is operating. The fans used for this thesis

were tested in an anechoic environment so that the background noise was minimal. In the signal processing for any error sensor signal, it may be assumed that the error sensor has a linear discrete-time relationship with the primary noise source and control actuators.

An ANC system is primarily used as a tool to reduce the noise radiated from a primary noise source. Error sensors are an essential component of the ANC system and the proper placement of error sensors in an ANC system can result in better active control of the primary noise source. For a more compact ANC system, the error sensors may be placed in the acoustic near field of the primary noise source. The ANC system used for this thesis was implemented with a feed-forward filtered-x algorithm.

1.4. THESIS ORGANIZATION

The work of this thesis has been organized into chapters and sections. The following list provides the name of each subsequent chapter title and a description of the material found therein:

- Chapter 2, Error Sensor Placement—the principles of acoustic coupling and ANC as they apply to the location of error sensors for minimization of sound power.
- Chapter 3, Fan Noise—a characterization of fan noise using point source distributions and previous methods for modeling cooling fans to determine error sensor locations in ANC.

- Chapter 4, Multipole Expansions—an explanation of how to use multipole expansions to determine the relative point source distributions that may be used to model an axial cooling fan.
- Chapter 5, Near-field Pressure Mapping and Global Attenuation—A verification of near-field error sensor placement and the effects that it has on the achievable global sound power attenuation of the primary noise source.
- Chapter 6, Multipole Expansions and Fan Noise ANC—the experimental results comparing the multipole expansion method of error sensor placement to the point source method.
- Chapter 7, Conclusions—a discussion of the results as they apply to ANC for axial cooling fans and new methods for optimizing error sensor placement.

CHAPTER 2

ERROR SENSOR PLACEMENT

2.1. ACOUSTIC COUPLING

Most of the current modeling practices in minimization of primary source sound power for the purpose of correctly placing near-field error sensors require that both the primary and secondary sources be modeled as point monopoles[20–22]. Modeling the acoustic coupling between point sources is much more straightforward than distributed source modeling. Point monopole sources may be used to model acoustic radiation from many different types of sources. A small loudspeaker, for example, may be modeled as a point source from the lowest frequency at which it will respond up to frequencies that correspond to wavelengths that are much larger than the radius of the loudspeaker. As the primary source modeling method varies, the correct placement of the error sensor varies. In this chapter, all acoustic sources are modeled as point monopoles.

The acoustic pressure from a single-frequency time harmonic spherical wave is calculated as:

$$\hat{p}(r,t) = \frac{\hat{A}}{r} e^{-i(\omega t - kr)} \tag{2-1}$$

where $\hat{A}$ is the complex pressure amplitude, r is the distance from the center of the source to the measurement point, ω is the angular frequency in radians, t is the time in seconds, and k is the wave number (m^{-1}). The complex pressure amplitude may also be calculated using Euler's equation. An approximation of this pressure equation may apply if the

radius of the source is small when compared to a wavelength of sound. When this approximation is valid the equation for complex pressure amplitude is calculated as,

$$\hat{A} = -i\frac{\rho_0 c\hat{q}k}{4\pi}, \tag{2-3}$$

where $\hat{q}$ is the complex source strength, ρ_0 is the atmospheric density, and *c* is the speed of the acoustic wave.

A thorough understanding of acoustic coupling and its role in global noise control is necessary to correctly position any of the error sensors that are used as a part of the ANC system. A primary noise source acoustically couples to a secondary source, or control actuator, only if the secondary source is sufficiently close to the primary source relative to a wavelength of sound. Optimization of global sound power control of the primary source may be achieved when more than one secondary source is used. A more rigorous explanation of this principle may be described using mathematics. If the primary source has a complex pressure described by (2-1) and (2-3), it is a point monopole source. If a secondary point source is placed a distance, *d*, from the primary source and has a complex source strength, $\hat{q}_s$, the acoustic pressure at the primary source due to its own pressure and the pressure of the secondary source may be calculated as[16]:

$$\hat{p}_p(a,t) = -i\frac{\rho_0 ck^2}{4\pi}\left(\left|\hat{q}_p\right|\frac{e^{ika}}{ka}e^{-i\psi} + \left|\hat{q}_s\right|\frac{e^{ikd}}{kd}e^{-i\varphi}\right)e^{-i\omega t}. \tag{2-4}$$

The sound power for the primary source due to coupling between the two sources is:

$$W_p = \frac{\rho_0 ck^2}{8\pi}\left|\hat{q}_p\right|^2\left(\frac{\sin ka}{ka} + \frac{\left|\hat{q}_s\right|}{\left|\hat{q}_p\right|}\frac{\sin\left[kd-(\varphi-\psi)\right]}{kd}\right). \tag{2-5}$$

A similar expression may be obtained for the sound power of the secondary source as the sources couple acoustically. Using the principle of superposition, the sound power of both the primary and secondary sources due to acoustic coupling may be calculating using this expression:

$$W_{tot} = \frac{\rho_0 c k^2}{8\pi}\left|\hat{q}_p\right|^2\left(1+\left(\frac{\left|\hat{q}_s\right|}{\left|\hat{q}_p\right|}\right)^2+2\frac{\left|\hat{q}_s\right|}{\left|\hat{q}_p\right|}\frac{\sin kd}{kd}\cos(\varphi-\psi)\right) \tag{2-6}$$

Examination of (2-6) reveals that the total sound power of the coupled system is minimized when

$$\cos(\varphi-\psi) = -1, \tag{2-7}$$

The optimum source strength, $\hat{q}_{so}$, of the secondary source may also be calculated for the condition of minimized total sound power using the following equation:

$$\hat{q}_{so} = +\left|\hat{q}_p\right|\frac{\sin kd}{kd}. \tag{2-8}$$

Including these minimization parameters in the calculation of minimized total sound power yields the following equation:

$$W_{\min} = \frac{\rho_0 c k^2}{8\pi}\left|\hat{q}_p\right|^2\left(1-\left(\frac{\sin kd}{kd}\right)^2\right). \tag{2-9}$$

The total sound power may be minimized further by placing the secondary sources as close to the primary source as possible, thus reducing the distance, *d*, between sources. In ANC, certain control actuator configurations produce better results than others depending on the number of control actuators used for control. For example, a study by Gee and Sommerfeldt showed that an ANC system with four symmetrically located control actuators surrounding a primary source achieved the greatest global attenuation[20].

2.2. ERROR SENSOR PLACEMENT FOR MINIMIZED SOUND POWER

When sound power is minimized the pressure field in the near field of the primary source may be mapped using the superposition of the pressure from the primary source and the pressures of each actively controlled actuator whose source strength has been optimized to minimize the sound power of the primary source. The map of the pressure field in the plane of the error sensors reveals the location of pressure nulls. These pressure nulls may be used to place the error sensors, whose signals are used in the ANC system to drive the acoustic pressure at each sensor location to zero.

As an example, suppose that a single point monopole source is radiating acoustic energy (Figure 2-1). When this source is actively controlled with one secondary control actuator, the resulting acoustic pressure radiated by the coupled sources will closely resemble an acoustic dipole. Figure 2-2 is an illustration of this exact case. When the

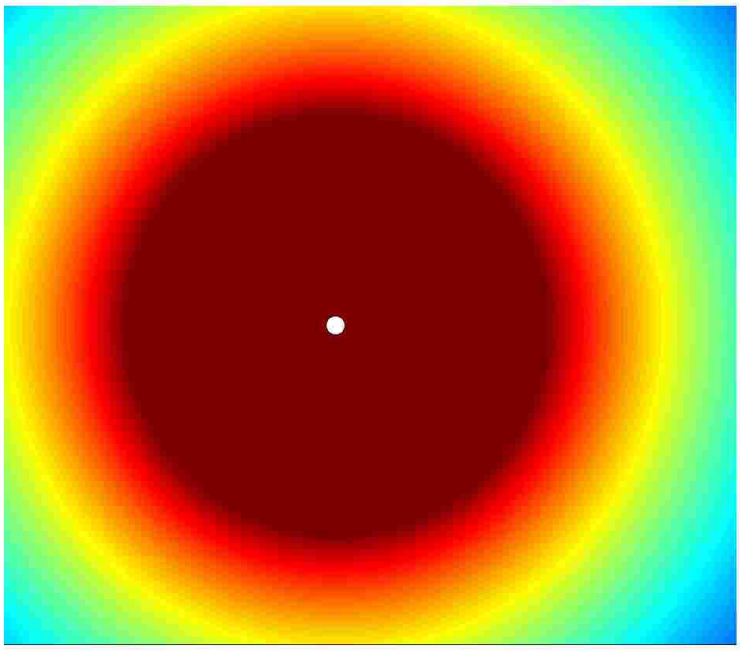

Figure 2-1: The radiated pressure field (dB ref. 20μPa) in the plane of a single point monopole source. The white circle marks the source location.

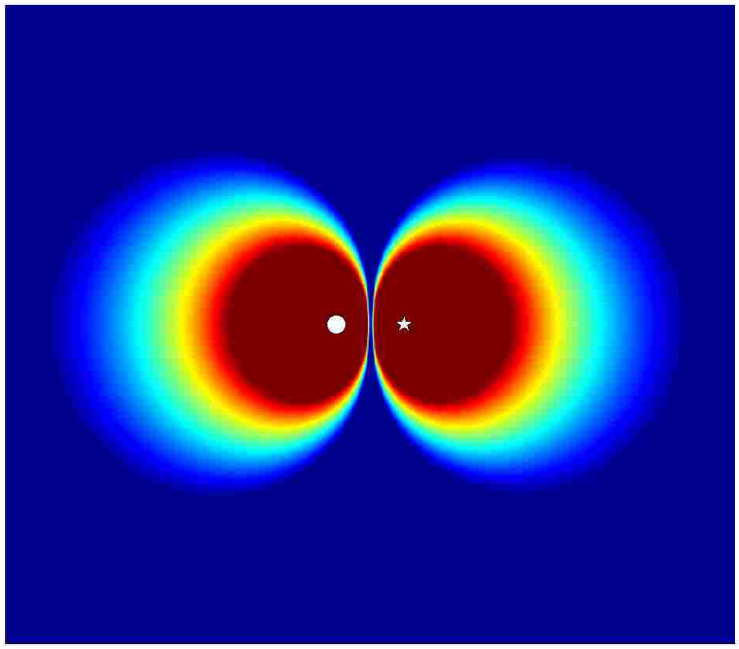

Figure 2-2: The radiated pressure field (dB ref. 20μPa) in the plane of ANC resulting in acoustic coupling between a single primary and secondary source for minimization of primary source sound power. The white circle and star mark the locations of the primary and secondary sources.

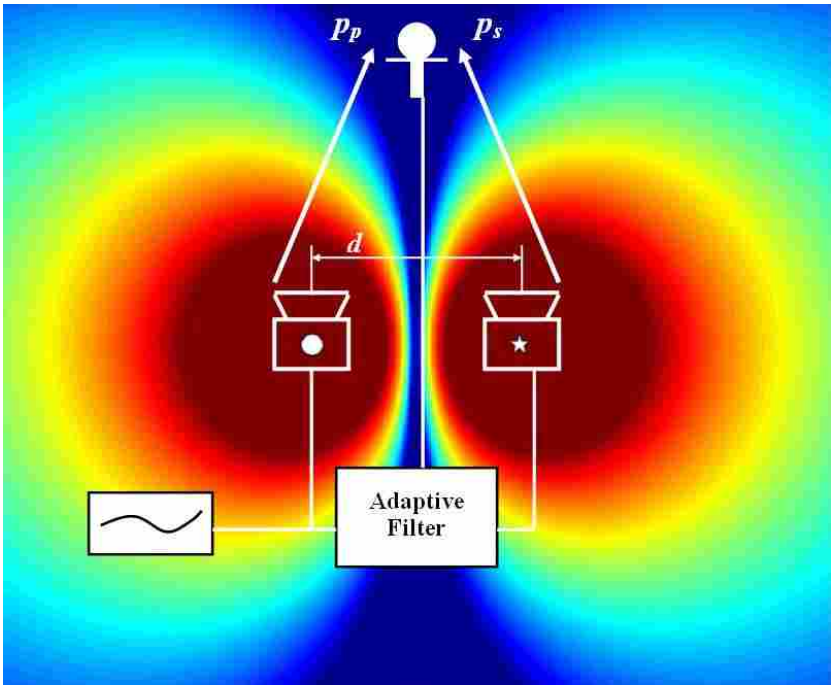

Figure 2-3: The near-field radiated pressure (dB ref. 20μPa) in the plane of ANC for the case represented in Figure 2-2. The variables p_p and p_s represent the primary and secondary source pressures.

pressure field that results from this acoustically coupled system is mapped, a pressure null is revealed halfway between the two sources. A near-field view of the radiated pressure for this case is shown in Figure 2-3, as well as a simple diagram of the active control system. The best location for an error sensor, whose signal is being driven to zero, is anywhere along this central pressure null.

2.3. DISCUSSION OF ERROR SENSOR PLACEMENT METHODS

The first decision that must be made in error sensor placement is whether to put the sensors in the acoustic near-field or far-field of the primary noise source. Various authors, such as Kempton[23] and Martin and Roure[34], place the error sensors in the acoustic far field of the primary source. Kempton's method of arranging the control sources and error sensors is complex and requires extensive computation. Martin and Roure proposed to place the control actuators in the near field of the primary source while the error sensors remained in the far field. The method of error sensor placement for this experiment was difficult as well.

Other authors, such as Gee and Sommerfeldt[21], Berry *et. Al*[25], and Qiu *et. Al*[26] suggest that it is preferable to use near-field and not far-field error sensors for minimization of sound power. These authors suggest that it is more desirable and more practical to use a compact active control system. Also, there is a tendency for the far-field error sensors to reduce the radiation of sound mostly in the direction of the sensor, thus reducing the overall global attenuation of the radiated sound. Also, error sensors located at acoustically large distances from the control actuators have large acoustic delays.

Near-field error sensors, therefore, are more desirable for use in an ANC system and are, therefore, used in the work of this thesis.

As previously stated in this chapter, the placement of error sensors has been modeled previously using point monopole sources to map the pressure field. Using this method, Gee and Sommerfeldt[21] achieved significant global attenuation of the fan source. According to their experiment, the control actuator configuration that gave them the best global attenuation, four control actuators located symmetrically around the fan, still did not achieve the amount of global attenuation predicted. Quinlan[22] used one secondary source to control the noise from a fan and achieved comparable global attenuation on just the BPF of the fan. Gerard *et. al*[27] used, instead of a point monopole source, an inverse aeroacoustic model to characterize the dipole-type noise of an automotive fan. The model is explained in more detail in Section 3.3. The global attenuation they achieved was more closely matched with the attenuation they predicted using the inverse aeroacoustic model. This last example illustrates the need to obtain a more complete representation of fan noise when determining the location of near-field error sensors.

CHAPTER 3

FAN NOISE

3.1. THE FREQUENCY SPECTRUM OF FAN NOISE

3.1.1. DISCRETE NOISE

Much of the discrete portion of noise from an axial fan is caused by the interaction of air-flow with the blades of the fan[10]. As each fan blade passes through any arbitrary point, the particles of air at that point experience a force, or impulse. The forces acting on the air particles create periodic impulses as each of the fan blades rotate around the hub of the fan. The periodic impulses caused by the motion of the fan blade create the fundamental, or blade passage frequency (BPF), of the fan. This fundamental frequency varies depending on the speed of the fan as well as the number of fan blades. The spectrum of a 60-mm fan is shown in Figure 3-1.

The periodic interaction of air with the fan blades gives rise to various harmonics of the BPF as well. The number of harmonics that rise above the broadband levels varies depending on the construction of the fan blade as well as the operating speed of the fan[29]. Another contributor to the tonal noise of a fan is the interaction of the fan blade with the stator vanes.

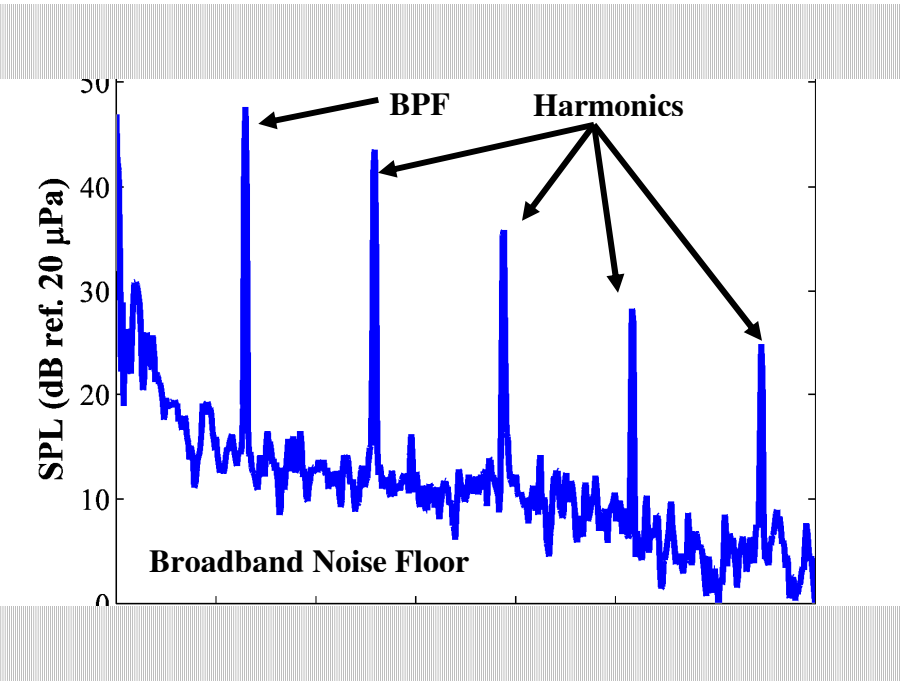

Figure 3-1: The measured power spectrum of a 60-mm fan. The measurement was made 1.5 m from the fan using an on-axis ½" ICP microphone.

3.1.2. BROADBAND NOISE

The broadband noise created by cooling fans varies with different types of fans and is caused by several fan-flow interaction mechanisms. First, there is an unsteady pressure on each blade surface. This unsteady pressure is caused by the boundary layer of the fan turbulence. There is also vortex shedding from the trailing edge of each blade. Much of the trailing edge vortex shedding is unsteady in nature. Lastly, there are random airflow interactions on the inlet side of the fan, resulting in a broadband noise spectrum[30]. All of aforementioned causes of broadband noise are either the effect of, or create turbulence. The acoustic energy radiated by turbulence is random and always has a broad frequency spectrum.

For axial cooling fans the broadband noise radiates at sound pressure levels that can be far below those of the BPF and its related harmonics. In contrast to the

axial fan, the spectrum of a centrifugal fan appears uniform, or broadband[10]. Although there are more discrete tones in the spectrum of the centrifugal fan, the energy of the tones is far less than for the axial fan. For the centrifugal fan the BPF is much less prominent in the noise spectrum than for the axial fan. The significant increase in acoustic energy of the tonal portion of an axial cooling fan's spectrum, when compared to the broadband portion of the same spectrum, make it a much better candidate for feed-forward ANC than the centrifugal fan[6].

3.2. MULTIPOLE CHARACTERISTICS OF FAN NOISE

Studies have shown that fan noise may be categorized as monopole, dipole, or quadrupole radiation[31]. Neise provides a mathematical proof of this concept, using the wave equation. He developed a flow diagram that illustrates the different sources of acoustic radiation from a fan and their relative sources. Neise's fan noise flow diagram is shown in Figure 3-2.

3.2.1. MONOPOLE CHARACTERIZATION

The monopole noise from a fan is discrete, or tonal, in nature. As noted in Chapter 1, tonal noise is the easiest for the human ear to detect. The blade thickness of the fan creates periodic volume displacements in the flow medium, air in this case, as the blades rotate around the geographic center of the fan[31]. The forces involved in these volume displacements are caused by the steady rotation of the fan in a steady flow field. The monopole contribution of a fan noise is small compared to the contribution from other fan noise mechanisms and depends largely on its installation. When a solid object is placed either on the inlet or outlet side of the cooling fan, the

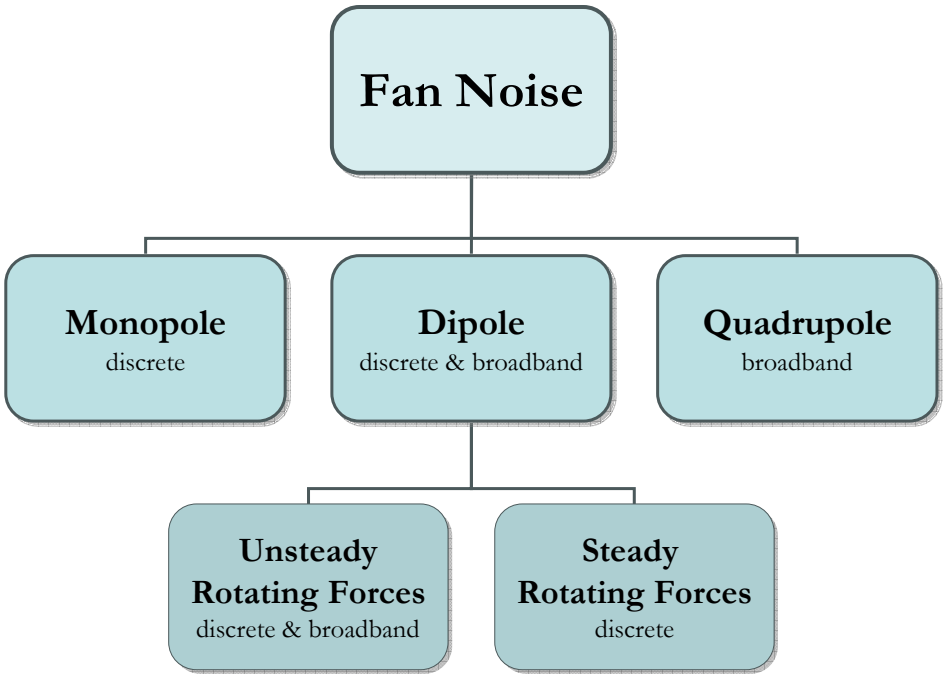

Figure 3-2: A flow diagram for fan noise characterization (taken from Ref. 32).

acoustic field due to the monopole contribution of the fan noise may change drastically. The changes in monopole radiation of the fan make it difficult to more accurately model tonal noise from the fan.

3.2.2. DIPOLE CHARACTERIZATION

Both steady and unsteady rotating forces in a cooling fan cause noise that may be characterized as a dipole[31]. Steady rotating forces were discussed in the previous section. The forces that exist from the interaction of the flow with a solid surface are unsteady in nature. These unsteady forces create both broadband and tonal noise and are the primary contributors to the blade passing frequency (BPF) and broadband noise floor of the fan. The displacement of the entire moving surface, i.e. the blades, also causes dipole-type acoustic radiation.

3.2.3. QUADRUPOLE CHARACTERIZATION

The broadband component of fan noise arises from turbulent flow. Turbulent flow is evident in the inlet air-flow, inside the fan enclosure, and is produced as the air-flow causes a wake behind the fan blade[29]. The pressure fluctuations due to turbulent flow have a random variation throughout all locations within the flow. Work by Mongeau and Quinlan showed that most of the broadband energy of the fan used in their study was radiated near the BPF and its harmonics[32]. Noise due to turbulent flow may be modeled as a single acoustic quadrupole or a distribution of quadrupoles around the fan[33].

3.3. POINT-SOURCE MODELING AND FAN ANC

Although there are many ways to control noise from axial fans both passively and actively, this thesis will focus on the active control of fan noise. Previous successes in active control for fans have demonstrated the possibilities of actively controlling the BPF as well as the second and third harmonics. Gee and Sommerfeldt achieved global attenuation of the BPF and up to the fourth harmonic of an 80-mm axial cooling fan using four near-field error sensors and four control actuators[21]. They achieved 10.1 dB global attenuation of the BPF (370 Hz) of the fan, and 16.1 dB at the second harmonic. Quinlan had one error sensor and one control actuator in his experiment[22]. He was able to achieve a sound power reduction of 10.2 dB for his fan with a BPF of 216 Hz. The error sensor locations for both of these experiments were determined by modeling the fan as a point monopole source.

Gerard *et al* made ANC simulations based on an inverse aeroacoustic model of fan noise[27]. Fan noise may be characterized using aeroacoustic equations for both the

uniform (steady) and non-uniform (unsteady) flow conditions of the fan. These equations were used in a time series expansion to find the dipole strength distribution over the area of the fan. The dipole distribution of the fan was used in an active control simulation and the results are discussed in Section 2.3.

As discussed in the previous section, many experiments in the active cancellation of fan noise have assumed that a fan can be modeled as a point monopole source, especially when installed in an enclosure. These models limit the type and causes of fan noise discussed previously in this chapter to a single monopole component. Noise from a fan is described as an acoustic multipole with contributions from monopole-, dipole-, and quadrupole-type noise. It may be argued that when a fan is placed in an enclosure it radiates primarily like an acoustic monopole. How much of the contribution from higher order sources—such as dipoles and quadrupoles—is diminished when the fan is installed in such a manner has not been proven experimentally, however,. The question of how much contribution exists from the higher order sources in a fan is answered in Chapter 6 of this thesis.

CHAPTER 4

MULTIPOLE EXPANSIONS

4.1. A MATHEMATICAL MODEL OF FAN NOISE

The knowledge of how a cooling fan radiates acoustic energy is necessary when attempting to suppress such sound actively. Some of the modeling procedures used in fan noise ANC assume that the fan radiates as a point monopole source, similar to a loudspeaker in the same frequency range. However, because of the complexity of the physical phenomena governing cooling fan noise, as discussed in Chapter 3, in comparison to a simple loudspeaker, a complete model of fan noise is more difficult to acquire.

Various methods have been used to model fan noise in past studies. Three of the most common methods include measurement analysis[34–36], numerical simulation[37–39], and mathematical modeling[41–43]. The procedure for calculating the minimized sound power (Chapter 2, 5) requires that the primary source be modeled as a point monopole source or a distribution of point sources. Distributions of point sources are relatively simple to model using mathematics, especially if multipoles such as monopoles, dipoles, and other traditionally defined source distributions can characterize them.

As discussed in Chapter 3 of this thesis, noise from an axial cooling fan may be characterized as monopole, dipole, and quadrupole. Therefore, a mathematical procedure may be a more efficient way of characterizing fan noise than the two other method

previously mentioned. Due to the multipole nature of fan noise, a multipole expansion (ME) is a viable modeling procedure. The theoretical basis for an ME requires the knowledge of spherical harmonics and their relationship to multipole point source distributions.

4.2. SPHERICAL HARMONICS

A spherical coordinate system may be defined for any source or distribution of sources. If the source is centered at the origin of this coordinate system the radiated acoustic pressure from this source may be solved using the Helmholtz equation in spherical coordinates,

$$\frac{1}{r^2}\frac{\partial}{\partial r}\left(r^2\frac{\partial \hat{p}(r,\theta,\varphi)}{\partial r}\right)+\frac{1}{r^2\sin\theta}\frac{\partial}{\partial \theta}\left(\sin\theta\frac{\partial \hat{p}(r,\theta,\varphi)}{\partial \theta}\right)+ \frac{1}{r^2\sin^2\theta}\frac{\partial^2 \hat{p}(r,\theta,\varphi)}{\partial \varphi^2}+k^2\hat{p}(r,\theta,\varphi)=0, \tag{4-1}$$

where $\hat{p}$ is the complex pressure, r is the distance from the origin to a measurement point, k is the acoustic wave number, θ is the polar angle, and φ is the azimuthal angle. The solution to this equation is valid anywhere outside the smallest sphere centered at the origin of the coordinate system that contains the source or source distribution. In spherical coordinates the solution may be expressed as the following summation:

$$\hat{p}(r,\theta,\varphi)=\left[\sum_{n=0}^{\infty} h_n^{(1)}(kr)\sum_{m=-n}^{n} \mathrm{Y}_n^m(\theta,\varphi)\right]e^{-i\omega t}, \tag{4-2}$$

where $h_n^{(1)}(kr)$ is the n^{th} order spherical Hankel function of the first kind which corresponds to the outgoing pressure waves, and $\mathrm{Y}_n^m(\theta,\varphi)$ are the spherical harmonics corresponding to the polar and azimuthal dependences of the acoustic pressure for an

infinite number of m and n indices. Spherical harmonics are defined in the following manner,

$$\mathrm{Y}_n^m(\theta,\varphi) = \hat{A}_{mn}\mathrm{P}_n^m(\cos\theta)e^{\pm im\varphi}, \tag{4-3}$$

with the following orthogonality relationship

$$\int_0^{2\pi}\int_0^{\pi} \mathrm{Y}_n^{m*}(\theta,\varphi)\mathrm{Y}_k^l(\theta,\varphi)\sin\theta\, d\theta\, d\phi = \delta_{nk}\delta_{ml}, \tag{4-4}$$

where $\delta_{nk} = \delta_{ml} = 1$ for $n = k$ and $m = l$ and $\delta_{nk} = \delta_{ml} = 0$ for $n \neq k$ and/or $m \neq l$ [44]. The variable $\hat{A}_{mn}$ in Eq. (4-3) represents the complex spherical harmonic coefficients, $\mathrm{P}_n^m(\cos\theta)$ is the associated Legendre polynomial for the m^{th} and n^{th} index, and the exponential $e^{\pm im\varphi}$ is more commonly expressed as the linear combination of $\cos(m\varphi)$ and $\sin(m\varphi)$. The Condon–Shortley phase of $(-1)^m$ is included in the spherical harmonic coefficient $\hat{A}_{mn}$. Theoretically, the pressure may be expanded to an infinite order n, as illustrated in Eq. 4-2. In practice the expansion must be truncated to a finite order. Using notation formerly described and truncating the sum to the order N, the solution from Eq. (4-3) may be expanded into a series of spherical harmonics[23]:

$$\begin{aligned}\hat{p}(r,\theta,\varphi) = &\sum_{n=0}^{N}\hat{h}_n^{(1)}(kr)\sum_{m=0}^{n}\hat{A}_{mn}\mathrm{P}_n^m(\cos\theta)\cos(m\varphi) + \\ &\sum_{n=0}^{N}\hat{h}_n^{(1)}(kr)\sum_{m=1}^{n}\hat{B}_{mn}\mathrm{P}_n^m(\cos\theta)\sin(m\varphi)\end{aligned} \tag{4-5}$$

An $e^{-i\omega t}$ time dependence is assumed in this as well as the following equations. The expansion used for this thesis was calculated up to the second order. The solution illustrated in Eq. 4-5 may be expressed for a finite order in matrix form with the following equation:

$$\hat{\mathbf{P}} = \hat{\mathbf{T}}\hat{\mathbf{A}} \tag{4-6}$$

where $\hat{\mathbf{P}}$ is a vector of complex pressure values at measurement points on a sphere surrounding the noise source, $\hat{\mathbf{T}}$ is a matrix of the spherical Hankel functions and spherical harmonics, and $\hat{\mathbf{A}}$ is a vector of complex spherical harmonic coefficients. If the complex pressure is measured over a sphere outside the volume containing the source, equation (4-6) may be solved for the spherical harmonic coefficients up to the n^{th} order by taking the inverse of the matrix $\hat{\mathbf{T}}$. If $\hat{\mathbf{T}}$ is not a square matrix, the inverse may not be possible to invert. This problem may is resolved by using a least-squares solution to the equation[45,46]. The least-squares solution is calculated as

$$\hat{\mathbf{A}} = \left[\hat{\mathbf{T}}^{\mathbf{H}}\hat{\mathbf{T}}\right]^{-1}\hat{\mathbf{T}}^{\mathbf{H}}\hat{\mathbf{P}}, \tag{4-7}$$

where the superscript *H* denotes a Hermitian transpose. The Hermitian transpose is defined as the complex conjugate of a normal matrix transpose.

Each spherical harmonic represents a specific type of multipole for the order *n* and *m*. For example, the multipole that represents the $m = 0$, $n = 0$ spherical harmonic is a monopole source. The zeroeth order multipole is a monopole, the first order multipoles are dipoles, and the second order multipoles are quadrupoles. The calculations for this thesis include terms up to second order multipoles. Figure 4-1 shows the directivity plots of the spherical harmonics up to the second order. Table 4-1 labels each spherical harmonic with a name, according to the multipole type. The $m = 0$, $n = 2$ spherical harmonic is termed a pseudo-longitudinal quadrupole because it has a point source distribution similar to a longitudinal quadrupole, but with an additional source at the origin. Although the $m = 2$, $n = 2$ multipole is a lateral quadrupole, the distance between

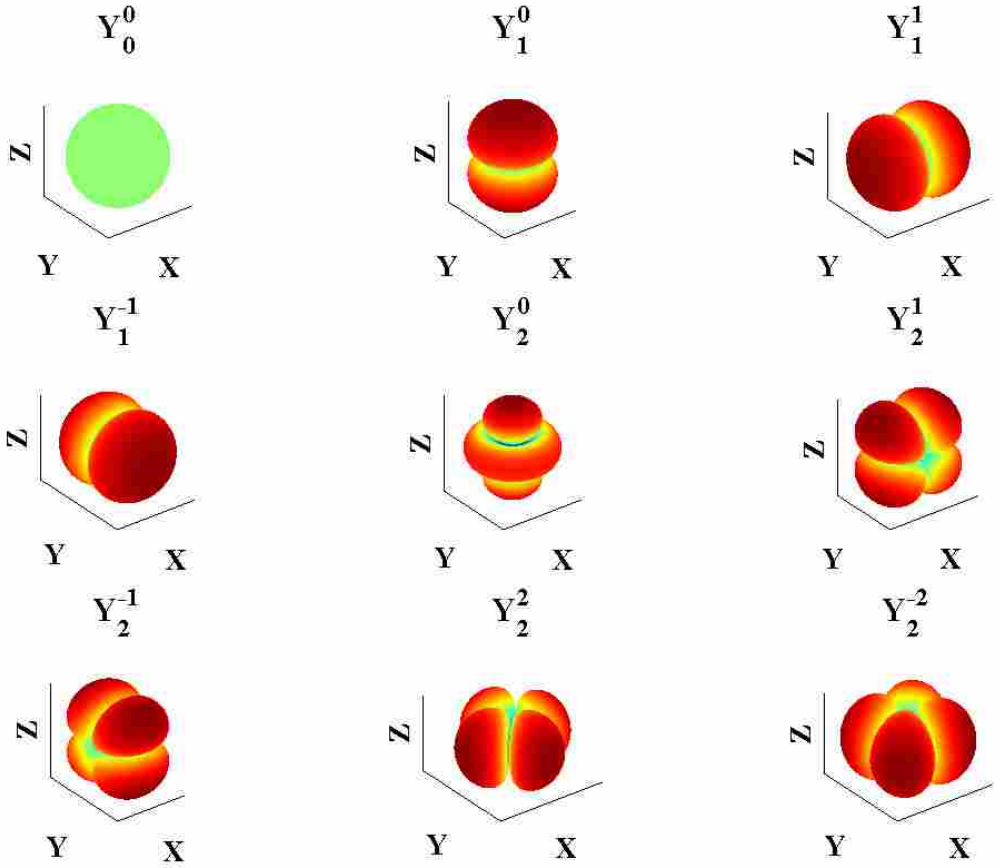

Figure 4-1: Directivity plots of up to the 2nd order spherical harmonics with the *m* and *n* indices shown in the Eq. 4-2 summation. The color scale is the similar between the plots. The *m* = 0, *n* = 0 spherical harmonic is uniform, with no variation in color. Axes units are dB ref. 20 µPa.

m*, *n	**Multipole Type**
0, 0	Monopole
0, 1	Dipole on the *z*-axis
1, 1	Dipole on the *x*-axis
-1, 1	Dipole on the *y*-axis
0, 2	Pseudo-longitudinal Quadrupole on the *z*-axis
1, 2	Lateral Quadrupole in the *xz*-plane
-1, 2	Lateral Quadrupole in the *yz*-plane
2, 2	Axial Lateral Quadrupole on the *xy*-axes
-2, 2	Lateral Quadrupole in the *xy*-plane

Table 4-1: The name and general location of each type of multipolar source in a spherical harmonic series up to the second order, for the *m* and *n* indices shown in the Eq. 4-2 summation. All multipole source distributions are centered at the origin.

the sources is a little smaller than the distance between sources for every other lateral quadrupole in the spherical harmonic series. The mathematical derivation of each multipole in the spherical harmonic series is explored in greater depth in the Appendix.

4.3. MULTIPOLE EXPANSIONS

4.3.1. MULTIPOLE EXPANSION THEORY

An ME extends the theory of spherical harmonics further by calculating the actual source strength of each point source within the multipole source distributions defined for each individual spherical harmonic[47]. The total number of independent source strengths for a second order ME is 19. The expected number of source strengths for a second order ME would be 26, however, there are some point sources that overlap. The overlapping point sources, each of them located on a coordinate axis, may be added using superposition of pressures to yield the source distribution shown in Figure 4-2. Table 4-2 shows the *m* and *n* coefficients and how they correlate to the variables used in Figure 4-2. It is important to note that the distance represented by the dark line connecting each point source and its closest neighbors in Figure 4-2 is defined as ε. Naturally, the distance, ε, must be small in comparison to an acoustic wavelength in order for the multipoles to acoustically couple. This distance is arbitrarily defined. However, it cannot exceed the radius of the smallest sphere containing the noise source.

The method for the calculation of individual source strengths can be illustrated using a point monopole source as an example. Before attempting to solve for the source strength due to the monopole contribution of the noise, it is necessary to use the method proposed in Section 4.2 of this chapter to determine the spherical

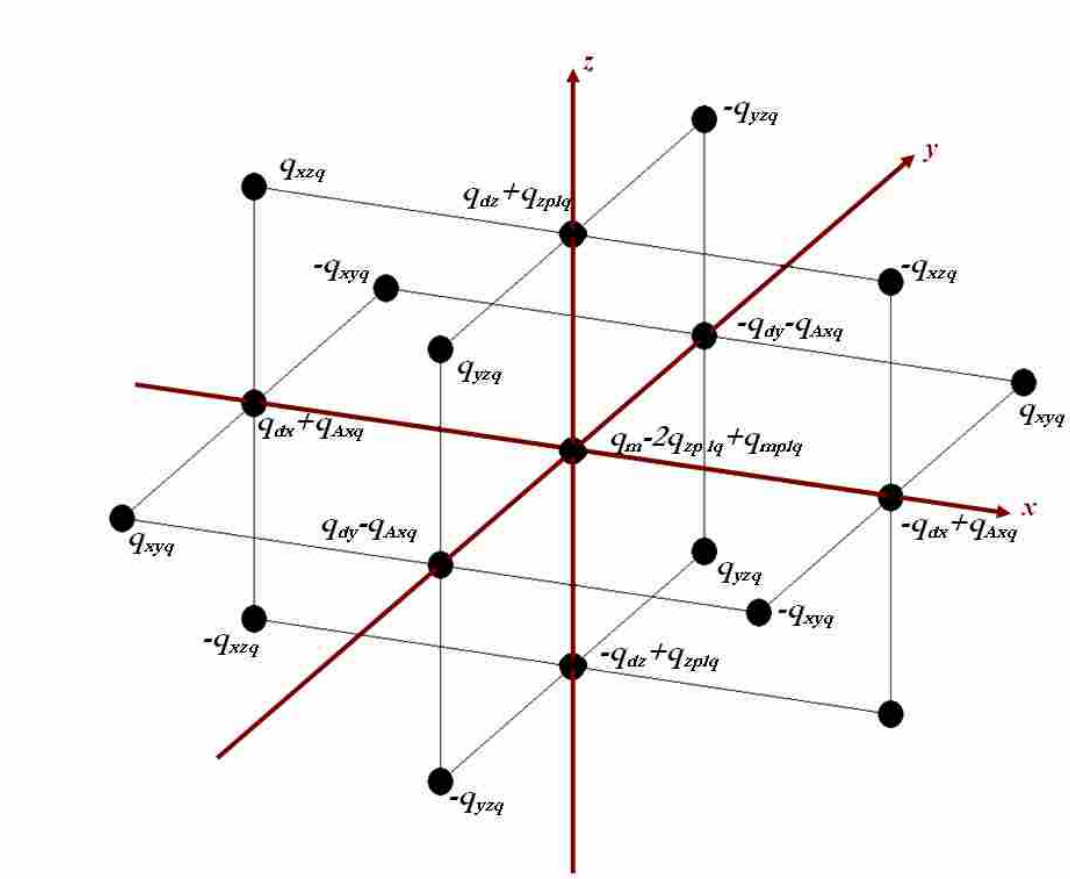

Figure 4-2: The locations and source strengths of each of the 19 point sources in a 2nd order ME. Each linear segment between point sources is equal to the distance ε.

$\hat{A}_{mn}$	**Source Strength (Figure 4-2)**
$\hat{A}_{00}$	q_m
$\hat{A}_{01}$	q_{dz}
$\hat{A}_{11}$	q_{dx}
$\hat{B}_{11}$	q_{dy}
$\hat{A}_{02}$	q_{zplq}, q_{mplq}
$\hat{A}_{12}$	q_{xzq}
$\hat{B}_{12}$	q_{yzq}
$\hat{A}_{22}$	q_{Axq}
$\hat{B}_{22}$	q_{xyq}

Table 4-2: The name of each variable in Figure 4-2 as it relates to a spherical harmonic. The variables are arranged in the same order as in Table 4-1.

harmonic coefficient, $\hat{A}_{00}$. The analytical expression for a point monopole source is

$$\hat{p}_m(r,\theta,\varphi) = \frac{\rho_0 c k^2}{4\pi}\hat{q}_m\left(-i\frac{e^{ikr}}{kr}\right)e^{-i\omega t}, \tag{4-8}$$

assuming an $e^{-i\omega t}$ time dependence. The equivalent expression for the pressure of a point monopole source is

$$\hat{p}_m(r,\theta,\varphi) = \hat{A}_{00}\mathrm{Y}_0^0(\cos\theta)h_0^{(1)}(kr), \tag{4-9}$$

$$\mathrm{Y}_0^0(\cos\theta) = 1, \tag{4-10}$$

$$h_0^{(1)}(kr) = -i\frac{e^{ikr}}{kr}. \tag{4-11}$$

The two expressions for pressure, equations (4-8) and (4-9), may be set equal to one another and the like terms are canceled from the equation. The variables that are left may be used to solve for the monopole source strength,

$$\hat{q}_m = \frac{4\pi}{\rho_0 c k^2}\hat{A}_{00}, \tag{4-8}$$

This method may be applied to the other eight multipoles. A detailed derivation of the other eight source strengths is found in the Appendix. The source strengths can be used in equation (2-1), for a point monopole source with a zero initial phase, and superimposed to reconstruct the radiated pressure at any point outside the smallest sphere containing the noise source.

4.3.2. CHARACTERIZATION OF NOISE SOURCES

The procedure for the ME of an arbitrary noise source requires knowledge of spherical harmonics and their relationship to multipole point source distributions. In

fact, a spherical harmonic expansion is identical to an ME up to a certain point in the procedure. The main difference between the two methods is that the spherical harmonic expansion is used to reconstruct the radiated pressure based solely on the spherical harmonics of the source in question and the ME uses a distribution of point sources to make the same reconstruction[47]. An ME may further be used to find the relative contribution that each separate multipole makes to the total radiated pressure of the noise source.

One difficulty in using an ME to model fan noise is that, according to the orthogonality condition of spherical harmonics, the initial complex pressure measurements must be made over an entire sphere outside of the volume containing the noise source. The only available measurement array was capable of measuring just a hemisphere of data surrounding a noise source. The limitations of measuring a hemisphere of data versus a full sphere of data were explored by inputting a known complex pressure field for a sphere and into the ME and calculating both the dB error between the original pressure field and its reconstruction at the same distance. The hemisphere of pressure data was designed with the same number and location of measurement points as the angular measurement apparatus described in Section 5.2.3. The ME was tested for every kind of multipole up to the second order. The dB error was below one-hundredth of a dB in both the sphere and hemisphere pressure fields for all cases, although the error was slightly less for the full sphere. A hemisphere of measurements is, therefore, sufficient for use in the ME of any arbitrary noise source.

The application of an ME in mapping the near-field pressure of minimized sound power gave rise to a question about the method's validity. If an arbitrary

distance, ε, may be defined for the ME, what effect will this distance have as its value differs from its minimum value to its maximum value? This question may be answered by a simple test. A map of the near-field pressure resulting from acoustic coupling between a multipole primary source and a number of secondary sources may be plotted for several MEs of the exact same primary multipole but with different separation distances, ε. This test was completed using a multipole primary source that consisted of three dipoles in different orientations and a monopole at the origin. Few changes, if any, were found in the near-field pressure as the distance, ε, varied. Figures 4-3 through 4-5 contain three different plots, each with a decreasing value of ε. The blank circle in the center of the plots represents the smallest sphere containing the multipole primary source, outside of which the pressure varies only slightly directly to the left and right of the source distribution.

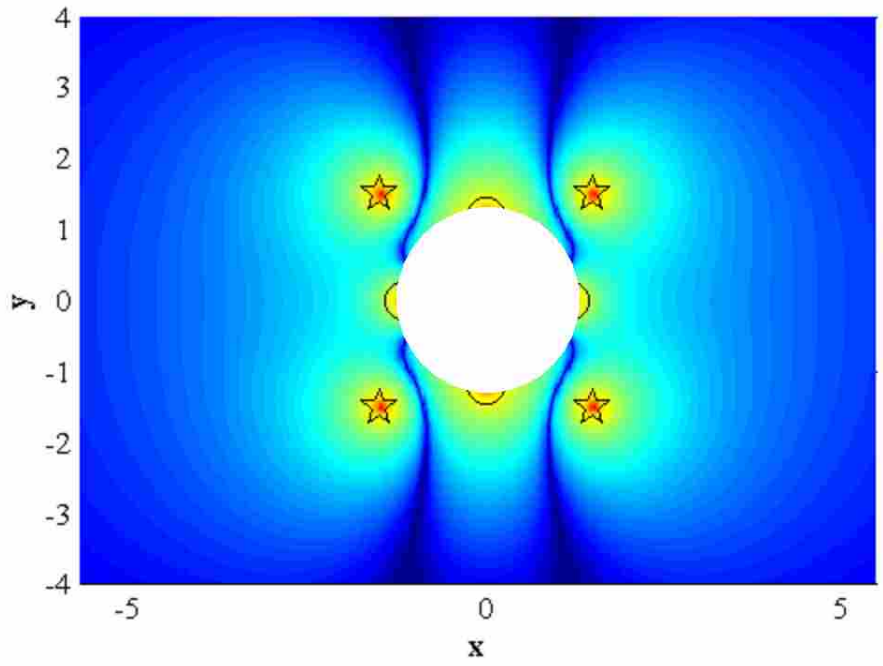

Figure 4-3: A map of the in-plane near-field pressure (ref. 20 µPa) for minimized sound power of the multipole primary source and four control actuators. The distance, ε, is 1 1/8" for this case. Axes units are in inches.

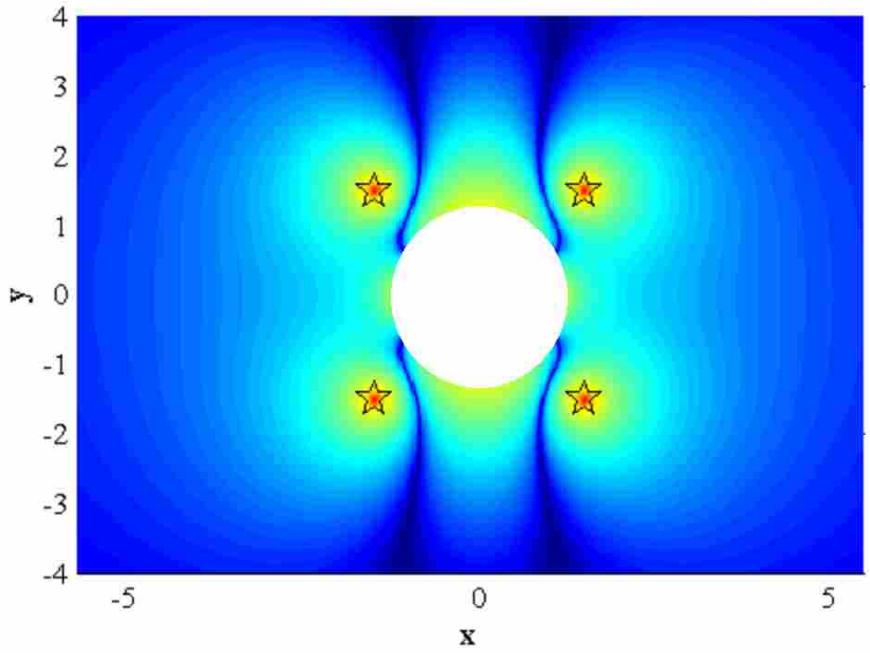

Figure 4-4: A map of the in-plane near-field pressure (ref. 20 μPa) for minimized sound power of the multipole primary source and four control actuators. The distance, ε, is 1" for this case. Axes units are in inches.

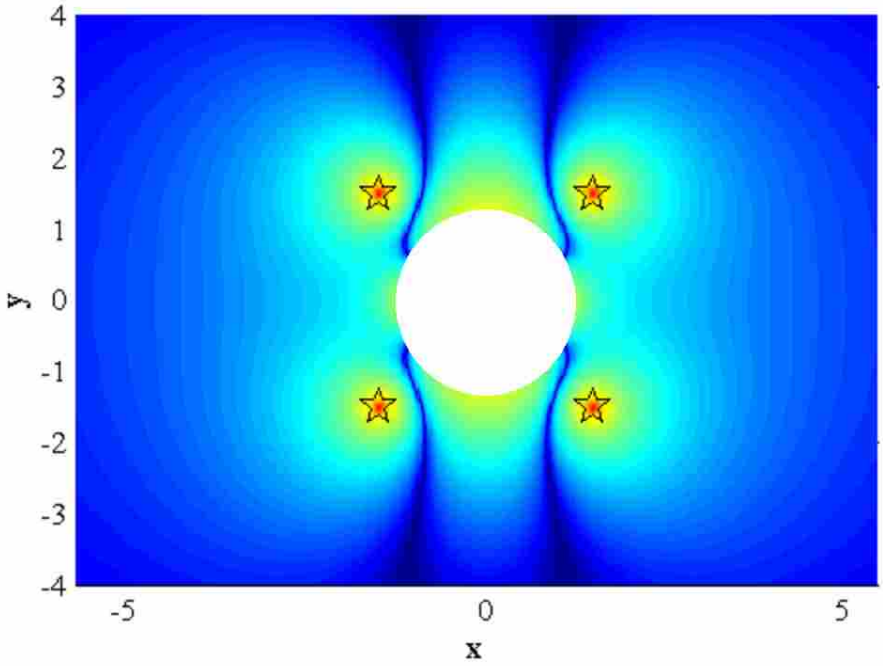

Figure 4-5: A map of the in-plane near-field pressure (ref. 20 μPa) for minimized sound power of the multipole primary source and four control actuators. The distance, ε, is 1/16" for this case. Axes units are in inches.

4.4. MULTIPOLE EXPANSIONS AND NOISE CONTROL

Kempton first suggested the use of an ME for control actuator placement in ANC[24]. His approach involved the placement of control actuators as “anti-sources” in the ME of the primary noise source. He states that the ambiguity in defining the sources of noise that determine the shape of far-field radiation may be an advantage in ANC, but did not experimentally verify this statement.

Martin and Roure used a similar method to the one proposed by Kempton for modeling the acoustic noise from three different types of simulated multipolar acoustic sources[23]. In each case the ME was calculated up to the second order and the control actuator source strengths were calculated based on the minimization of the simulated primary source(s). Error sensors were placed in the acoustic far field of the noise source. The simulated results showed significant global attenuation.

Although each of the aforementioned studies has verified the usefulness of an ME in ANC, this modeling procedure has not yet been used to characterize actual cooling fan noise. A complete characterization of cooling fan noise using multipole point source distributions can be used to map the near-field pressure based on a condition of minimized sound power of any given source distribution and configuration of control actuators. The pressure map may then be used to further optimize the placement of error sensors in ANC.

CHAPTER 5

NEAR-FIELD PRESSURE MAPPING AND GLOBAL ATTENUATION

5.1. THEORETICAL NEAR-FIELD PRESSURE PREDICTION

5.1.1. THE DEVELOPMENT OF A GUI

A MATLAB Graphical User Interface (GUI) was developed for calculating various parameters in a general ANC configuration. The GUI allows the user to enter the x, y, and z coordinates, fundamental frequency, size, magnitude, and phase for any number of primary and secondary, or control, sources in an ANC system. Figure 5-1 shows the part of the user interface that was designed for these parameters. Also,

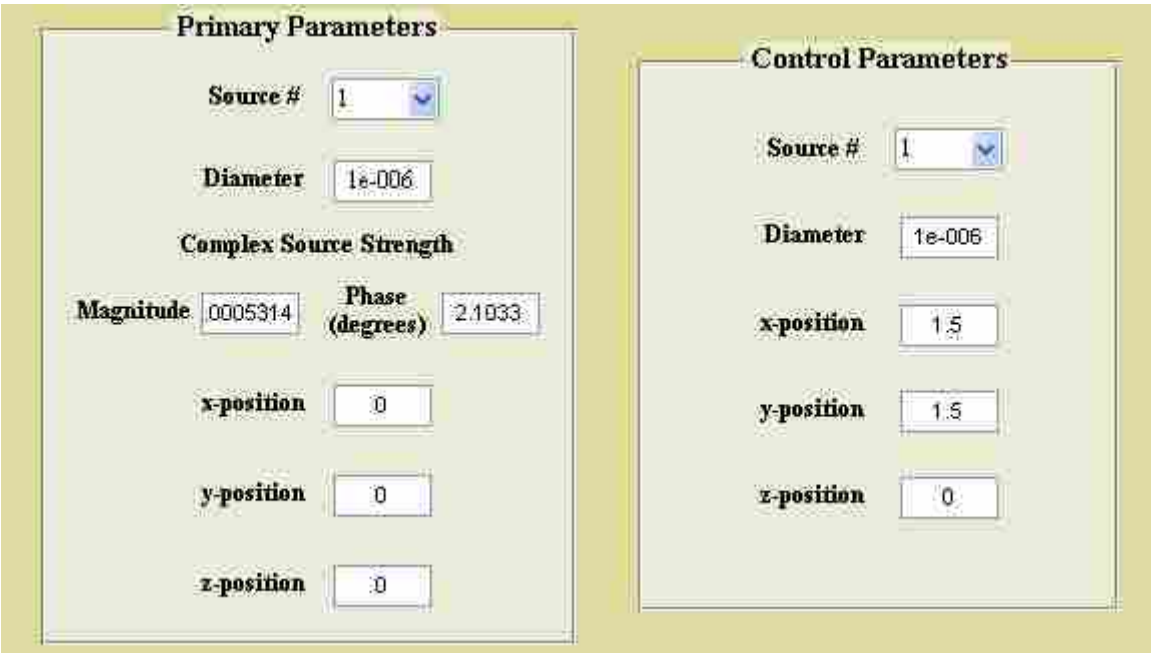

Figure 5-1: Part of the GUI designed to input the source attributes and locations for an ANC system.

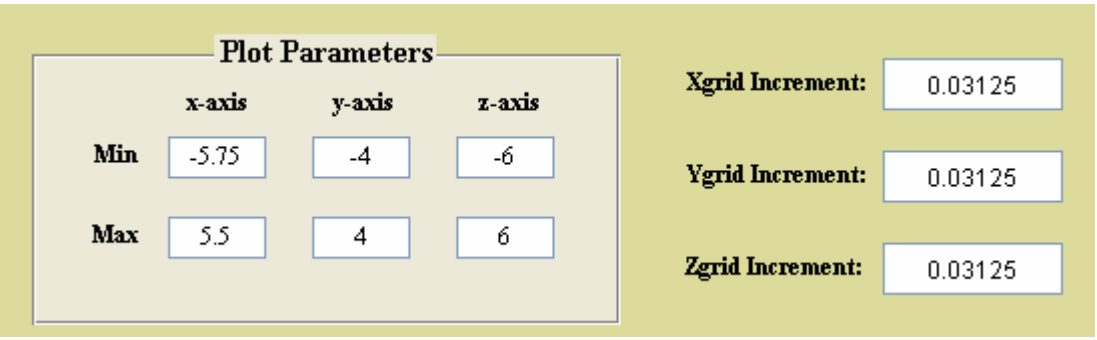

Figure 5-2: Part of the GUI designed to input the x, y, and z plotting limits as well as the plot resolution.

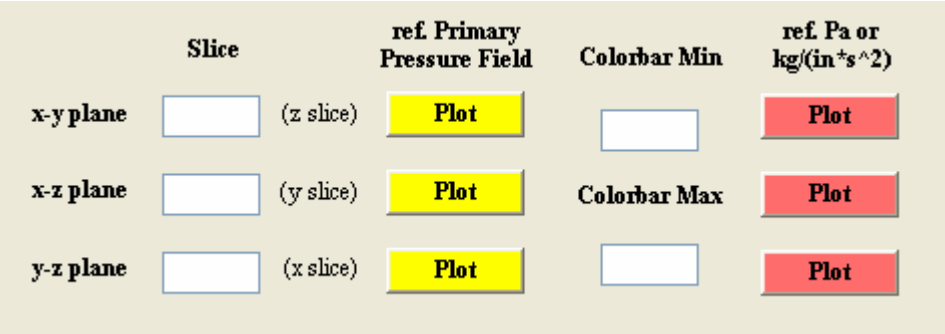

Figure 5-3: Part of the GUI designed to input the specific plot, plotting plane and color attributes.

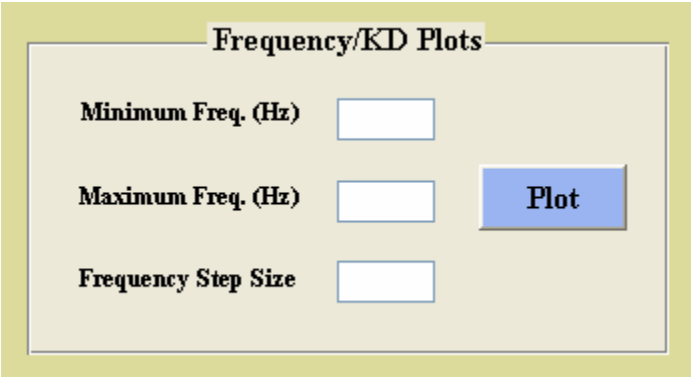

Figure 5-4: Part of the GUI designed to input the plotting range and resolution for the minimum power output (in dB) of the primary/secondary source configuration.

the GUI allows the user to choose all the plotting parameters for either a pressure map, as illustrated in Figures 5-2 and 5-3, or the minimum power output of the system in decibels over any range of frequencies, as shown in Figure 5-4. This type of an interface provides a quicker and more efficient method for mapping the pressure in any plane and at any distance from a single source or any array of sources. This capability becomes a necessity when the primary source is modeled not as a single point monopole acoustic source, but as a distribution of point sources, and when multiple secondary sources are used in varying configurations.

The GUI was primarily designed to use as a tool for error sensor placement. Using the procedure described in the next section, a pressure map may be created that reveals the locations of the near-field pressure nulls that exist in the acoustic coupling of primary and secondary sources. The GUI is also used to test different control source configurations for achievable global attenuation.

5.1.2. PRESSURE MAPPING METHODS

To determine the radiated pressure of any primary/secondary source configuration, the optimum source strengths of each of the secondary sources must be calculated. The optimum source strength for each secondary source is calculated based on a condition of minimized sound power of the source configuration. The method used for these calculations is based on previous work by Nelson and Elliott[16,48]. A vector of complex pressures from an acoustic source distribution can be expressed as the product of a matrix of complex transfer impedances, $\hat{\mathbf{Z}}$, and a vector of source strengths, $\hat{\mathbf{q}}$:

$$\hat{\mathbf{p}} = \hat{\mathbf{Z}}\hat{\mathbf{q}}. \tag{5-1}$$

The matrix of transfer impedances is comprised of the self impedance of each source in the distribution as well as the mutual interaction between sources. As an example, the impedance transfer matrix for a distribution of primary and secondary sources is illustrated in the following equation:

$$\hat{\mathbf{Z}}(p_m \mid s_n) = \begin{bmatrix} \hat{\mathbf{Z}}(p_1 \mid s_1) & \hat{\mathbf{Z}}(p_1 \mid s_2) & \cdots & \hat{\mathbf{Z}}(p_1 \mid s_n) \\ \hat{\mathbf{Z}}(p_2 \mid s_1) & \hat{\mathbf{Z}}(p_2 \mid s_2) & \cdots & \hat{\mathbf{Z}}(p_2 \mid s_n) \\ \vdots & \vdots & \ddots & \vdots \\ \hat{\mathbf{Z}}(p_m \mid s_1) & \hat{\mathbf{Z}}(p_m \mid s_2) & \cdots & \hat{\mathbf{Z}}(p_m \mid s_n) \end{bmatrix}. \tag{5-2}$$

The subscripts *p* and *s* in Eq. 5-2 represent the contributions from each primary and secondary source and the indices *m* and *n* represent the m^{th} primary source and n^{th} secondary source. Similar matrices may be calculated for the mutual impedances of the primary sources, $\hat{\mathbf{Z}}(p_m \mid p_n)$, as well as the secondary sources, $\hat{\mathbf{Z}}(s_m \mid s_n)$, resulting in an *m*-by-*m* matrix for the primary sources and an *n*-by-*n* matrix for the secondary sources.

The impedance matrix for a general array of acoustic sources may be used to calculate the power output of the source configuration in the following manner,

$$W = \tfrac{1}{2}\Re\{\hat{\mathbf{q}}^H \hat{\mathbf{Z}}^H \hat{\mathbf{q}}\} \tag{5-3}$$

The symbol, $\Re$, denotes the real part. Following a similar procedure to the one outlined in Section 2.1 the total sound power of the entire primary/secondary source distribution may be calculated and then minimized for minimum sound power output.

Three variables may be defined that provide a more simplified minimum sound power equation. The three variables, $\hat{\mathbf{A}}$, $\hat{\mathbf{B}}$, and $\mathbf{C}$ are defined as

$$\hat{\mathbf{A}} = \tfrac{1}{2}\Re\{\hat{\mathbf{Z}}(s_m \mid s_n)\}, \tag{5-4}$$

$$\hat{\mathbf{B}} = \tfrac{1}{2}\Re\{\hat{\mathbf{Z}}(p_m \mid s_n)\}\hat{\mathbf{q}}_p, \tag{5-5}$$

$$\mathbf{C} = \tfrac{1}{2}\hat{\mathbf{q}}_p^H\Re\{\hat{\mathbf{Z}}(p_m \mid p_n)\}\hat{\mathbf{q}}_p. \tag{5-6}$$

Using Eq. 5-4 through Eq. 5-6, the expression for minimized sound power of any arbitrary number of primary and secondary sources is

$$W_{\min} = \mathbf{C} - \hat{\mathbf{B}}^H\hat{\mathbf{A}}^{-1}\hat{\mathbf{B}} \tag{5-7}$$

Similar to the example presented in Section 2.1, this expression for minimized sound power may be optimized further by placing the secondary source(s) as close as possible to the primary source(s). The optimum source strength for each secondary source is calculated as

$$\hat{\mathbf{q}}_{so} = -\hat{\mathbf{A}}^{-1}\hat{\mathbf{B}} \tag{5-8}$$

This procedure is the method that was programmed in the GUI to find the optimum source strength, as given in Eq. 5-8, of each secondary source as well as the minimum power output, as given in Eq. 5-7. When the optimum source strength is calculated, the pressure field in any plane relative to the sources may be mapped using a superposition of pressure radiating from each source. Each source is assumed to radiate as a point monopole. The entire procedure is used to find the locations of

pressure nulls in the near field of the control system configuration in order to more accurately place the error sensors.

5.2. EXPERIMENTAL CONFIGURATION

5.2.1. MEASUREMENT SOURCES

An experiment was designed to make measurements of the noise radiated from a 60-mm axial cooling fan, similar to the one shown in Figure 1-2, as well as the 50-mm loudspeaker shown in Figure 5-5. Each source was mounted in the center of an aluminum plate. The measurement *x*- and *y*-axes are shown in Figure 5-7. Both of these sources acted as the primary source for each measurement. Four 25-mm loudspeakers, shown in Figure 5-6, were also mounted in the plate in a symmetric configuration surrounding the primary source. A photograph of the plate is shown in Figure 5-7. These sources acted as the secondary sources, or control actuators. Error sensors were placed in varying locations on the surface of the aluminum plate. The plate was set on a box with dimensions similar to that of a computer, as observed in Figure 5-8.

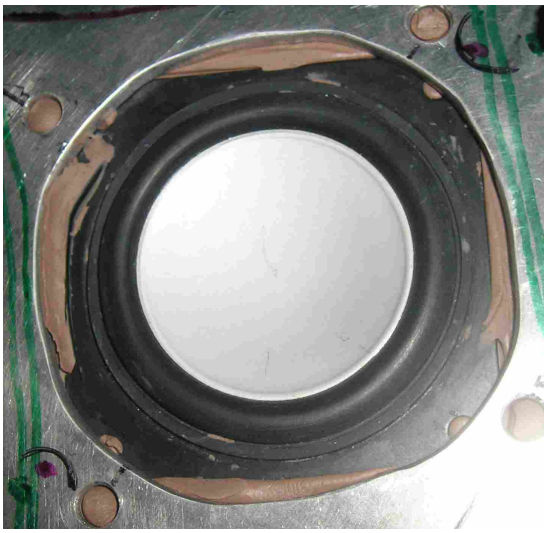

Figure 5-5: A photograph of the 50-mm loudspeaker used as a primary source in the same location on the plate as the axial fan.

Figure 5-6: A photograph of the 25-mm loudspeaker that was used as a control actuator in the ANC system.

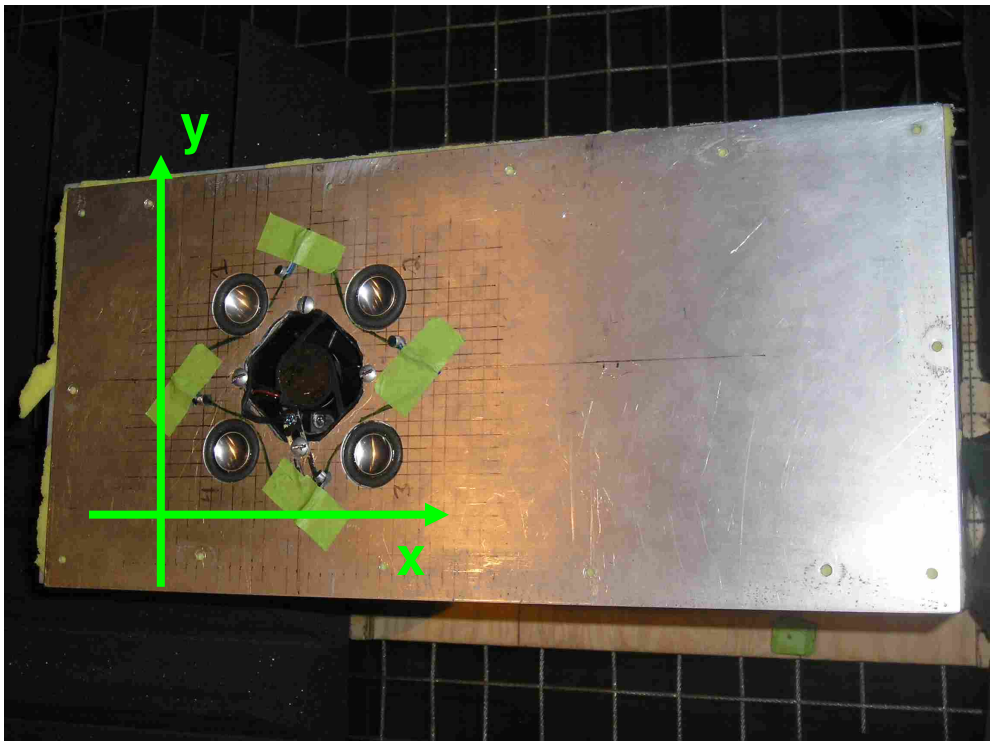

Figure 5-7: A photograph of the aluminum plate used to install the primary and secondary sources. Green arrows mark the directions of the *x*- and *y*-axes for all near-field measurements.

5.2.2. NEAR-FIELD MEASUREMENT APPARATUS

To explore the effect of error sensor placement on global sound power attenuation, two kinds of measurements were made: near-field and far-field. The near-field measurement array consisted of 23 ¼" ICP microphones, each positioned in a linear array and each equally spaced ½" apart. A photograph of the linear array is shown in Figure 5-9. The linear array was mounted in a bracket along the *x*-axis of the plate and allowed one dimensional movement along the *y*-axis. During each set of measurements the linear array was initially placed at the edge of the plate. The array was shifted forward ¼" after each measurement. When the array arrived at the opposite edge of the plate the first set of measurements was finished, resulting in 33 measurements along the *y*-axis of the plate. The array was then shifted ¼" toward the

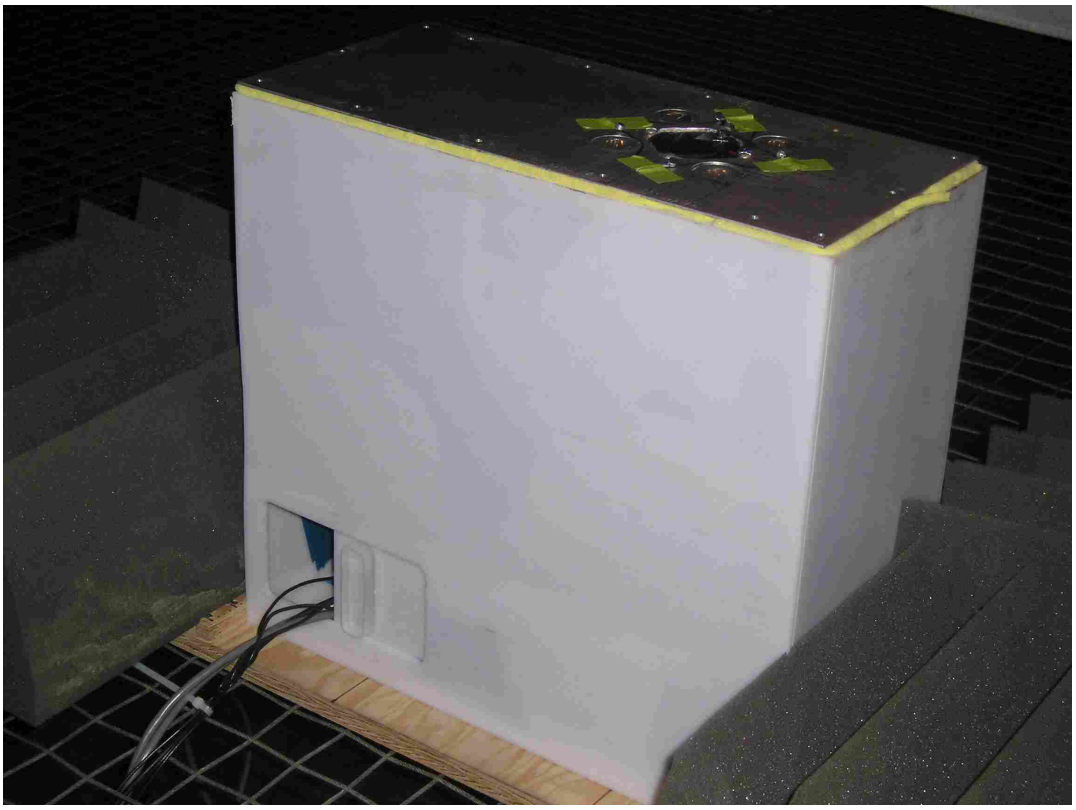

Figure 5-8: A photograph of the complete installation for primary and secondary sources.

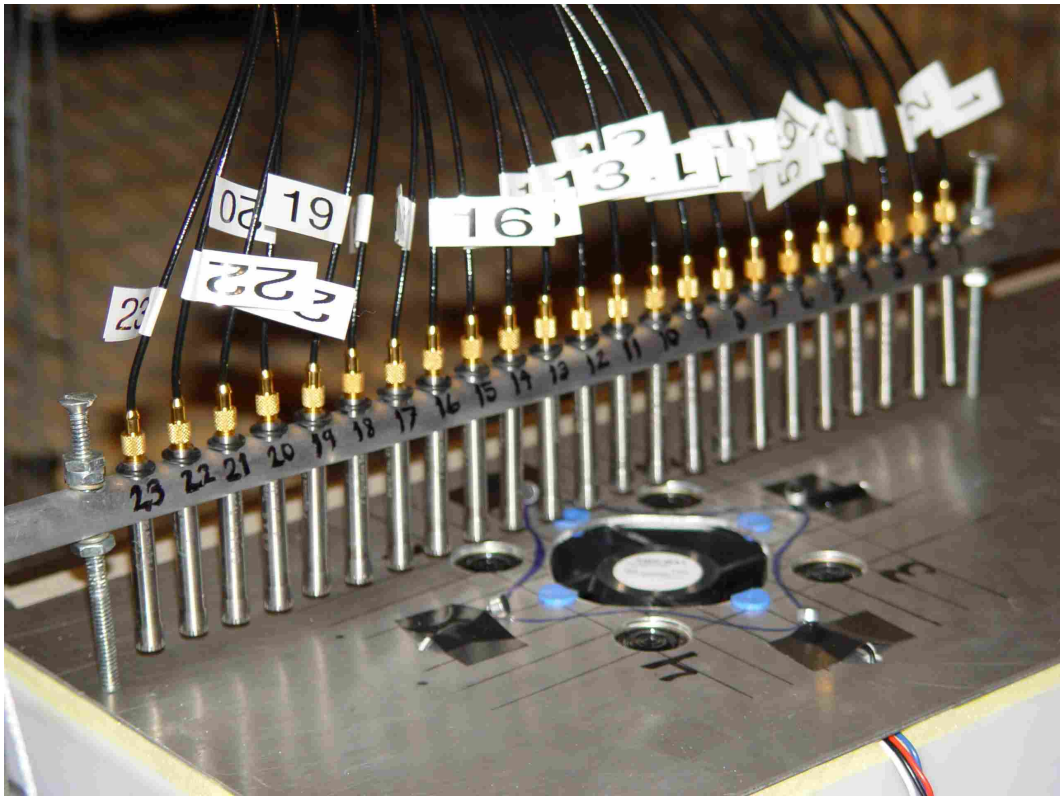

Figure 5-9: A photograph of the linear array. The two screws at each end were used to keep the microphones at an equal distance from the plate

x-direction and another set of measurements was completed. The two sets of data were interleaved in MATLAB to plot a ¼" resolution map of the near-field acoustic pressure. All near-field measurements were made in the *x*-*y* plane ¼" above the aluminum plate.

5.2.3. FAR-FIELD MEASUREMENT APPARATUS

The far-field array was constructed with thirteen ½" ICP microphones in a semi-circular configuration, as shown in Figure 5-10. Each microphone on the angular array was positioned to measure the pressure in equal area segments. The angle of each microphone on the array from the center of the arc is shown in Table 5-1. Microphones one through seven measured 10° increments in φ, from 180° to 350°. Microphones seven through 13 measured 10° increments from 0° to 170° in φ. A

Figure 5-10: A photograph of the semi-circular measurement array.

Mic #	Angle (θ)
1	-85.6°
2	-75.9°
3	-65.8°
4	-54.8°
5	-42.0°
6	-24.5°
7	-0.0°
8	24.5°
9	42.0°
10	54.8°
11	65.8°
12	75.9°
13	85.6°

Table 5-1: The angles, in degrees θ, for each microphone on the measurement arc. The arc spans from $-\pi/2$ to $\pi/2$ in θ.

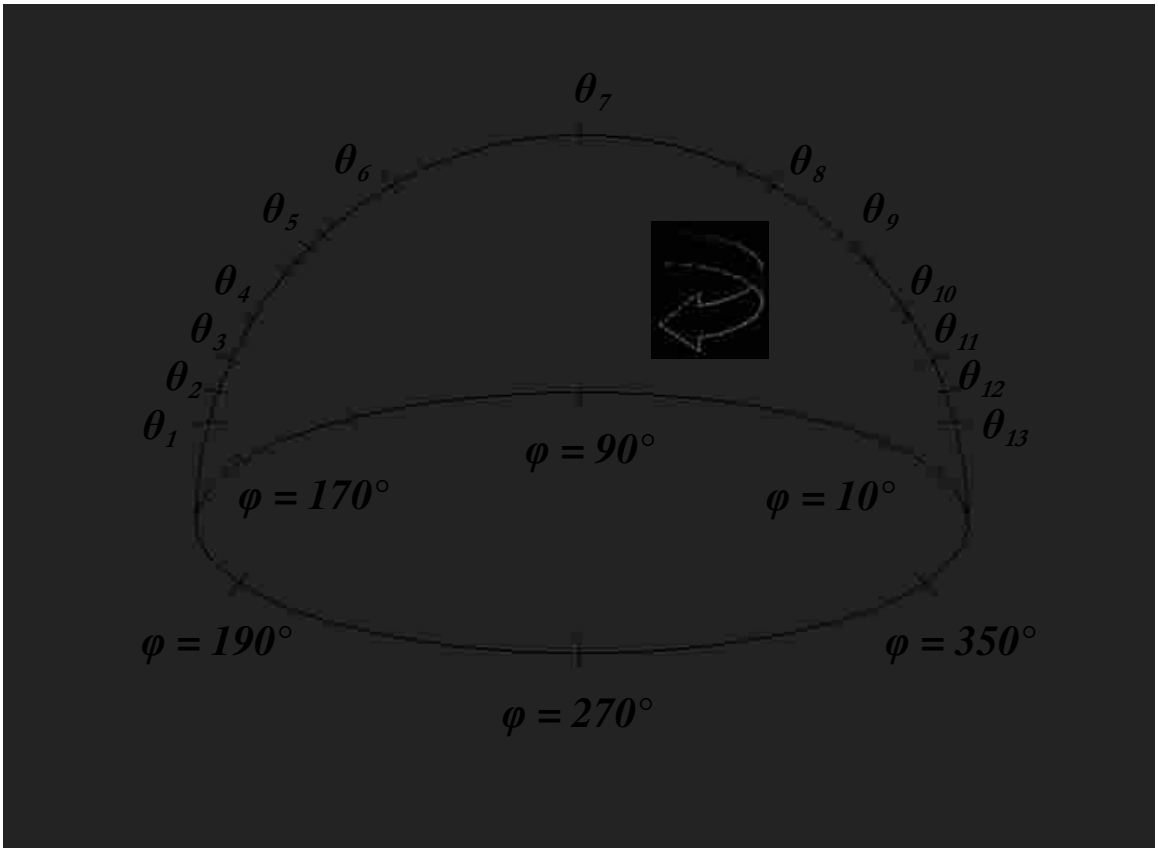

Figure 5-11: A diagram of the microphone locations on the angular array (θ) and some of the measurement locations (φ). The direction of motion for each measurement is indicated with an arrow.

complete illustration of the measurement scheme for this array may be found in Figure 5-11. The plate was positioned so that the center of the primary source aligned with the center of microphone seven on the angular array. The array was initially positioned on the *x*-axis and was rotated 10° (in φ) after each measurement and finished when the angular array reached 170°, making a total of 18 measurements. All measurements, both near- and far-field, were made inside a qualified anechoic chamber.

5.2.4. HARDWARE

The microphone signals were all patched through the chamber into a control room. A National Instruments PXI machine was used to receive the input channels

and perform the necessary signal processing, such as sampling and averaging. A LABVIEW interface was used for motion control and initial plotting of the far-field angular array. A similar interface was used to make the near-field measurements. The data from each channel and measurement was saved in a file compatible for loading in MATLAB. Each measurement was processed in LABVIEW and the results were plotted using a code developed in MATLAB.

The ANC measurements required several pieces of hardware. An infrared emitter/detector was used as the reference signal for the cooling fan. The emitter was placed on the outlet side of the fan and the detector was placed on the fan inlet. The complete emitter/detector pair was then used to detect the passing of each individual blade through the infrared light. After being digitally filtered, the reference signal was passed through an analog input/output device and filtered for anti-aliasing. The input/output device communicated electronically to a DSP that performed all of the algorithms and system identification procedures used in ANC. Electret microphones, 5-mm in diameter, were used as error sensors for the ANC system, as shown in Figure 5-12. A photograph of the input/output device and DSP is provided in Figure

Figure 5-12: A photograph of one 5-mm electret microphone used as an error sensor.

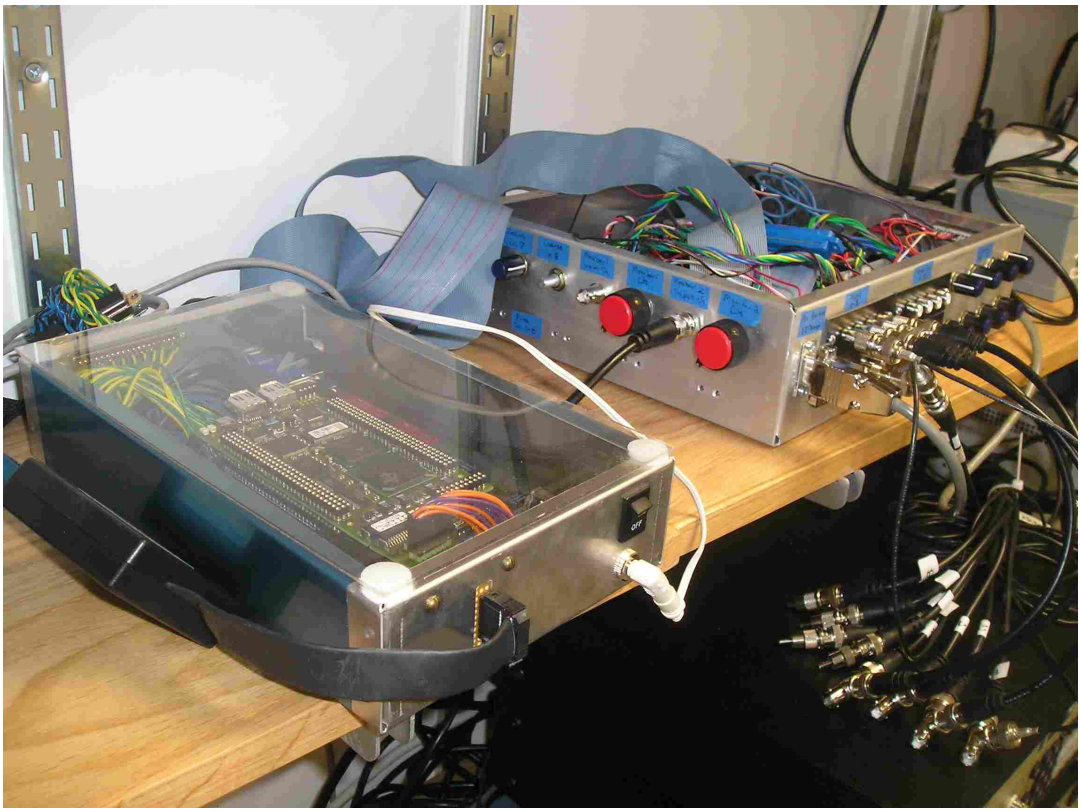

Figure 5-13: A photograph of the DSP (left) and analog input/output device (right).

5-13. The error sensor pre-amplification and control actuator outputs were all calibrated before running the system identification procedure. Calibration, system identification, and ANC were all controlled with a laptop computer.

5.3. NEAR-FIELD ERROR SENSOR PLACEMENT RESULTS

To verify that the near-field pressure nulls exist for minimized sound power of a single point monopole source, the 50-mm loudspeaker was used as the primary noise source. The excitation signal of the loudspeaker was a sine wave at 622 Hz. This frequency was chosen to mimic the BPF of the 60-mm axial cooling fan. The radiated sound field was measured with and without ANC. The near-field ANC measurements were compared to the theoretical predictions for two benchmark cases: two control

a) b)

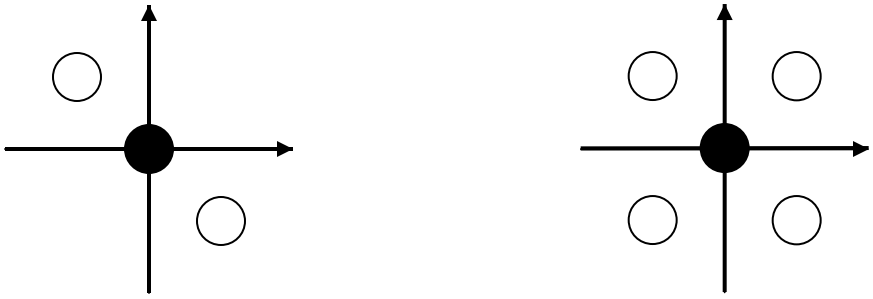

Figure 5-14: The ANC configuration for a) one primary source (black circle) and two control actuators (white circles) and b) one primary source (black circle) and four control sources (white circles).

actuators located 2.12" from the center of the primary source to the center of each control actuator, as shown in Figure 5-14a, and four control actuators symmetrically located around the primary source and at the same distance, as shown in Figure 5-14b. The naming convention for each benchmark cases is two-by-two, meaning two control actuators with two error sensors, and four-by-four, meaning four control actuators with four error sensors. The average far-field global sound level reduction was also measured with the angular array and plotted on a three-dimensional surface. The axial fan, with a BPF of 622 Hz, was then placed in the same location as the primary loudspeaker source and the near- and far-field pressure was measured for the ANC configuration illustrated in Figure 5-14b. The standard deviation for loudspeaker and fan global attenuation calculations was 0.1 dB and 0.3 dB respectively.

A theoretical map of the near-field pressure in a plane parallel to and 0.25"above a monopole noise source is shown in Figure 5-15. The axis units for this and every subsequent near-field pressure map are in inches. The primary loudspeaker source was measured in the same near field plane using the linear microphone array. The resulting pressure map is shown in Figure 5-16. The loudspeaker appears to radiate the same

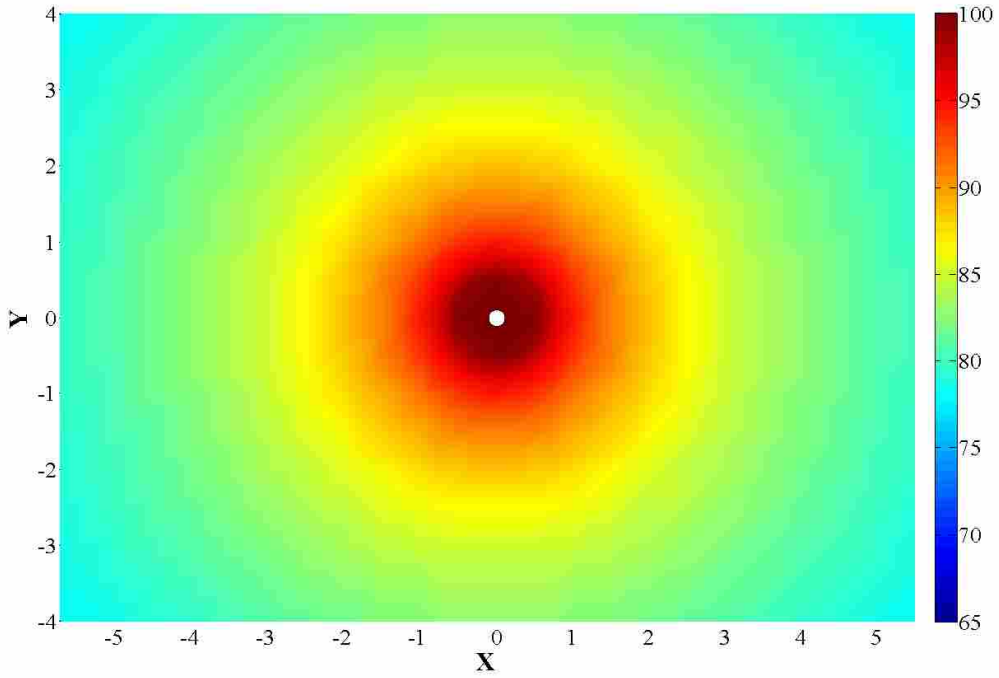

Figure 5-15: A theoretically calculated near-field pressure map (dB ref. 20 µPa) of a single point monopole at 622 Hz in a plane 1/4" above the source. The circle marks the location of the source. Axes units are in inches.

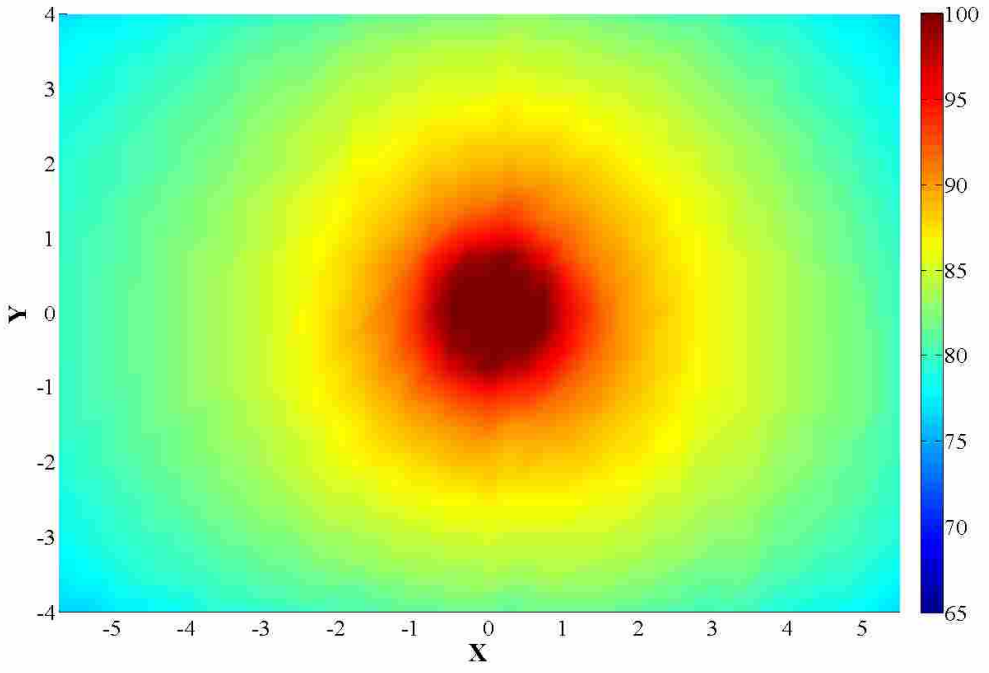

Figure 5-16: A near-field measurement (dB ref. 20 µPa) of the 50-mm loudspeaker source in a plane 1/4" above the source and at 622 Hz. Axes units are in inches.

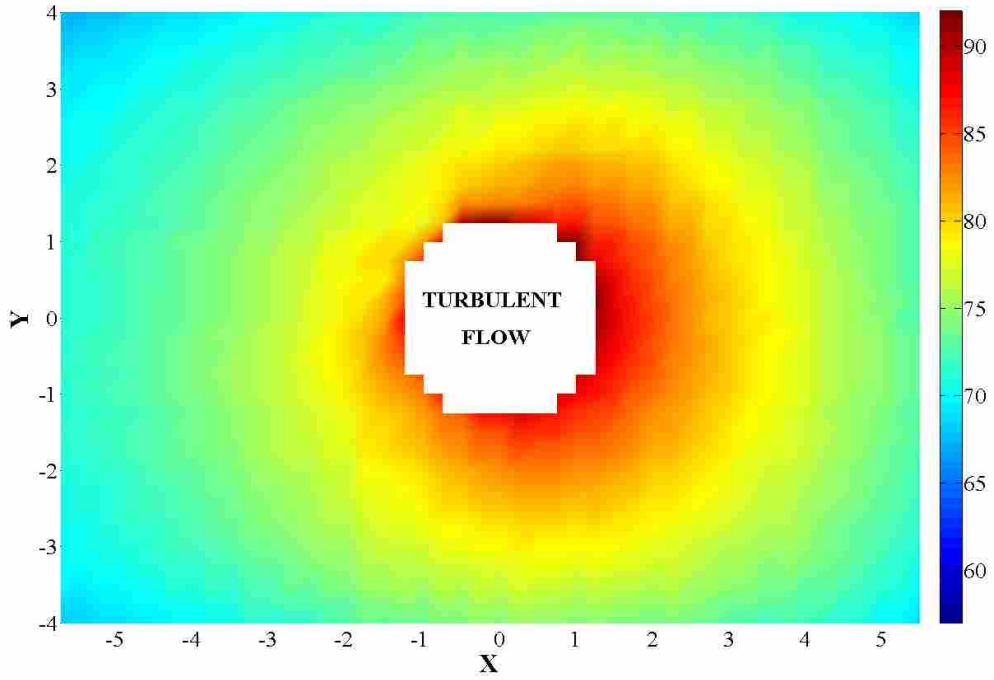

Figure 5-17: A near-field measurement (dB ref. 20 µPa) of the 60-mm axial cooling fan (BPF 622 Hz) in a plane 1/4" above the source. Axes units are in inches.

pressure field as a monopole source. In comparison, the pressure field of an axial cooling fan installed in the same plate, as shown in Figure 5-17, but with the installation of an infrared emitter/detector pair, appears to radiate like a monopole that is skewed in the positive *x*-direction.

5.3.1. TWO-BY-TWO CONTROL

A map was created to plot the pressure field due to minimized sound power of the two-by-two configuration illustrated in Figure 5-14a. This map, as shown in Figure 5-18, was used to place the error sensors during ANC for the same configuration. A similar theoretical plot is shown in Figure 5-19 that plots the radiated pressure referenced to 20 µPa. The pressure field was also measured and mapped, as shown in Figure 5-20. The theoretical pressure field is calculated as

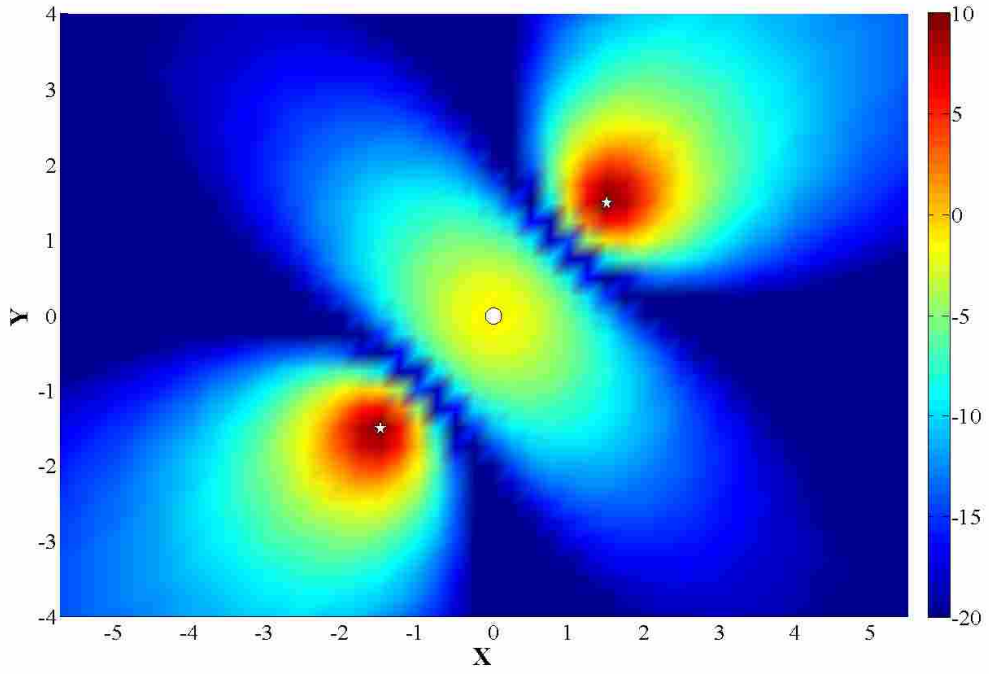

Figure 5-18: A theoretical pressure map of the near-field radiated pressure (dB ref. primary pressure field) in a plane 1/4" above the source due to minimization of sound power for primary (white circle) and secondary (white star) sources at 622 Hz. Axes units are in inches.

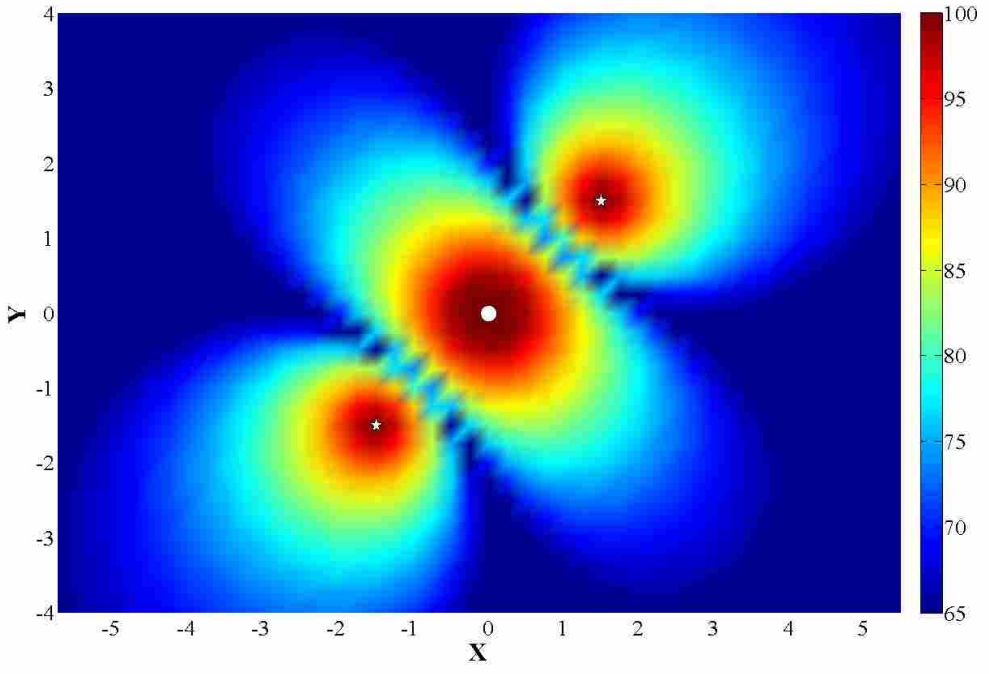

Figure 5-19: A theoretical map of the near-field pressure (dB ref. 20 µPa) 1/4" above the source due to sound power minimization for primary (white circle) and secondary (white star) sources at 622 Hz. Axes units are in inches.

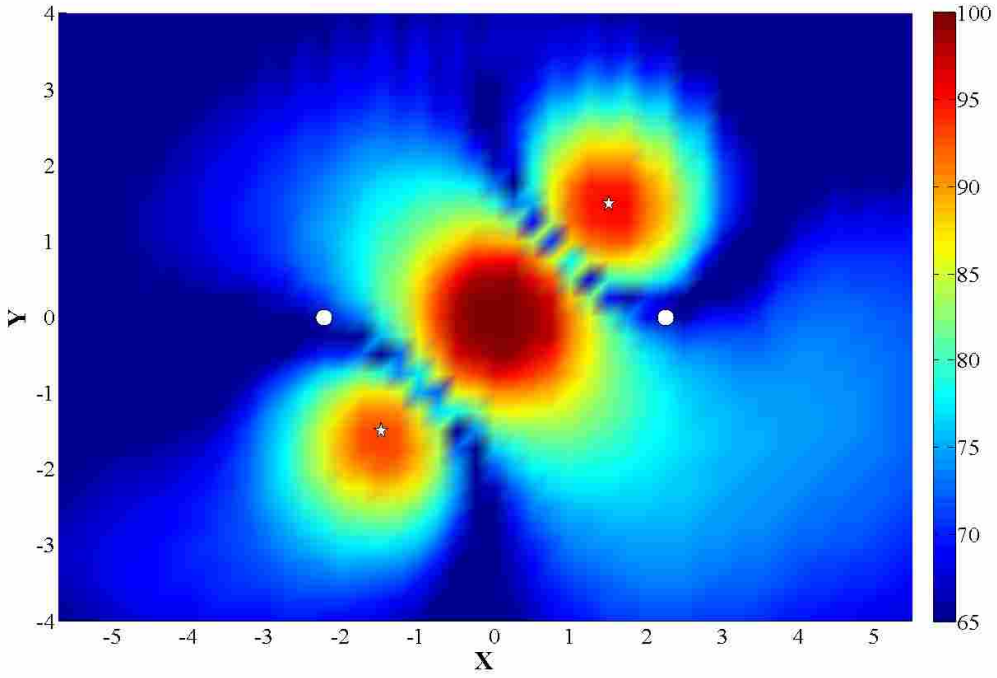

Figure 5-20: A near-field measurement (dB ref. 20 µPa) of the two-by-two ANC system for the 50-mm loudspeaker at 622 Hz and 1/4" above the source. White circles mark the locations of the error sensors. Axes units are in inches.

sound pressure level referenced to the pressure field of the primary source alone. This plot is more useful in locating the pressure nulls that are created for the condition of minimized sound power of the primary and secondary sources. The near-field pressure nulls created in the actual measurement closely resemble those predicted in Figure 5-19.

The global sound pressure level attenuation was measured in the far-field of the primary source and the three-dimensional surface plot is shown in Figure 5-21. For every far-field plot in this thesis the outer wire mesh grid is the measurement of the loudspeaker or fan without ANC and the inner color-surface plot is the measurement when ANC is turned on and allowed to converge to a global minimum.

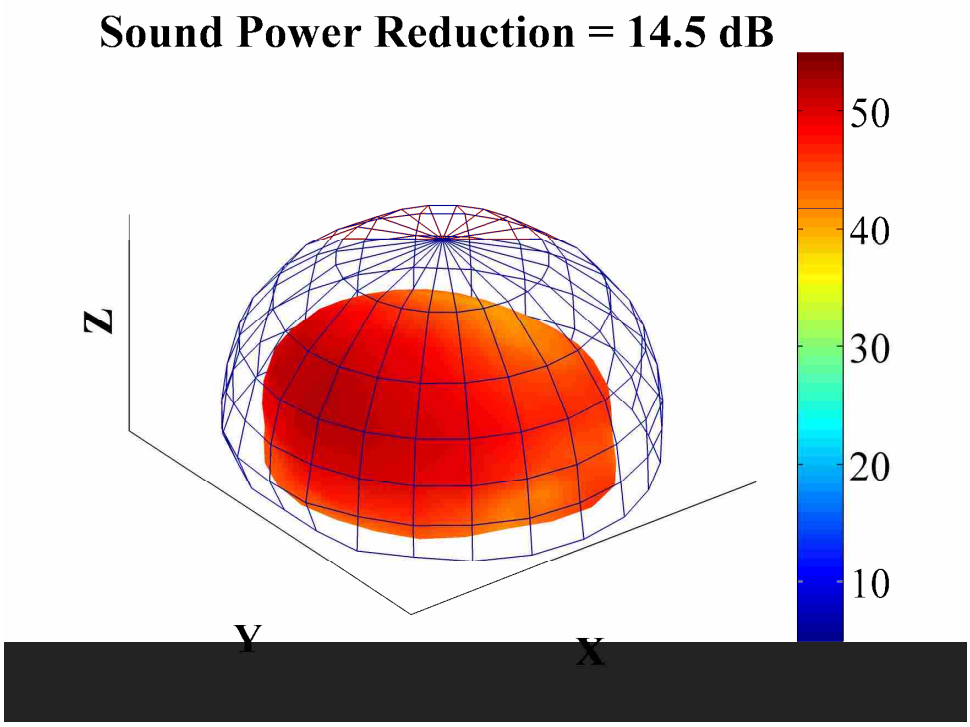

Figure 5-21: A far-field measurement of the two-by-two ANC system with (color) and without (wire mesh) control for the 50-mm loudspeaker source at 622 Hz. Axes units are in dB ref. 20 µPa.

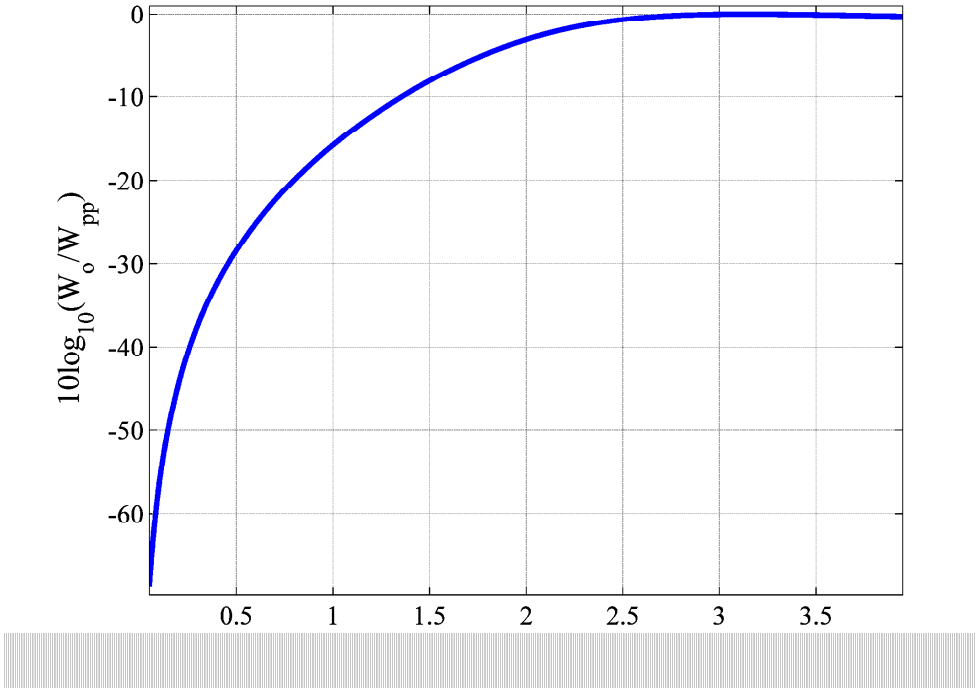

Figure 5-22: A theoretical curve of the achievable sound power reduction in dB (ref. sound power of the primary source) for the two-by-two ANC system over *kd*. For the fan BPF, *kd* ≈ 0.6.

Although this type of global sound power reduction is desirable, it does not reach the potential reduction determined by the point source model. A curve of the global sound power reduction, in dB, for this primary/secondary source configuration is shown in Figure 5-22. The sound power reduction is plotted as a function of *kd*, or the wave number multiplied by the separation distance of the sources to the primary source. According to this plot, the achievable global sound power reduction should be over 25 dB at the *kd* value (≈0.6) that is associated with the BPF of the fan for this ANC system.

5.3.2. FOUR-BY-FOUR CONTROL

The ANC configuration in Figure 5-14b was also mapped and used to verify the locations of near-field pressure nulls. Again, a theoretical pressure map was made for the minimization of sound power from the primary and secondary sources in the

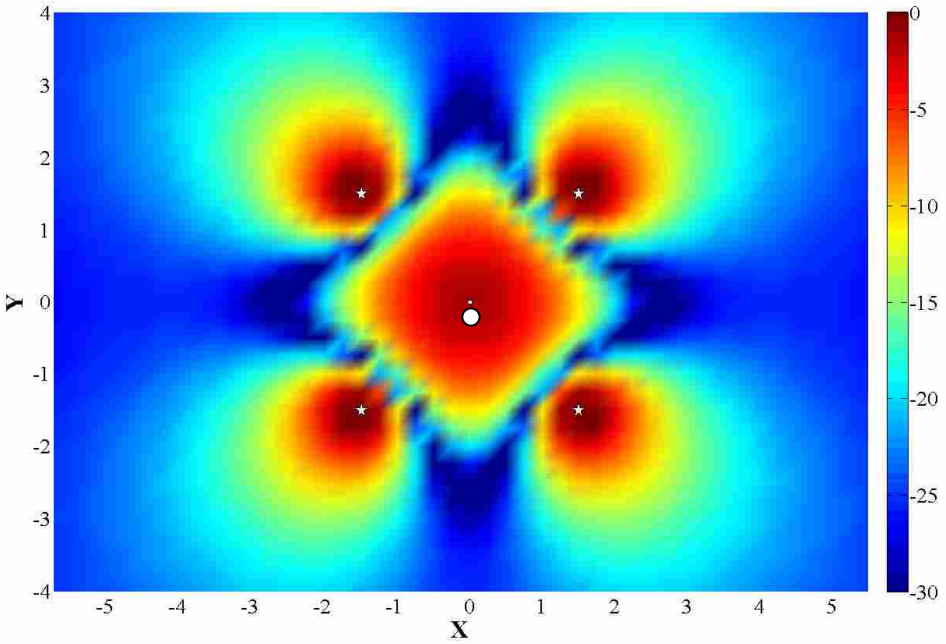

Figure 5-23: A theoretical pressure map of the near-field radiated pressure (dB ref. primary pressure field) 1/4" above the source due to minimization of sound power for the four-by-four ANC configuration at 622 Hz. Axes units are in inches.

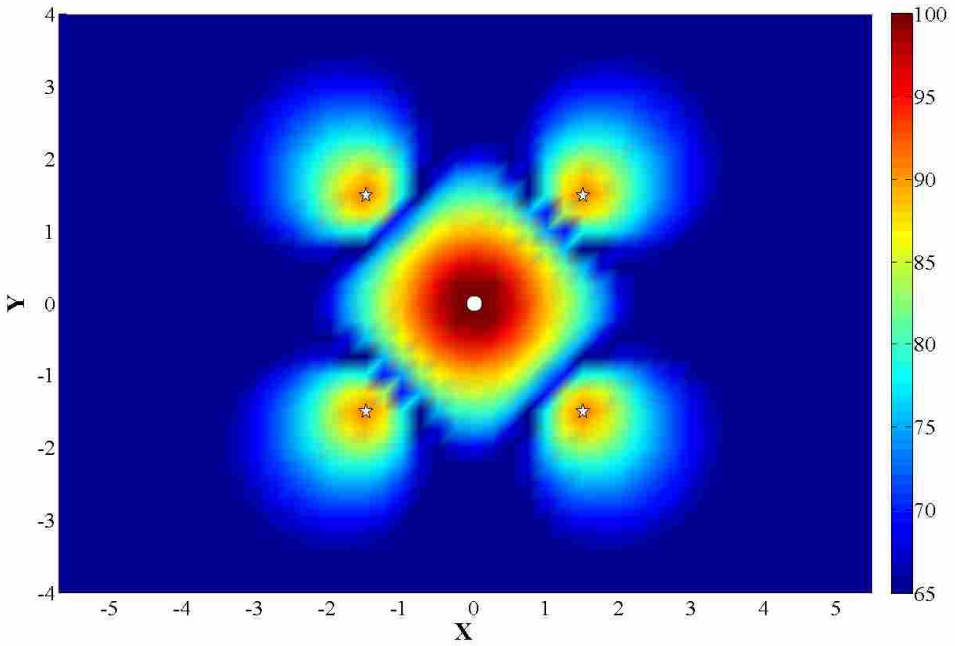

Figure 5-24: A theoretical pressure map of the near-field radiated pressure (dB ref. 20 µPa) 1/4" above the source due to minimization of sound power for the four-by-four ANC configuration at 622 Hz. Axes units are in inches.

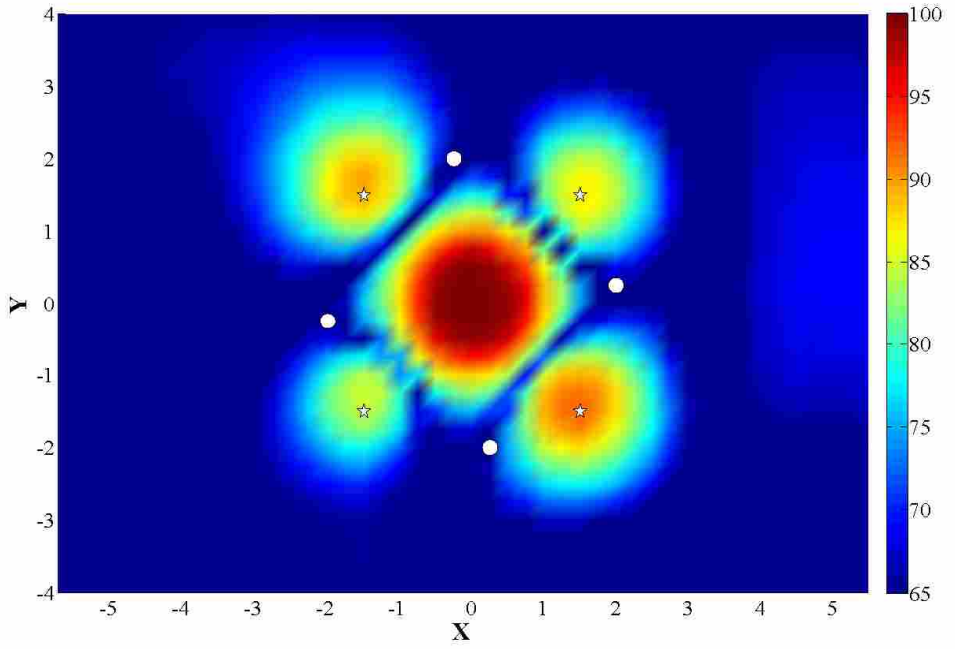

Figure 5-25: A near-field measurement pressure (dB ref. 20 µPa) of the four-by-four ANC system for the 50-mm loudspeaker (622 Hz) 1/4" above the source. White circles mark the locations of the error sensors. Axes units are in inches.

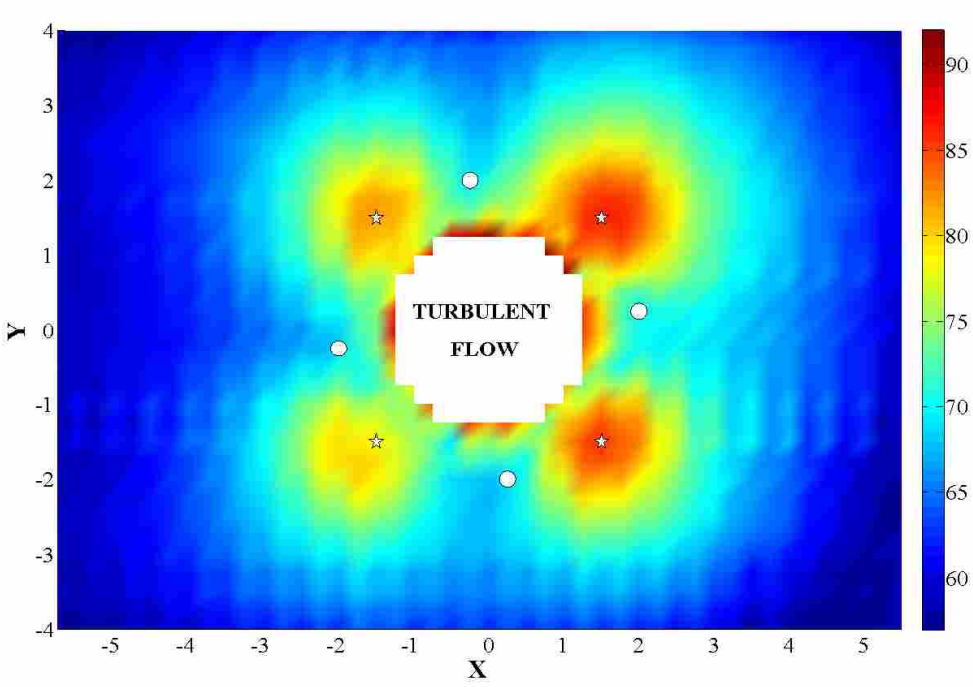

Figure 5-26: A near-field measurement (dB ref. 20 µPa) of the four-by-four ANC system for the axial cooling fan (BPF 622 Hz) 1/4" above the source. White circles mark the locations of the error sensors. Axes units are in inches.

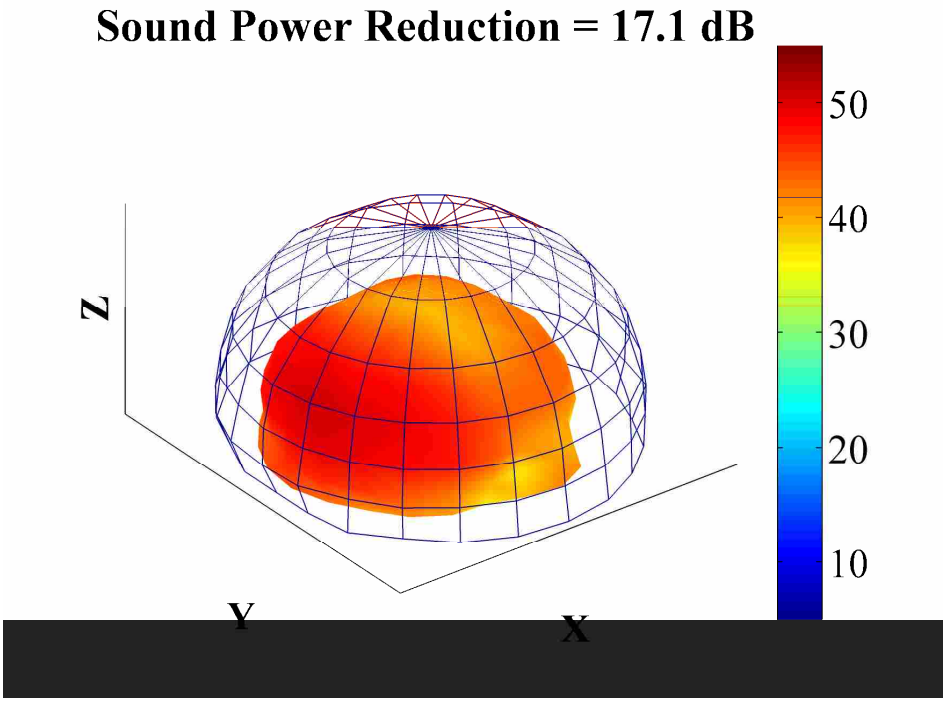

Figure 5-27: A far-field plot of the four-by-four ANC system with (color) and without (wire mesh) control of the 50-mm loudspeaker source at 622 Hz. Axes units are in dB ref. 20 µPa.

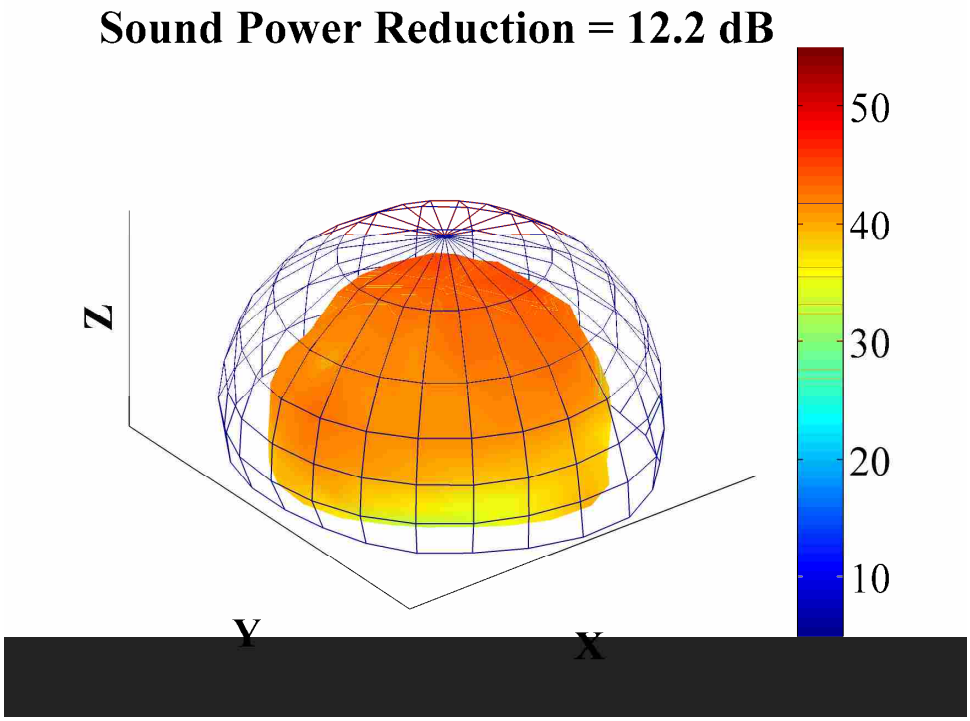

Figure 5-28: A far-field plot of the four-by-four ANC system with (color) and without (wire mesh) control of the axial cooling fan at its BPF (622 Hz). Axes units are in dB ref. 20 µPa.

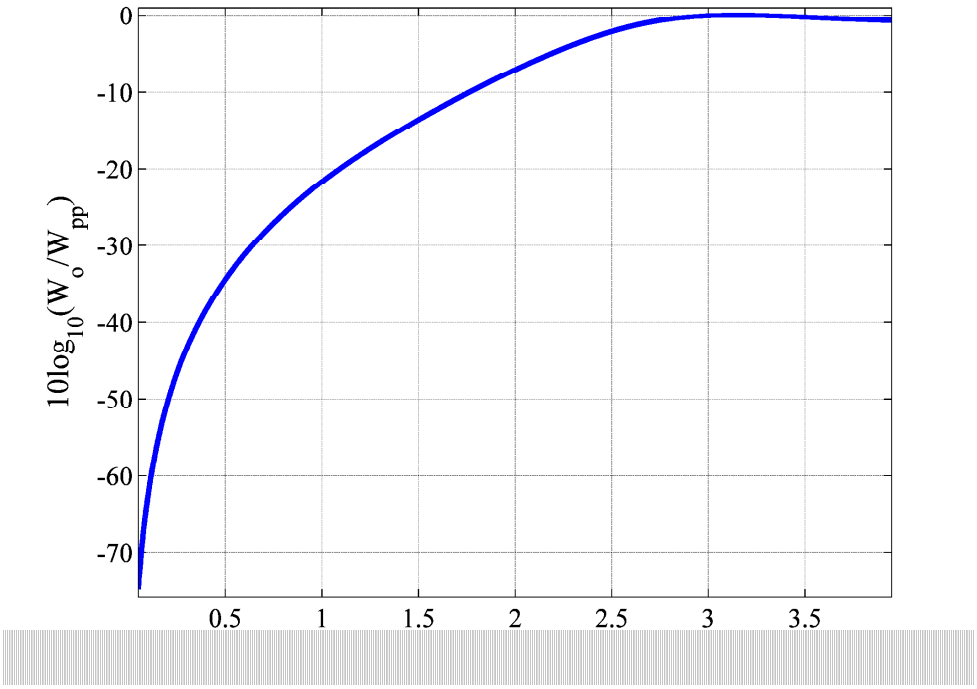

Figure 5-29: A theoretical curve of the achievable sound power reduction in dB (ref. sound power of the primary source) for the four-by-four ANC system over *kd*. For the fan BPF, *kd* ≈ 0.6.

four-by-four configuration, and is shown in Figures 5-23 and 5-24. A plot of the measured pressure map of this ANC system for a loudspeaker primary source is shown in Figure 5-25. The pressure nulls that are created by the minimization of sound power for this ANC system are almost exactly the same as those plotted in Figure 5-24. In comparison, the pressure nulls are not nearly as prominent for the axial cooling fan, as illustrated in Figure 5-26, partially due to the drastic increase in the acoustic energy of the broadband noise floor. The global sound pressure level attenuation for the loudspeaker source vs. the fan source is shown in Figures 5-27 and 5-28.

Once again the potential for global sound power reduction was not reached for the four control actuator configuration. The four-by-four ANC configuration should be able to reduce the global sound power by over 30 dB for $kd \approx 0.6$. The plot in Figure 5-29 is an illustration of this principle.

To explore the capabilities of the ANC system to adapt well to changes in error sensor placement, one of the error sensors was placed far away from its intended location on the plate. The near-field results for this experiment are shown in Figures 5-30 and 5-31 for the loudspeaker and fan. The far-field results are plotted in Figures 5-32 and 5-33. In comparison, the global reduction for the loudspeaker with and without the changed error sensor placement, shown in Figures 5-32 and 5-27, was within the standard deviation of 0.3 dB for that set of measurements, or 0.1 dB. A comparison of the global reduction of the fan, as shown in Figures 5-33 and 5-28, yielded similar results within a measurement standard deviation of 0.3 dB. It may be observed further that although there was virtually no change in far-field global

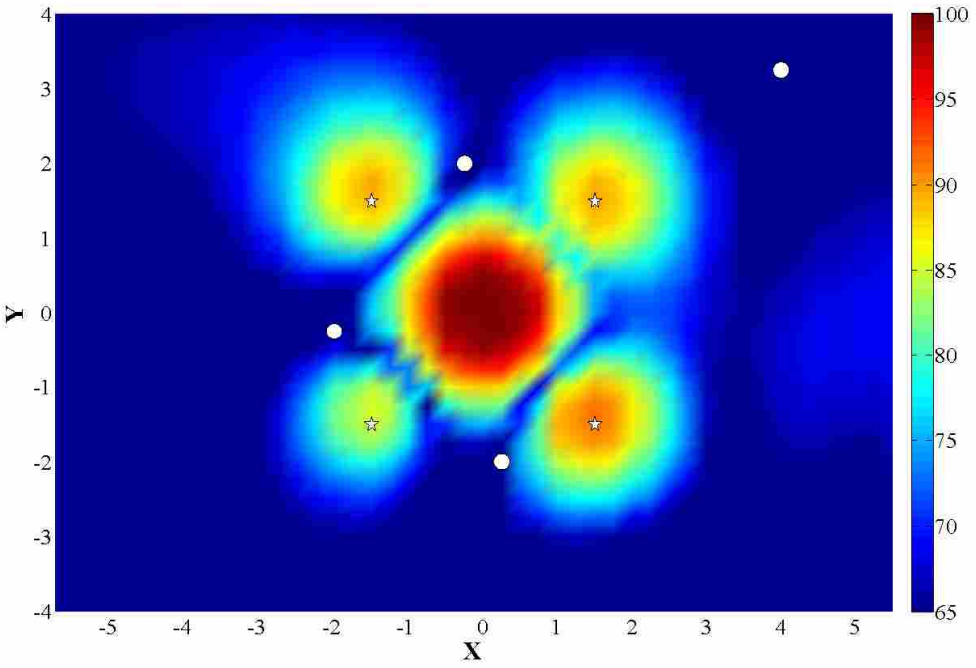

Figure 5-30: A near-field measurement (dB ref. 20 µPa) of the four-by-four ANC system for the 50-mm loudspeaker at 622 Hz and 1/4" above the source, with one error sensor out-of-place. White circles mark the locations of the error sensors. Axes units are in inches.

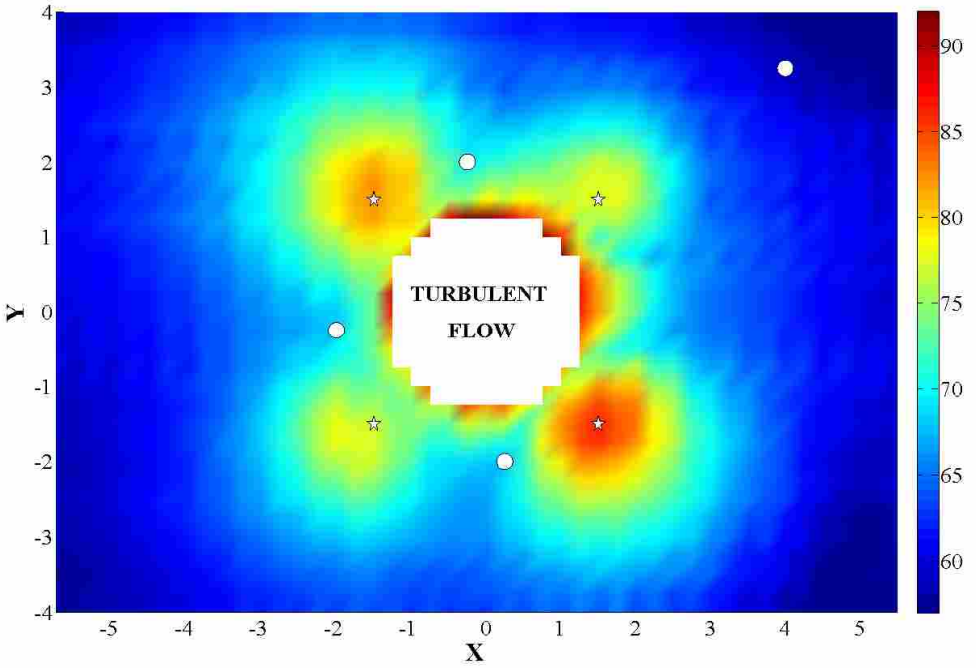

Figure 5-31: A near-field measurement (dB ref. 20 µPa) of the same ANC system as in Fig. 5-30, but for an axial cooling fan at its BPF (622 Hz) and 1/4" above the source. White circles mark the locations of the error sensors. Axes units are in inches.

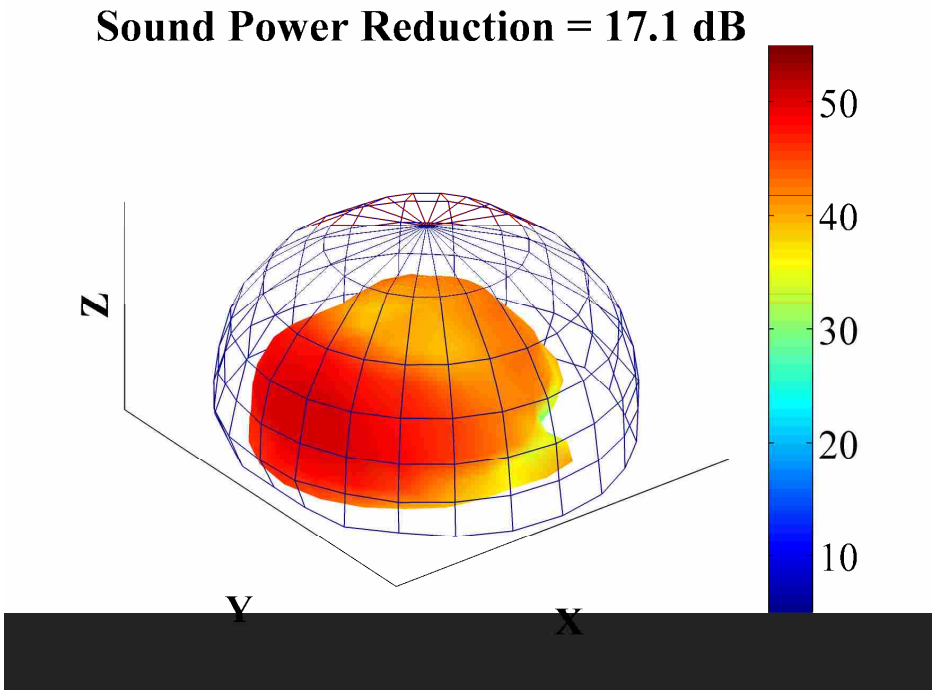

Figure 5-32: A far-field plot of the four-by-four ANC system, when one error sensor is out-of-place, with (color) and without (wire mesh) control of the 50-mm loudspeaker source at 622 Hz. Axes units are in dB ref. 20 µPa.

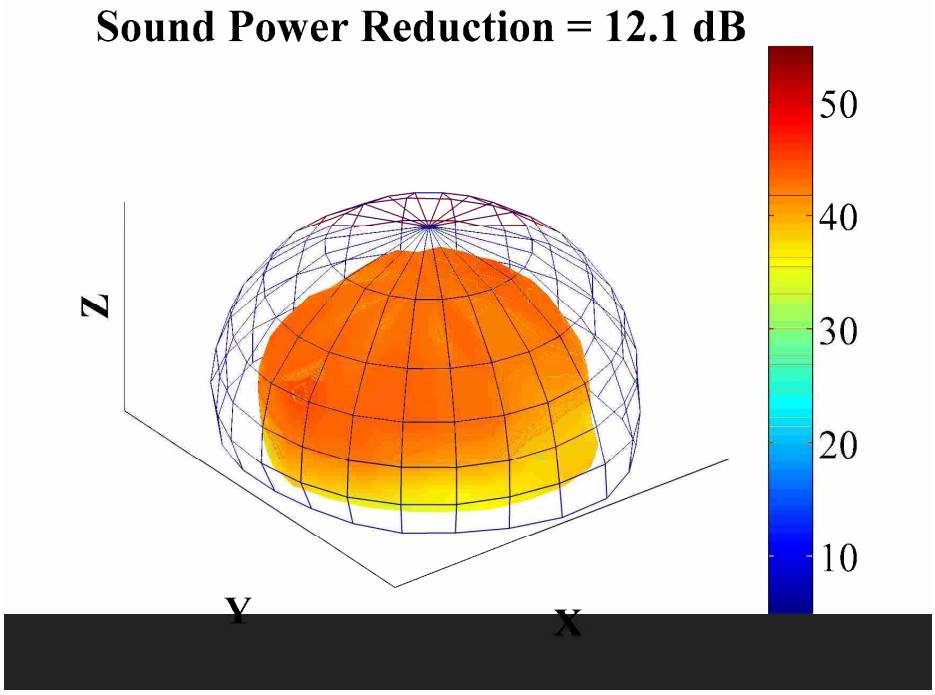

Figure 5-33: A far-field plot of the four-by-four ANC system, when one error sensor is out-of-place, with (color) and without (wire mesh) control of the axial cooling fan at its BPF of 622 Hz. Axes units are in dB ref. 20 µPa.

reduction, the map of the near-field did change slightly. In the case of the axial cooling fan, the pressure amplitude of the control actuator in the top right portion of the near-field map was greatly decreased, resulting in a rather large change of near-field pressure for that portion of the map when compared to the pressure map in Figure 5-26.

5.3.3. NEAR FIELD FOR IDEAL VS. NON-IDEAL SENSOR LOCATIONS

To test the actual effects of error sensor placement on far-field global attenuation, the error sensors were placed in locations on the plate that were completely outside of any theoretically predicted pressure null. The source used for this test was the 50-mm loudspeaker. The near-field measurement for this error sensor placement, shown in Figure 5-34, shows drastic changes in the near-field pressure in comparison to Figure

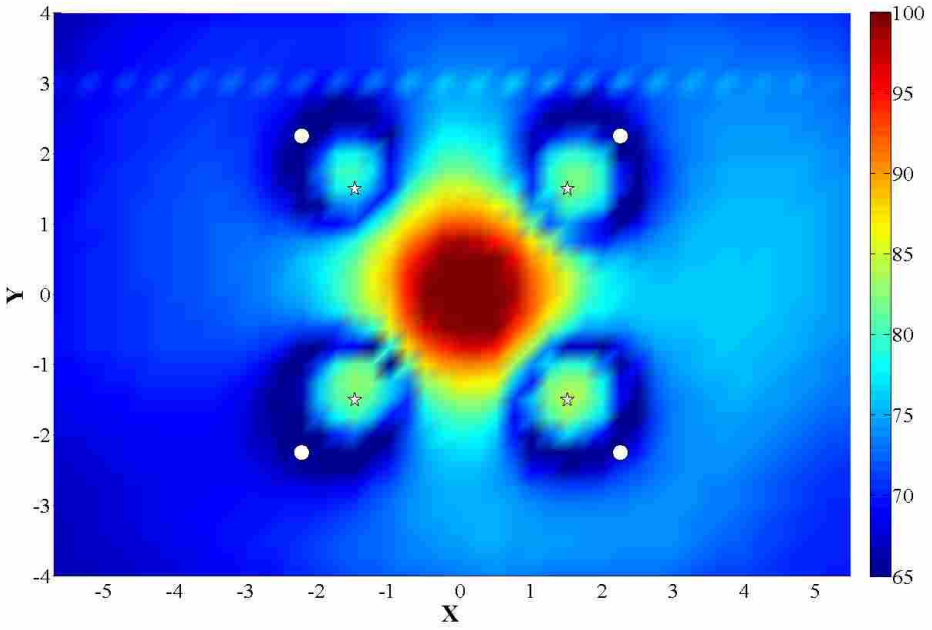

Figure 5-34: A near-field measurement (dB ref. 20 µPa) of the four-by-four ANC system for the 50-mm loudspeaker at 622 Hz and 1/4" above the source, with error sensors at non-ideal locations. White circles mark the locations of the error sensors. Axes units are in inches.

5-25. Since both pressure maps are plotted on the same scale, it appears that the sound pressure in the near field is not as reduced when the error sensors are placed at non-ideal locations.

5.3.4. FAR FIELD FOR IDEAL VS. NON-IDEAL SENSOR LOCATIONS

A plot of the far-field global sound pressure level reduction in ANC for the primary loudspeaker source best illustrates the importance of placing the error sensor within the theoretically predicted pressure nulls. Figure 5-35 shows the global sound power reduction of the ANC system plotted in Figure 5-34, with error sensors at non-ideal locations. With a standard deviation of only 0.1 dB for the loudspeaker ANC measurements, the decrease in average global reduction from 17.1 dB to 9 dB is quite significant and the BPF tone for this case was perceptibly louder than the previous ANC measurements.

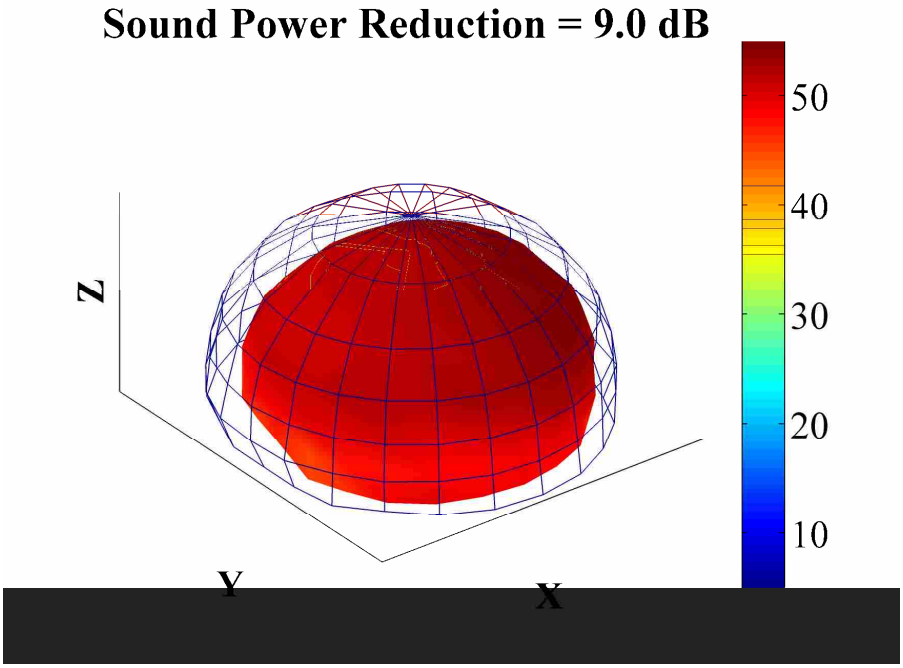

Figure 5-35: A far-field plot of the four-by-four ANC system, when all the error sensors are in non-ideal locations (Fig. 5-34), with (color) and without (wire mesh) control for a 50-mm loudspeaker at 622 Hz. Axes units in dB ref. 20 µPa.

CHAPTER 6

MULTIPOLE EXPANSIONS AND FAN NOISE ANC

6.1. PRELIMINARY TESTS IN MULTIPOLE EXPANSIONS

An ME requires complex pressure data measured over a sphere or hemisphere. A hemisphere was measured using the angular microphone array described in Chapter 5, Section 5.2.3. The complex pressure was obtained by calculating the transfer function between a reference microphone and every other microphone on the array. The reference microphone chosen was microphone seven, or the central and stationary microphone. The power spectrum of the reference microphone was used in the following equation to obtain complex pressure data at each of the other microphone positions:

$$\hat{y}_n = \left|x_{ref}\right| \hat{H}_n(\omega) \tag{6-1}$$

where $\hat{y}_n$ is the complex data measured at the n^{th} microphone position, $\left|x_{ref}\right|$ is the square root of the reference microphone's power spectrum, and $\hat{H}_n(\omega)$ is the transfer function between the reference microphone and the n^{th} microphone.

6.1.1. TWO TEST CASES

To examine the accuracy of the ME, two test cases were created. In one, a 50-mm loudspeaker was mounted in the plate and box previously used for ANC measurements (Figure 5-8). The excitation signal used for the loudspeaker was a 100-ms periodic chirp from 250 to 6000 Hz. The complex pressure in the far field of the

loudspeaker was measured using the procedures previously explained in Section 5.2.3 and Section 6.1. Using the method described in Section 4.3.1, the contribution from each individual source distribution was calculated and the pressure field was reconstructed. Figure 6-1 shows the hemisphere of both the original pressure measurement and the reconstruction for the loudspeaker source at 550 Hz. The error (in dB) between the measurement and reconstruction at this frequency was calculated and plotted on a three-dimensional surface and is shown in Figure 6-2. The mean error for the reconstruction was 0.3 dB. The relative contribution from each of the individual multipole sources at 550 Hz is shown in Figure 6-3. All of the theoretically calculated far-field plots shown in this chapter are generated with the exact same angular resolution as the measurements made with the semi-circular microphone array.

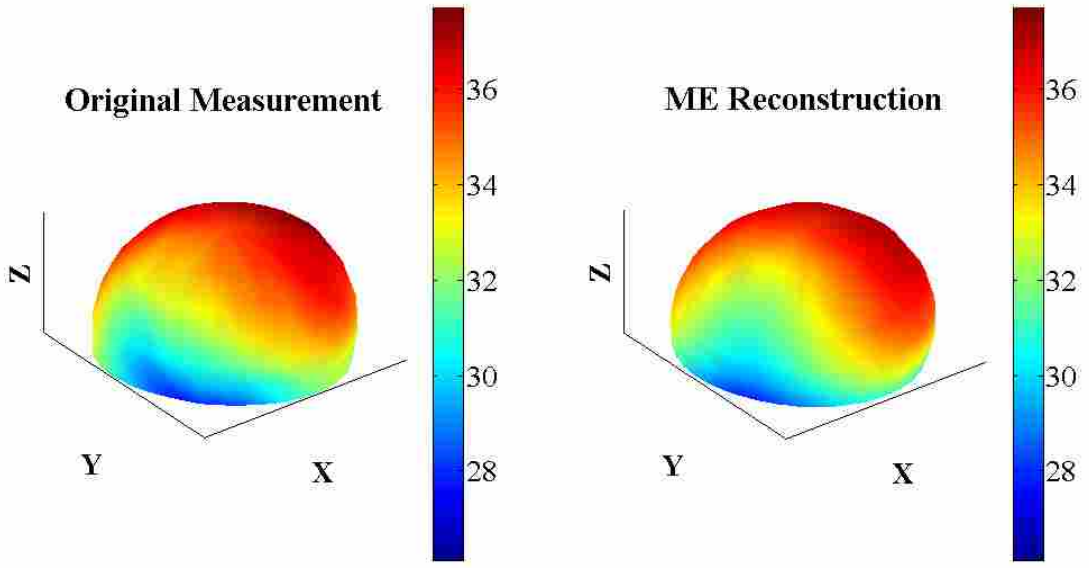

Figure 6-1: A far-field plot of the original pressure measurement and the reconstruction from a ME for a loudspeaker source at 550 Hz. The color scale is the same for both plots. Axes units are in dB ref. 20 µPa.

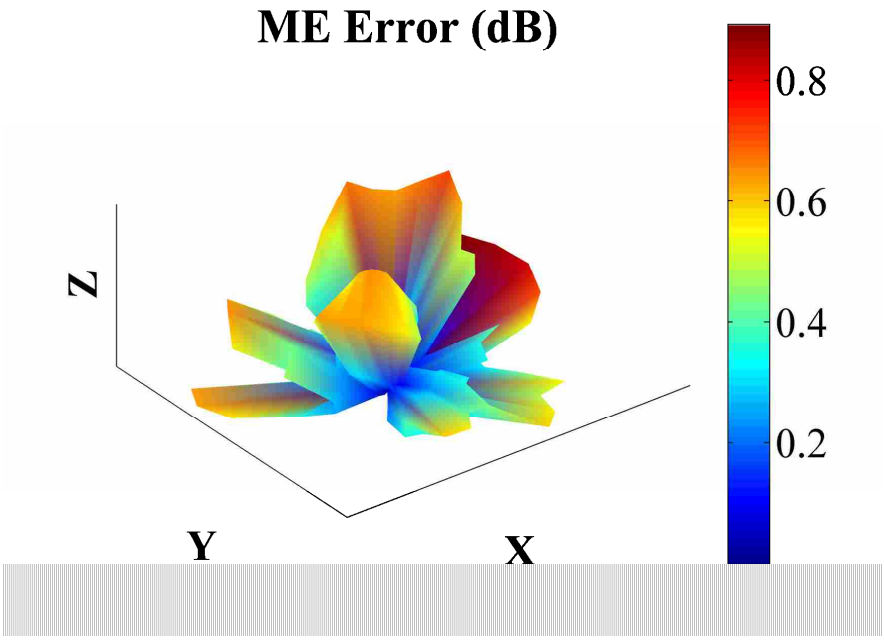

Figure 6-2: A surface plot of the dB error for the ME of the loudspeaker measurement at 550 Hz. Axes units are in dB ref. original measurement.

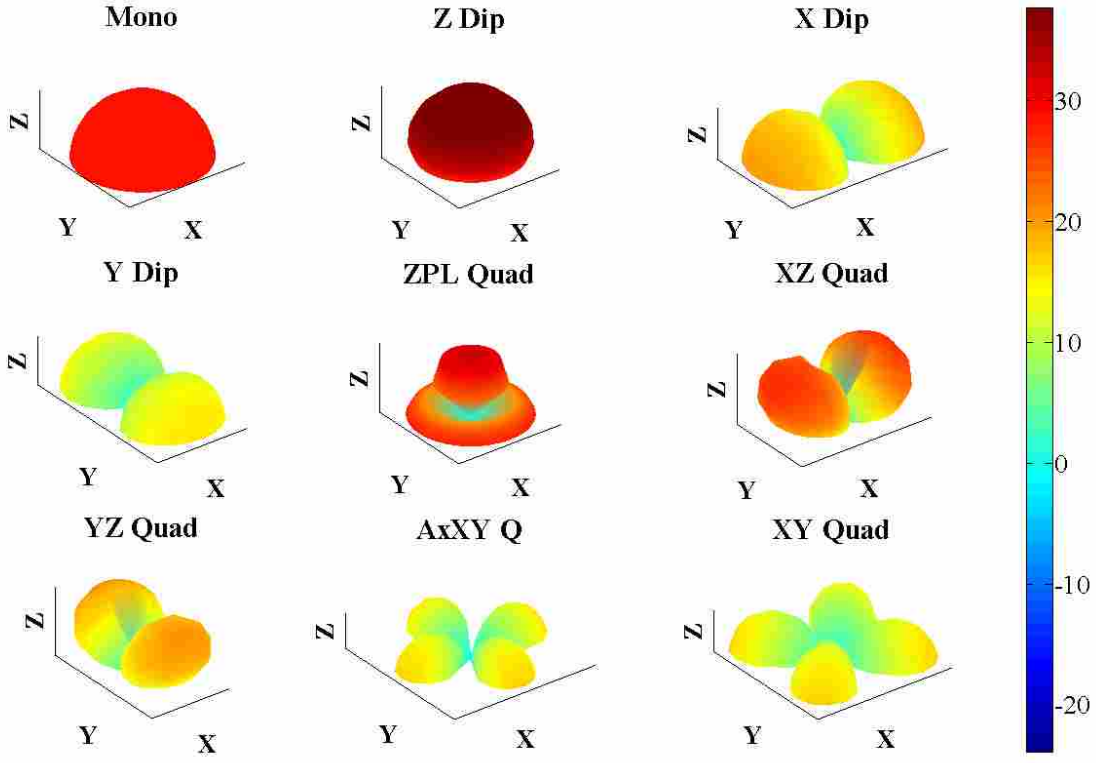

Figure 6-3: The relative contribution from each multipole source in the ME of the loudspeaker source at 550 Hz. Axes units are in dB ref. 20 µPa.

The second test that was created involved measurement of a dipole sound source. Two 25-mm loudspeakers were mounted in the plate and box. The two loudspeakers were wired so that one of them radiated pressure out of phase with the other. The loudspeakers were spaced a distance of 4 1/4″ apart. Again, a 100-ms periodic chirp was used for the excitation signal from 100 Hz to 3000 Hz. A frequency of 550 Hz was used in the generation of each plot. Plots of the original and reconstructed pressure fields, error (in dB), and relative contribution of multipole sources for this test case at 550 Hz are shown in Figures 6-4 through 6-6. The mean error for the reconstruction was 0.2 dB.

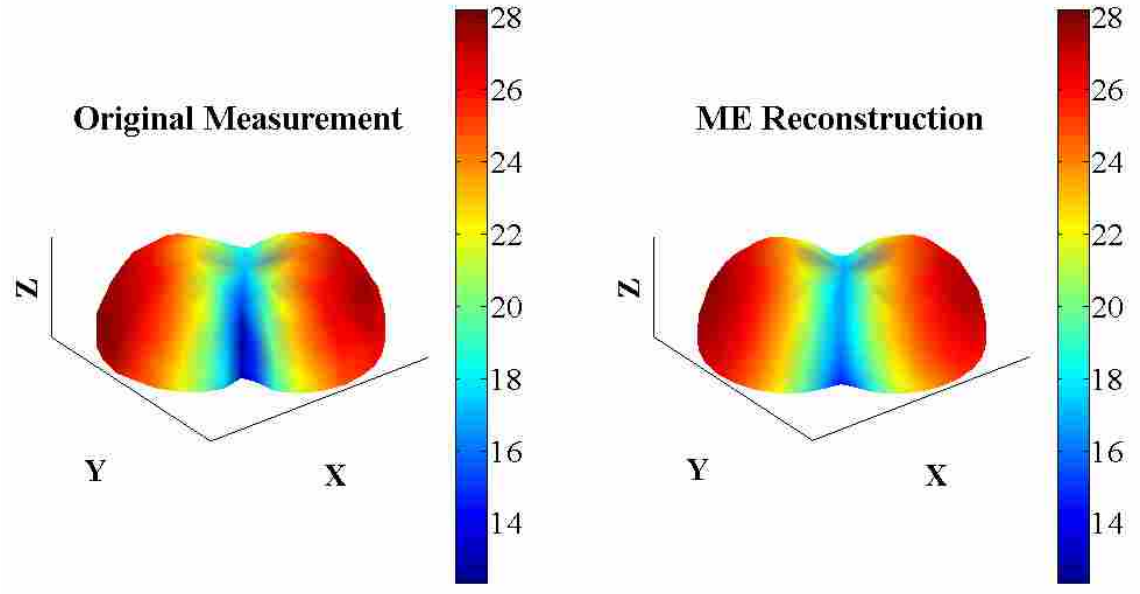

Figure 6-4: A far-field plot of the original pressure measurement and the reconstruction from a ME for a dipole source situated 45° from the *x*- and *y*- axes at 550 Hz. The color scale is the same for both plots. Axes units are in dB ref. 20 µPa.

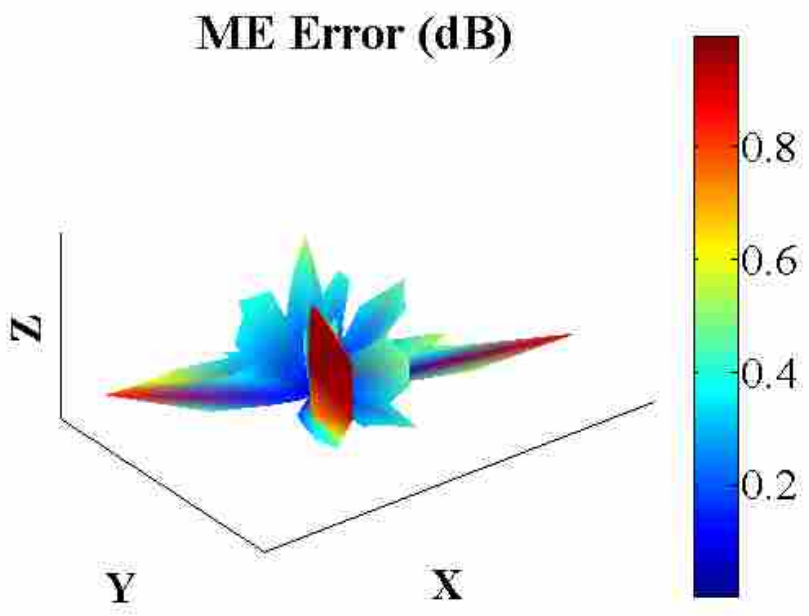

Figure 6-5: A surface plot of the dB error for the ME of the dipole measurement at 550 Hz. Axes units are in dB ref. original measurement.

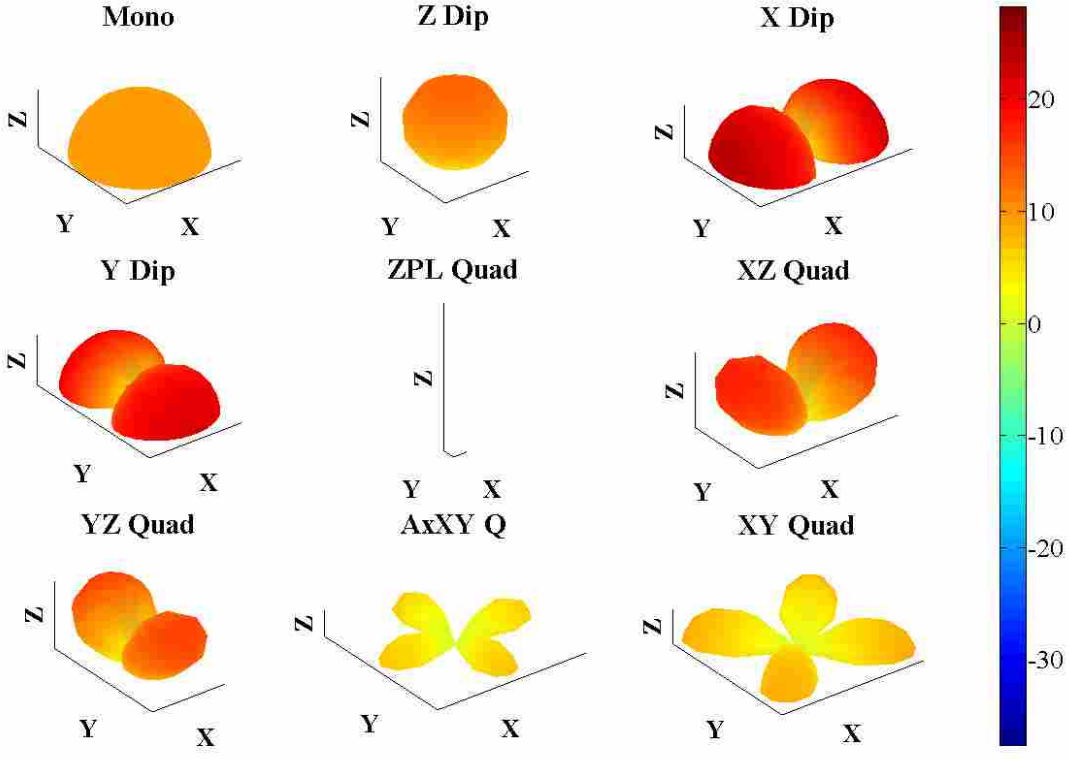

Figure 6-6: The relative contribution of each multipole source in the ME of the dipole measurement at 550 Hz. Axes units are in dB ref. 20 µPa.

6.1.2. DISCUSSION OF TEST CASE RESULTS

The monopole loudspeaker source was expected to have a more uniform pressure over the measurement hemisphere. As illustrated in Figure 6-1, the pressure was not completely uniform over the hemisphere measurement surface. A possible explanation for this is that the loudspeaker source was installed without mounting a sealed cap on the body of the loudspeaker. Perhaps some of the negative pressure from the back of the loudspeaker was exposed to the semi-circular array. All other loudspeakers in the plate were mounted with caps that were sealed to the aluminum plate. Although the loudspeaker did not radiate as much like a monopole as expected, the ME was still accurate at the measurement location within less than 0.5 dB on average. It is apparent in Figure 6-3 that the greatest contributors to the radiation of the loudspeaker were the monopole, z-axis dipole, and z-axis pseudo-longitudinal quadrupole.

The ME for the dipole, as shown in Figure 6-4, was highly accurate. Upon observing the relative contributions from each source distribution in Figure 6-6, it is apparent that the greatest contributors to the radiation of this particular dipole source were the x- and y-axis dipoles, and the xz-plane and yz-plane quadrupoles. It is conceptually reasonable that a dipole which is off-axis in the xy-plane, according to the coordinate system of the ME, would yield dominant contributions from each of the multipoles whose primary radiation protrudes from that same plane.

6.2. THE MULTIPOLE EXPANSION OF AN AXIAL COOLING FAN

6.2.1. MULTIPOLE FAN MODEL

The same procedure used in the ME of the test cases was used in calculating the values of the source strengths and the relative contributions of each multipole for an axial cooling fan with a BPF of 659 Hz. The ME was used to model the BPF of the fan as well as its second and third harmonics. Plots of the original and reconstructed pressure fields and dB error for the BPF of the fan are shown in Figures 6-7 through 6-9. The mean dB error for the BPF of the axial fan was 0.3 dB. The relative contributions of the fan multipoles showed that the monopole, *z*-axis dipole, and *y*-axis dipole were the greatest contributors to the fan noise.

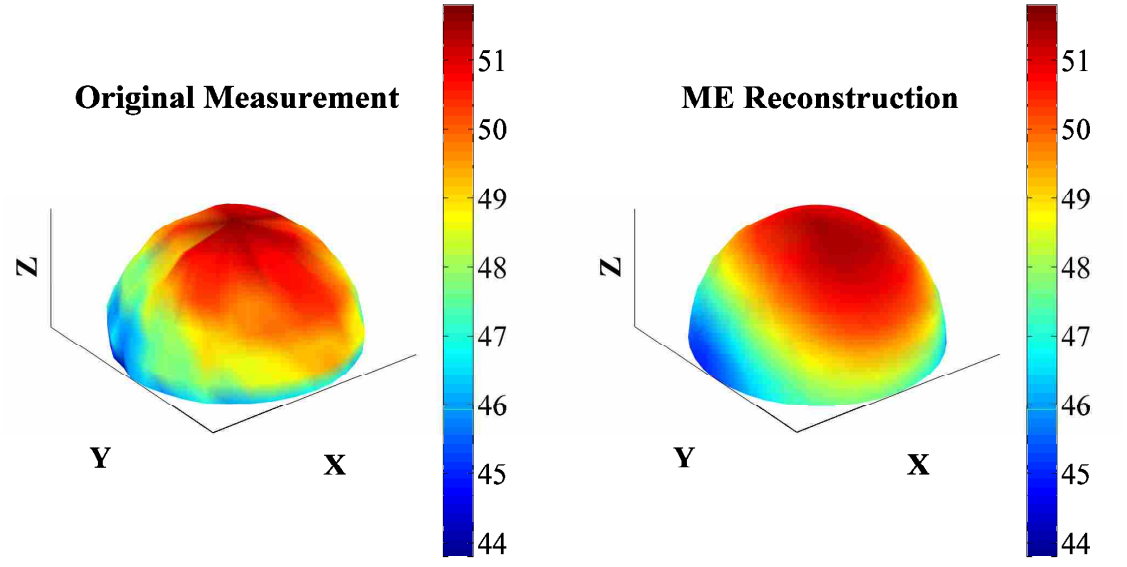

Figure 6-7: A far-field plot of the original pressure measurement and the reconstruction from an ME for the BPF (659 Hz) of an axial cooling fan. The color scale is the same for both plots. Axes units are in dB ref. 20 µPa.

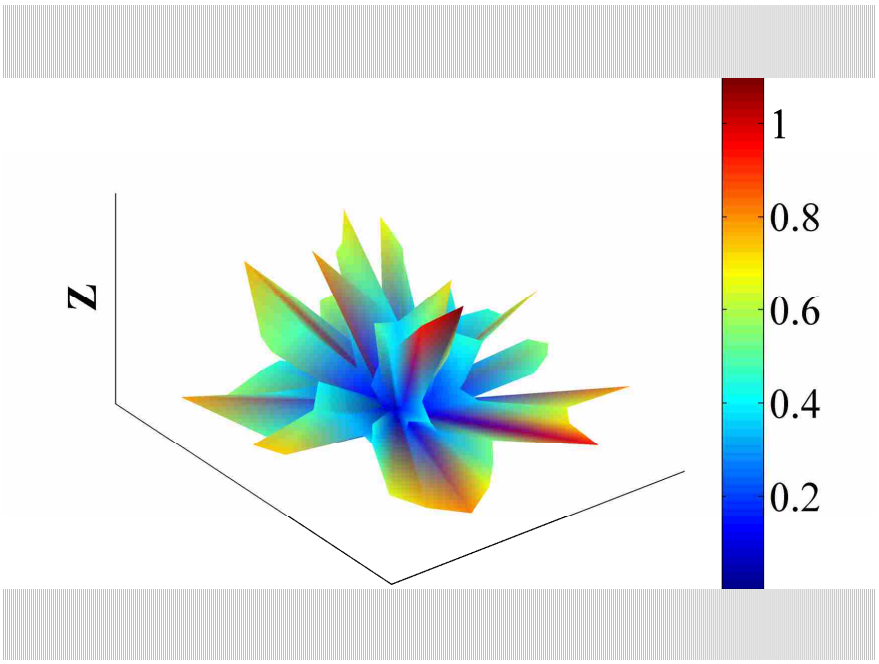

Figure 6-8: A surface plot of the dB error for the ME of the axial fan BPF (659 Hz) measurement. Axes units are in dB ref. original measurement.

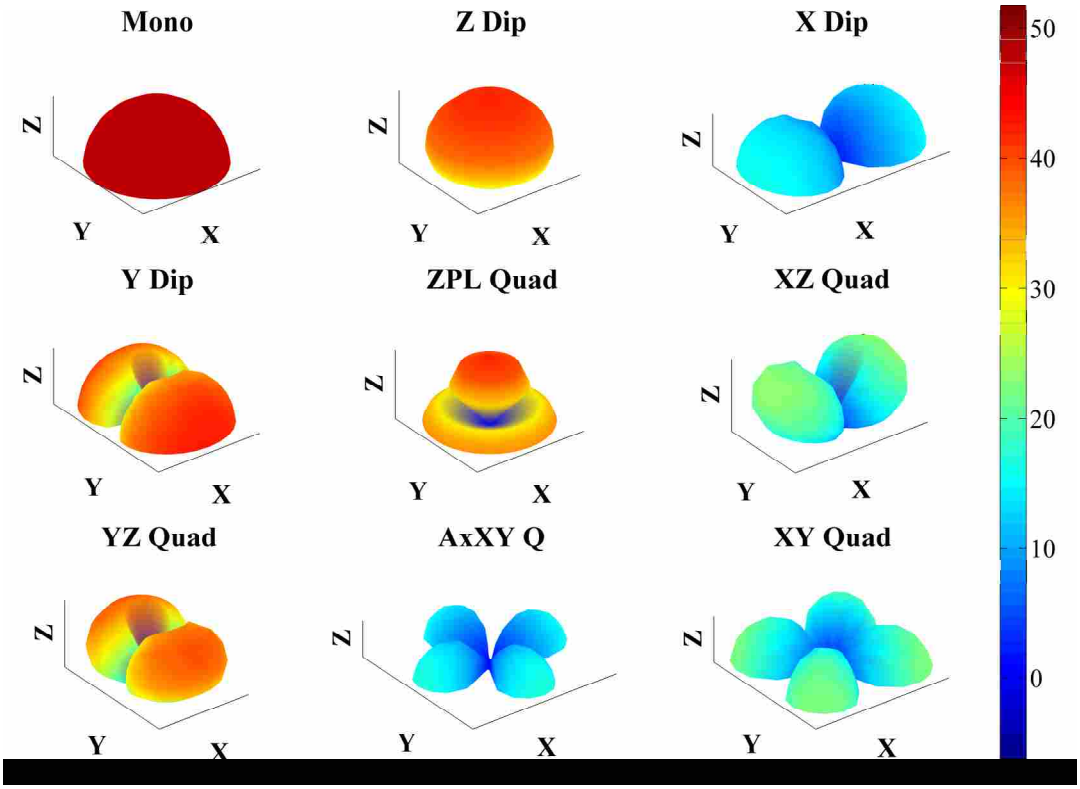

Figure 6-9: The relative contribution of each multipole source in the ME of the axial fan BPF (659 Hz) measurement. Axes units are in dB ref. 20 µPa.

6.2.2. CHANGES IN PRESSURE NULLS FOR A MULTIPOLE FAN

Using the data obtained from the multipole reconstruction of the BPF of the axial fan, the relative magnitude and phase of each of the 19 point sources in the multipole distribution was calculated using Eq. 4-7 and the process described in Section 4.3.1. The characteristics of each multipole are illustrated in Figure 4-1 and Table 4-1. The source strengths were used to plot the radiated pressure of the fan in the near field. A theoretical plot of the pressure magnitude for the axial fan modeled at the BPF as a multipole point source distribution is shown in Figure 6-10. The actual pressure magnitude radiated by the axial fan was measured and is plotted in Figure 6-11. The theoretical map of pressure for the ME model, shown in Figure 6-10, and the fan measurement, shown in Figure 6-11, both display an offset monopole-

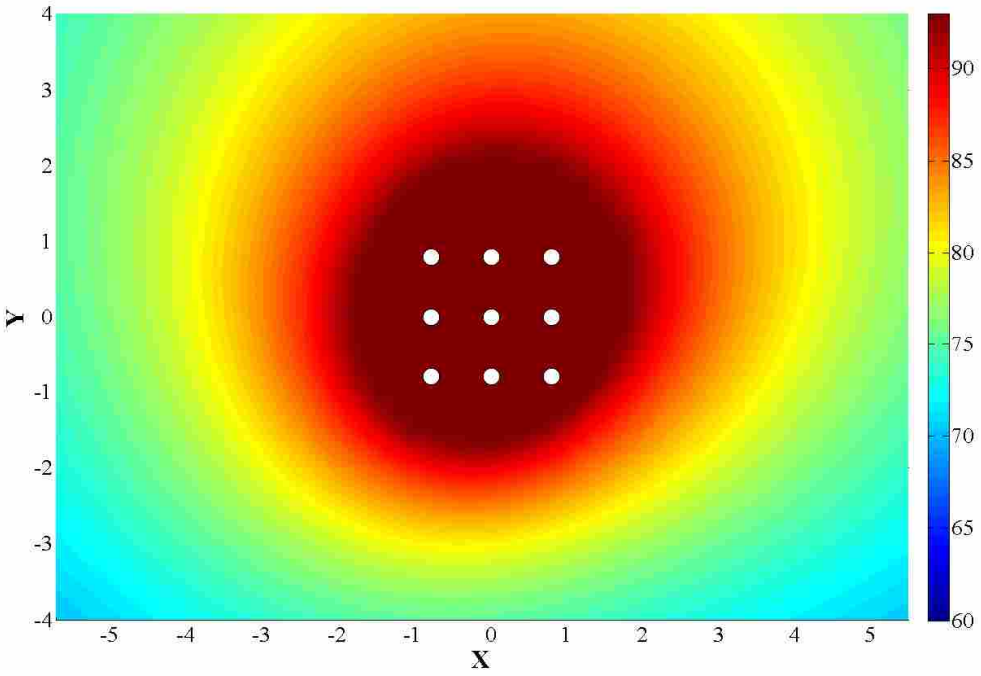

Figure 6-10: A theoretical map of the radiated pressure (dB ref. 20 µPa) in the xy plane 1/4″ above the ME model point source distribution of an axial fan at its 659 Hz BPF. The white circles mark the locations of ME model point sources in the plane of the fan. Axes units are in inches.

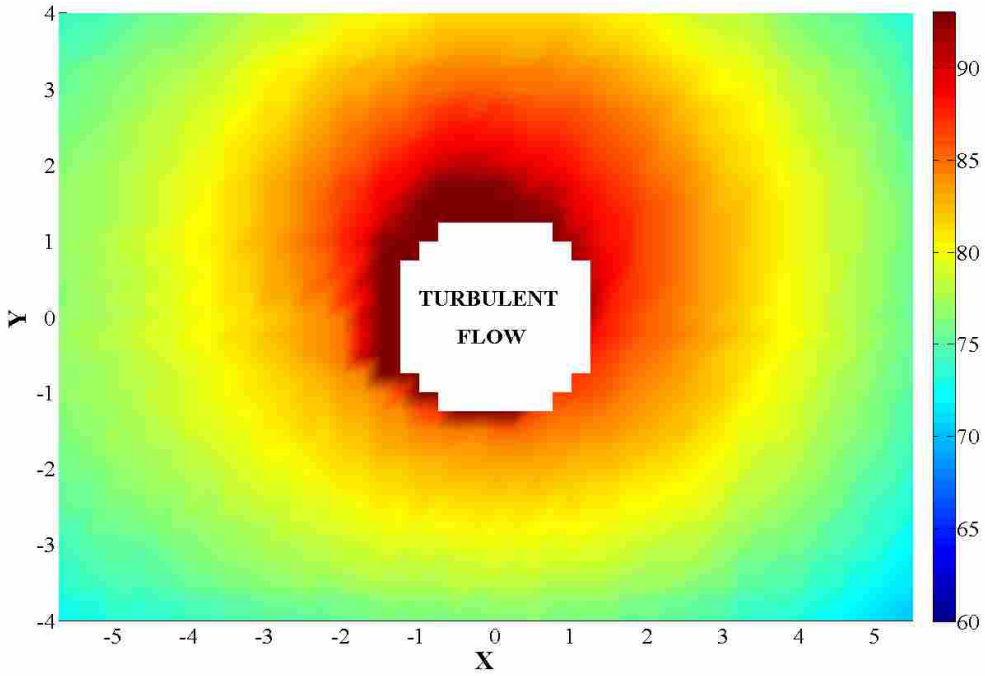

Figure 6-11: A near-field map (dB ref. 20 µPa) of the measured radiated pressure of an axial fan at its BPF (659 Hz) and 1/4″ above the source. Axes units are in inches.

q	Magnitude	Phase (degrees)
q_m	0.0000235	117.53
q_{dz}	0.0000268	-58.56
q_{dx}	0.0000014	167.20
q_{dy}	0.0000286	-75.92
q_{zplq}	0.0003276	-69.34
q_{xzq}	0.0000124	144.78
q_{yzq}	0.0000819	51.40
q_{Axq}	0.0000046	-56.28
q_{xyq}	0.0000067	3.44

Table 6-1: The magnitude and relative phase of each multipole point source in the ME for the BPF (659 Hz) of an axial cooling fan.

like distribution. The presence of measurement noise in Figure 6-11 cause the magnitude of similitarity between this figure and Figure 6-10 difficult to determine. A table of the magnitude and phase of each source strength calculated in the ME for the fan BPF (659 Hz) is provided in Table 6-1.

The theoretical near-field pressure magnitude in dB (referenced to the pressure field of the distributed source) for a minimization of sound power for the distributed axial fan source and the four control actuator ANC configuration is shown in Figure 6-12. Figure 6-13 shows the pressure map for this same 4-by-4 ANC configuration when referenced to 20 μPa. The predicted error sensor placement found in Figure 6-12 is completely different in comparison to the prediction of error sensor placement for a single monopole point source, as shown in Figure 5-22. A plot of the optimum sound power reduction for the ANC of the ME model shows that the expected reduction of the BPF (659 Hz) of the multipole fan source is 8 dB. Figure 6-14 is a plot of the optimum sound power reduction for the ME model in a range of frequencies.

As noted in Figure 6-12, the near-field prediction does not offer many locations for error sensor placement. According to the figure, the error sensors should all be located only in the top half of the measurement plane. Also, Figure 6-14 dictates that the optimum achievable sound power reduction should only be about 8 dB. The achievable reduction predicted by the distributed source model is far less than the reductions that have been experimentally achieved on the BPF of an axial cooling fan. This result is explored further in Section 6.3.

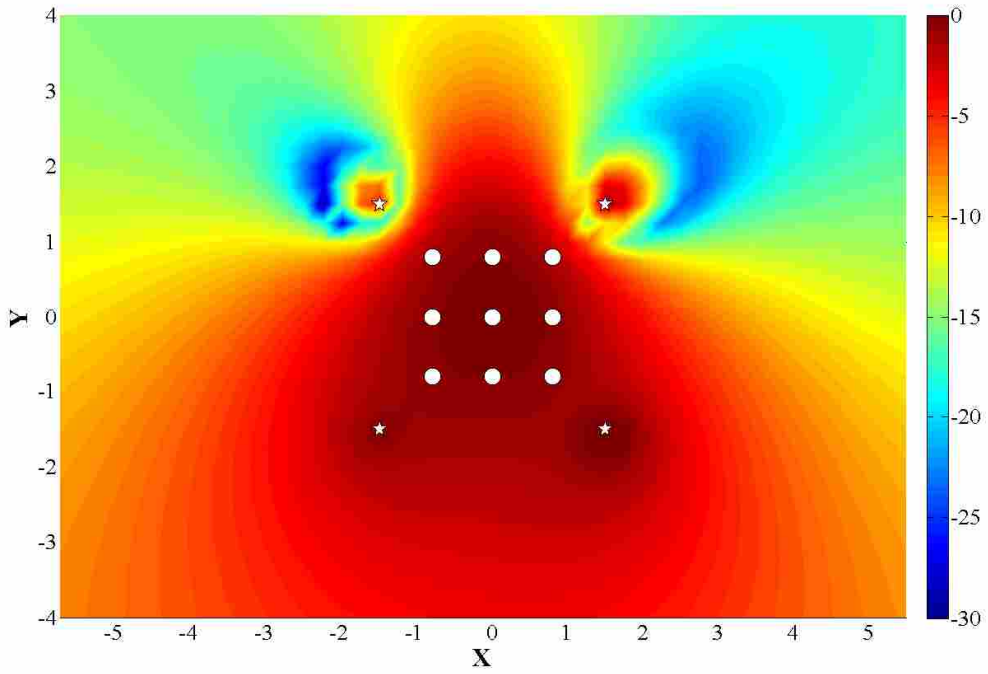

Figure 6-12: A theoretical map of the near-field pressure (dB ref. primary source pressure field) due to sound power minimization of the ME model (circles) of an axial fan at its BPF (659 Hz) and four control actuators (stars) on a plane 1/4″ above the source. Axes units are in inches.

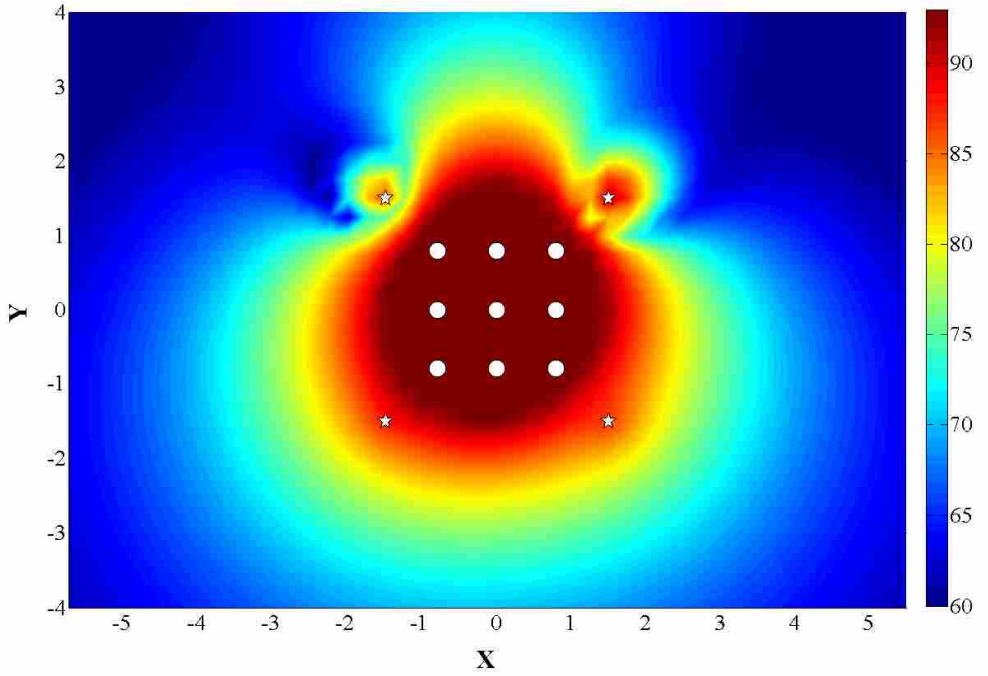

Figure 6-13: A theoretical map of the near-field pressure (dB ref. 20 µPa) due to sound power minimization of the ME model (circles) of an axial fan at its BPF (659 Hz) and four control actuators (stars) on a plane 1/4″ above the source. Axes units are in inches.

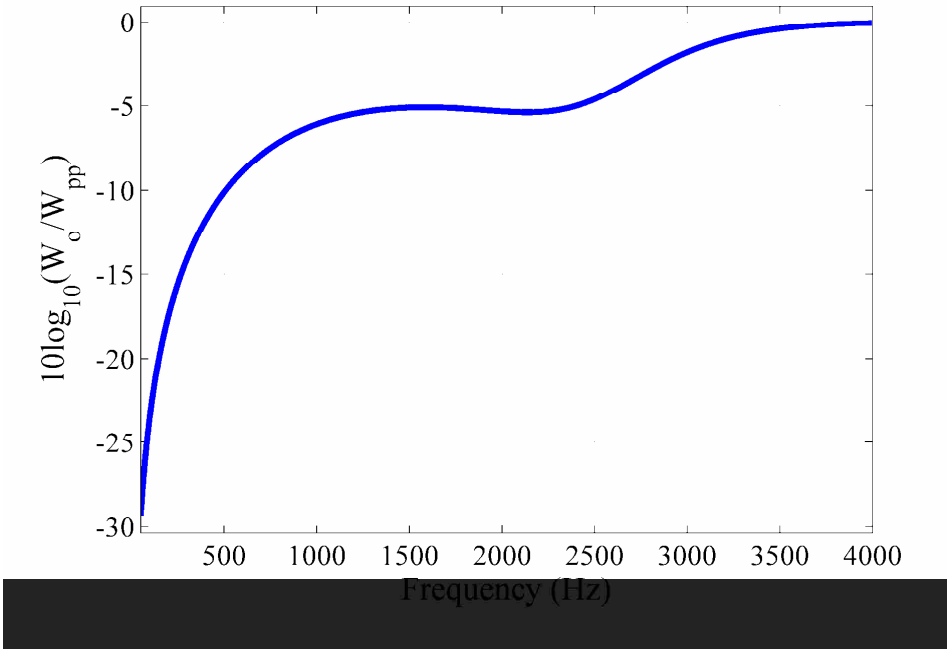

Figure 6-14: A plot of the minimum power output in dB (ref. sound power of the primary source) vs. frequency for 4-by-4 ANC of the ME model of fan noise.

6.3. MULTIPOLE FAN NOISE SENSOR PLACEMENT RESULTS

6.3.1. NEAR-FIELD COMPARISONS

ANC was applied to the axial fan using the two different error sensor locations that were found by minimizing sound power for the point monopole source and for the multipole source with four control actuators and four error sensors. Figure 5-23 represents the error sensor placement for a point monopole sound power minimization and Figure 6-12 represents the same scenario but with the primary source modeled as a multipole. As noted in this figure, the optimum location of error sensors would be solely in the top half of the measurement plane. An attempt was made to place all of the error sensors in the top half of the measurement plane. With the error sensors in these locations the ANC system was extremely inefficient in reducing the sound power of the cooling fan at its 659 Hz BPF. A plot of the far field

sound power reduction for this case is shown in Figure 6-15. Because the global reduction was so poor with the error sensors in the top half of the plane, two of them were placed in the bottom half of the plane, but in random locations relatively far away from the control actuators. The error sensor predictions determined by the point source model and ME model of fan noise were tested and maps of the measured near-field pressure resulting from ANC of the axial fan are shown in Figures 6-16 and 6-17. The circles on each figure mark the error sensor locations used according to each model.

The error sensor placement that was determined using the ME model of fan noise appeared to produce a similar near-field radiated pressure to the point primary source model. The top half of Figure 6-17 somewhat resembles the theoretical

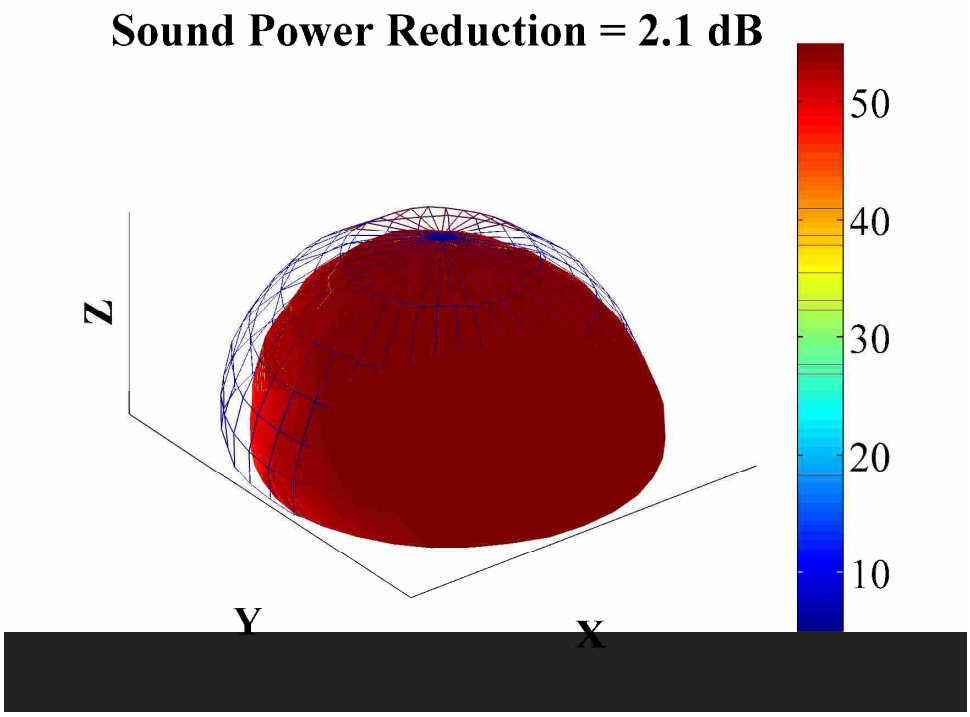

Figure 6-15: The far-field measurement with (color) and without (wire mesh) 4-by-4 ANC of the axial fan at its BPF of 659 Hz and with error sensor in the top half of the measurement plane, according to the ME model of fan noise. Axes units are in dB ref. 20 µPa.

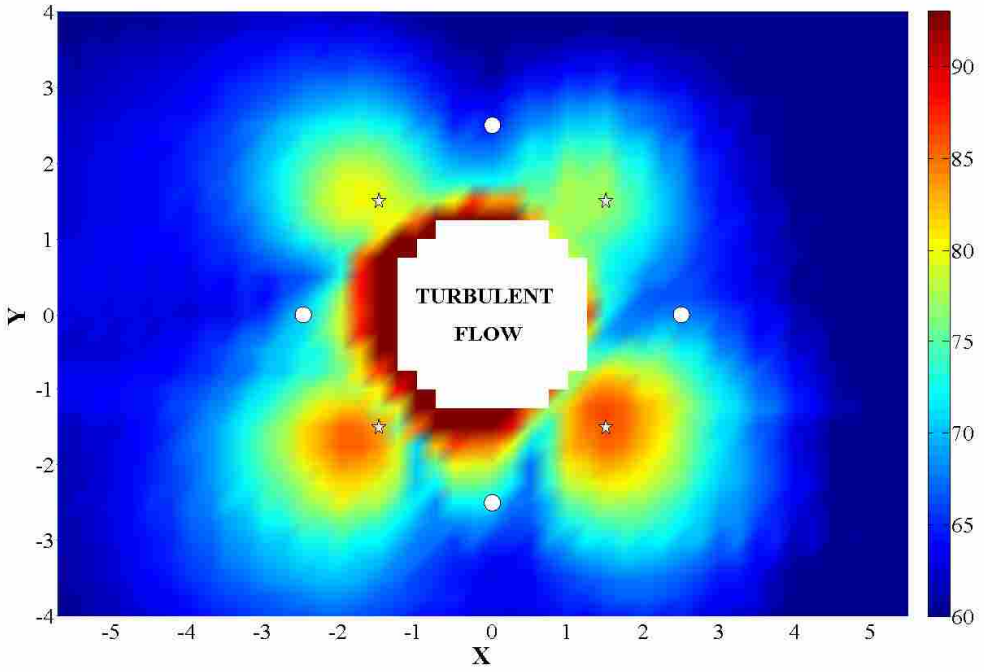

Figure 6-16: The measured near-field radiated pressure (dB ref. 20 µPa) due to sound power minimization for the axial fan at its BPF (659 Hz) and 1/4″ above the source. Error sensors (white circles) were placed according to the point source model. Axes units are in inches.

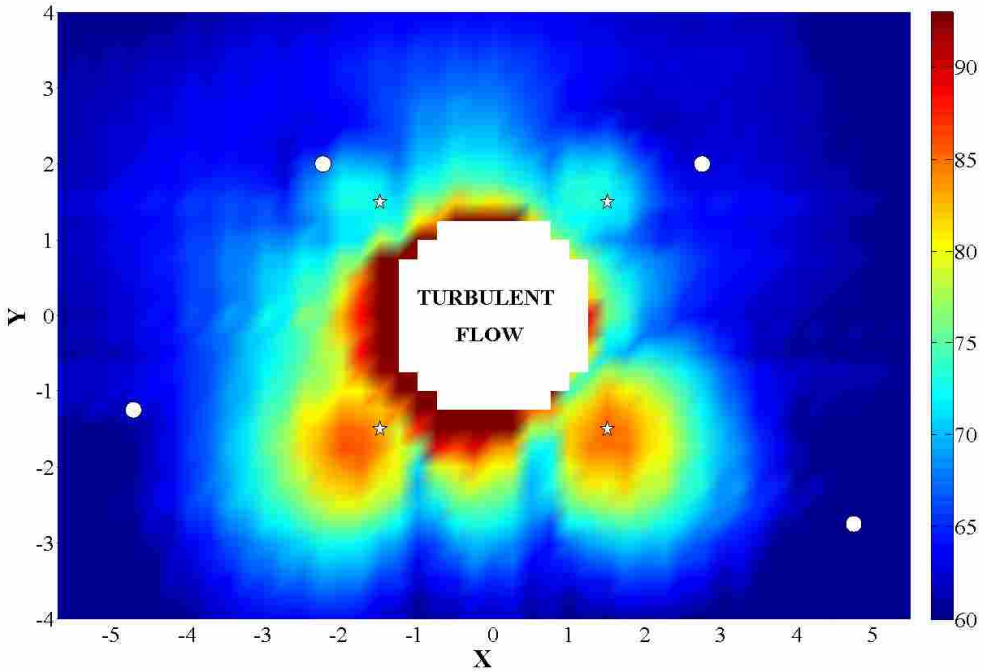

Figure 6-17: The measured near-field radiated pressure (dB ref. 20 µPa) due to sound power minimization for the axial fan at its BPF (659 Hz) and 1/4″ above the source. The top two error sensors (white circles) were placed according to the ME model. Axes units are in inches.

prediction shown in Figure 6-13. However, in the bottom half there are nulls in between the control actuators that were not predicted in the ME for the fan. Also, the power spectrum of the error sensor signals with control in the ME positions showed large reductions to dB levels much lower than the broadband noise floor. This was not the case with the error sensor in locations according to the point source model.

6.3.2. FAR-FIELD GLOBAL ATTENUATION

The global sound power attenuation for ANC of the axial fan with error sensor placement according to both the point source and ME model of fan noise was measured using the semi-circular array. Figures 6-18 and 6-19 show these far-field measurements. For ten measurement ensembles with thirty averages each, the standard deviation was calculated as 0.1 dB. The sound power reduction of the fan with error sensors placed according to the point source model was 20.4 dB. The sound power reduction of the fan when error two of the error sensors were placed according to the ME model was only 14.1 dB. In comparison, the placement of error sensors according to the ME model was not optimum for far-field sound power reductions. To gain further understanding of how the error sensor locations for the point source model produced better results, the error sensors were placed at different locations within the theoretically predicted pressure null that occurs as a result of the minimization of sound power for point monopoles. The null locations chosen were much closer to the control actuators, similar to the error sensor locations shown in Figure 5-25. The average sound power reduction measurement for this error sensor placement was calculated to be 17.6 dB. The measurement with and without ANC

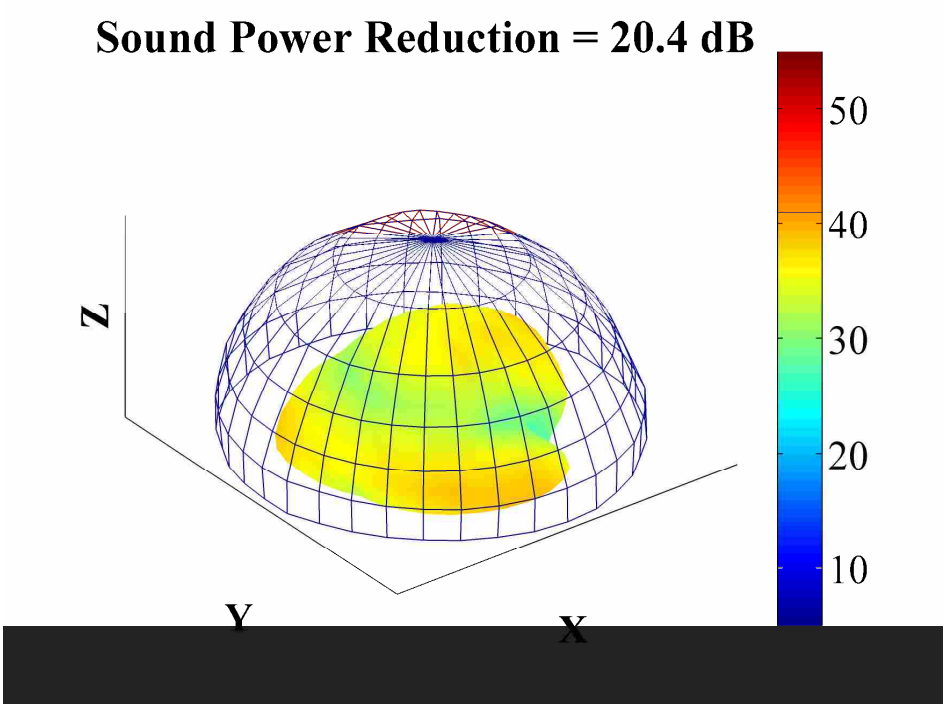

Figure 6-18: The far-field measurement with (color) and without (wire mesh) 4-by-4 ANC of the axial fan at its BPF of 659 Hz and with error sensors in the locations predicted by the point source model of fan noise. Axes units are in dB ref. 20 µPa.

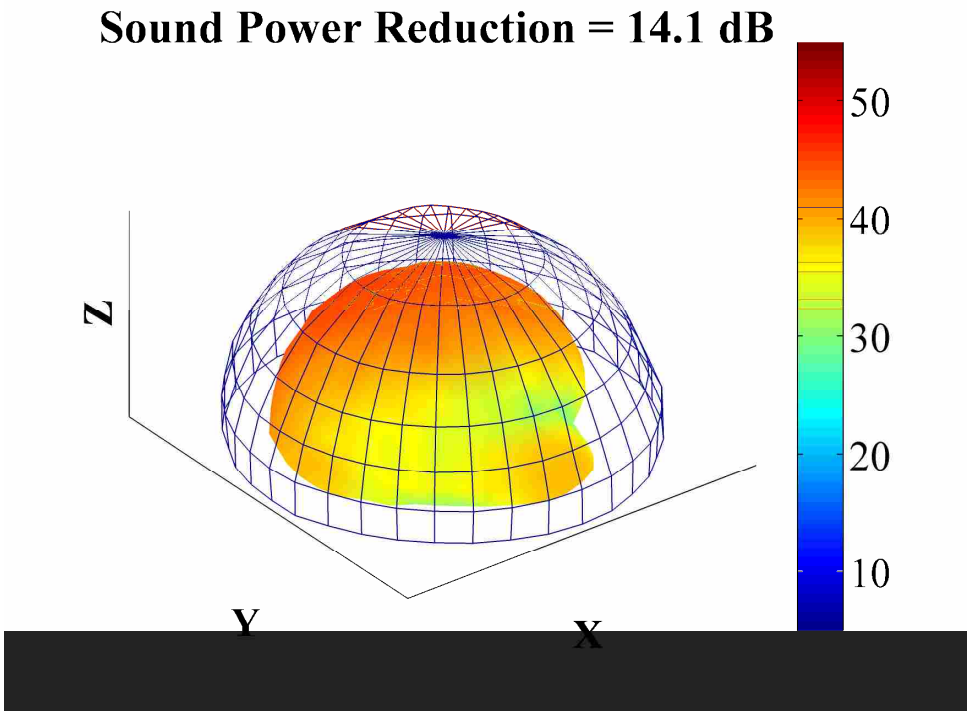

Figure 6-19: The far-field measurement with (color) and without (wire mesh) 4-by-4 ANC of the axial fan at its BPF of 659 Hz and with error sensors in the locations predicted by the ME model of fan noise. Axes units are in dB ref. 20 µPa.

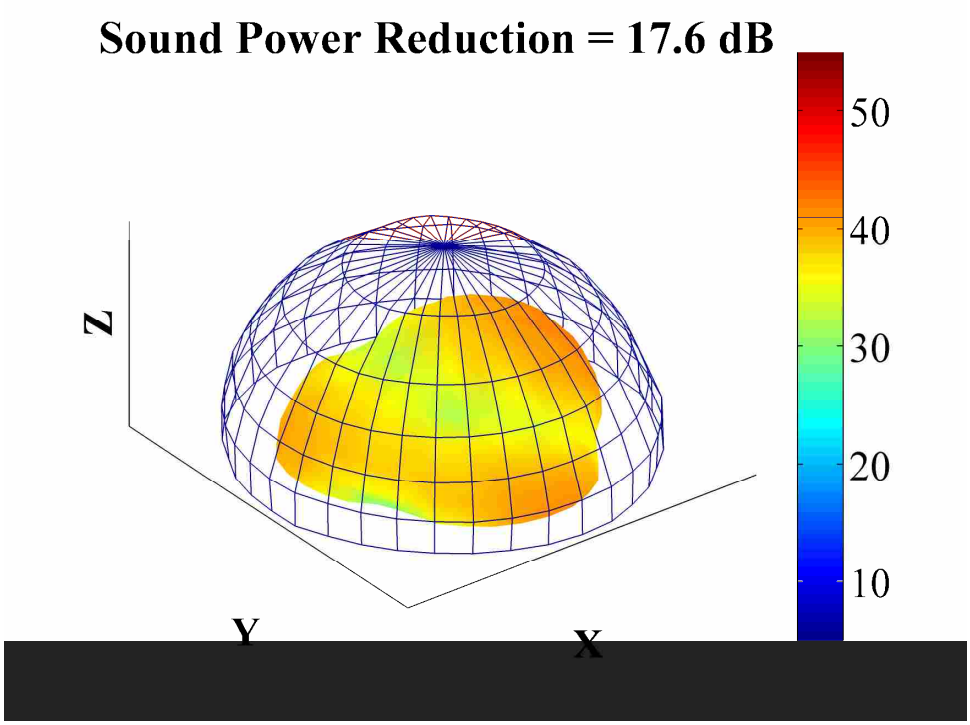

Figure 6-20: The far-field measurement with (color) and without (wire mesh) 4-by-4 ANC of the axial fan at its BPF of 659 Hz and with error sensors close to the control actuators, but still on the pressure null predicted by the point source model of fan noise. Axes units are in dB ref. 20 µPa.

is shown in Figure 6-20. In comparison, the average sound power reduction for fan ANC with error sensors placed in both the locations predicted according to the point source model performed much better than ANC with error sensors placed according to the ME model.

6.3.3 LIMITATIONS OF THE ME MODEL

The inefficacy of the ME model when used for near-field error sensor prediction led to further investigation of the ME theory, the MATLAB code used to calculate the multipole source strengths, the code used for calculating the optimum source strength of secondary (control) sources, and the calculation of minimum power output for the ANC configuration. The code was tested using some benchmark cases,

one of which was a dipole primary source and two secondary sources. The analytical solution for this case was calculated and compared to the answer from the MATLAB code. The MATLAB code calculated the optimum source strengths of the control sources as well as the minimum power output exactly as predicted by the analytical solution.

Upon finding that the code was functioning properly, another code was developed to investigate further the cause of inefficiency of the ME model. This code was designed to import the primary source strengths obtained from the ME expansion as well as the optimum source strengths of the ANC configuration, and plot the theoretical far field of the multipole noise source with and without the theoretically predicted ANC. The complex pressure field of the theoretically predicted ANC system was then imported back in the original ME code and analyzed with an ME in order to discover which multipoles, if any, were controlled for the theoretical calculation of optimum source strength and minimum power output. The results of these tests are shown and discussed further in the following paragraphs.

The theoretically produced far-field pressure for a point monopole source with and without ANC by four symmetrically placed control actuators (in the same locations as described for the 4-by-4 ANC configuration) is shown in Figure 6-21. The sound power reduction for this and every following theoretical far-field calculation is found by averaging the squared pressure without ANC and subtracting the averaged squared pressure with theoretical ANC. The theoretical far field of the ME model of fan noise with and without ANC is shown in Figure 6-22. The relative

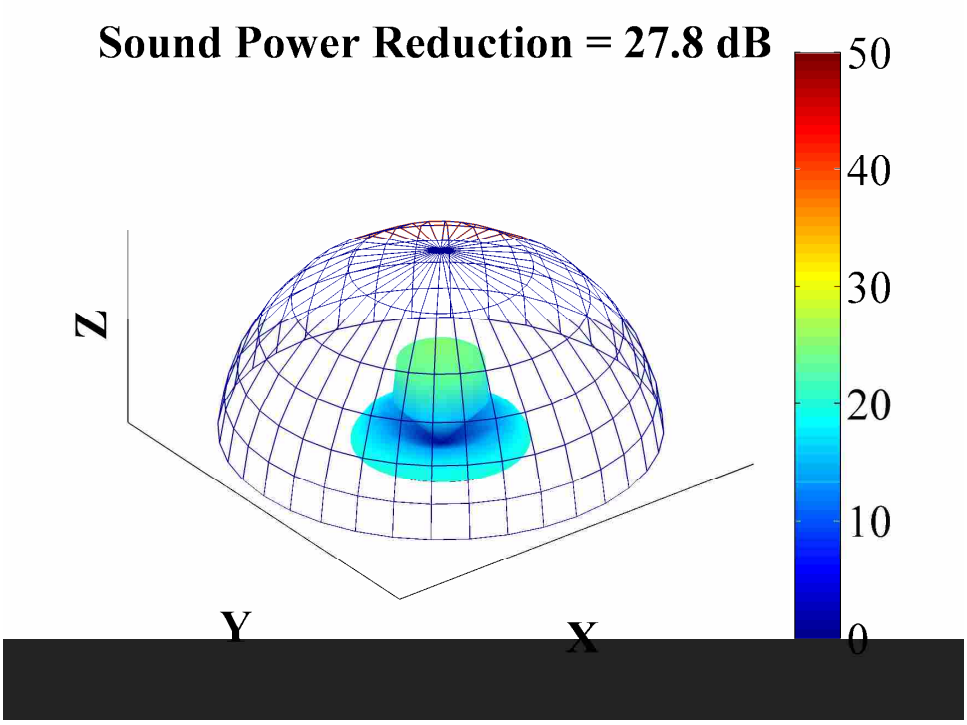

Figure 6-21: The theoretical far field of a single primary point source with (color) and without (wire mesh) control at 659 Hz. Axes units are in dB ref. 20 µPa.

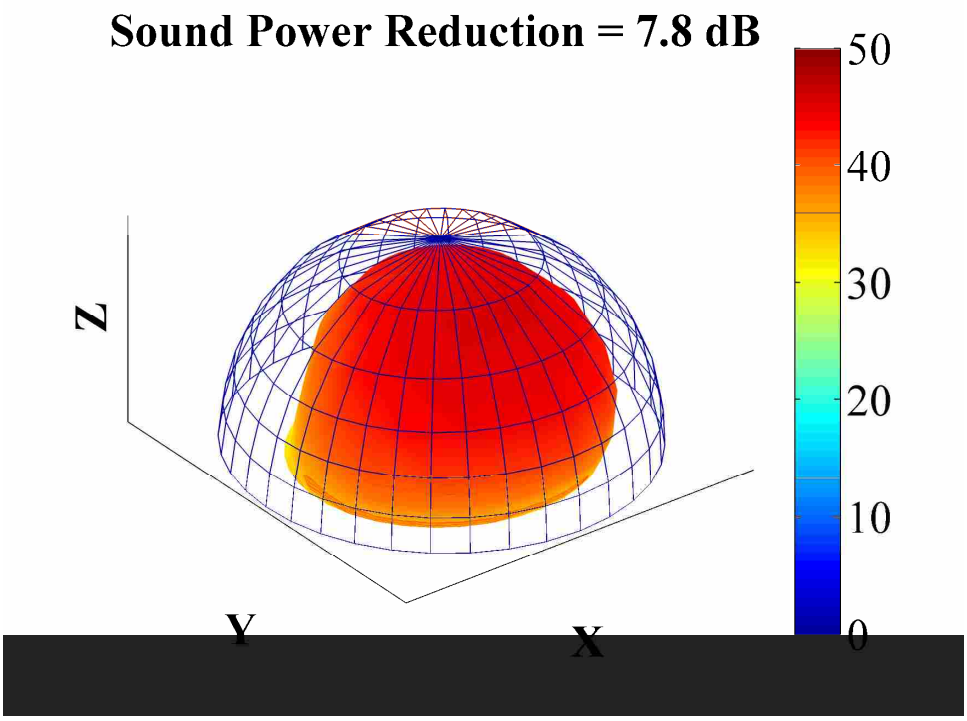

Figure 6-22: The theoretical far field of the ME of an axial fan with (color) and without (wire mesh) control at a BPF of 659 Hz. Axes units are in dB ref. 20 µPa.

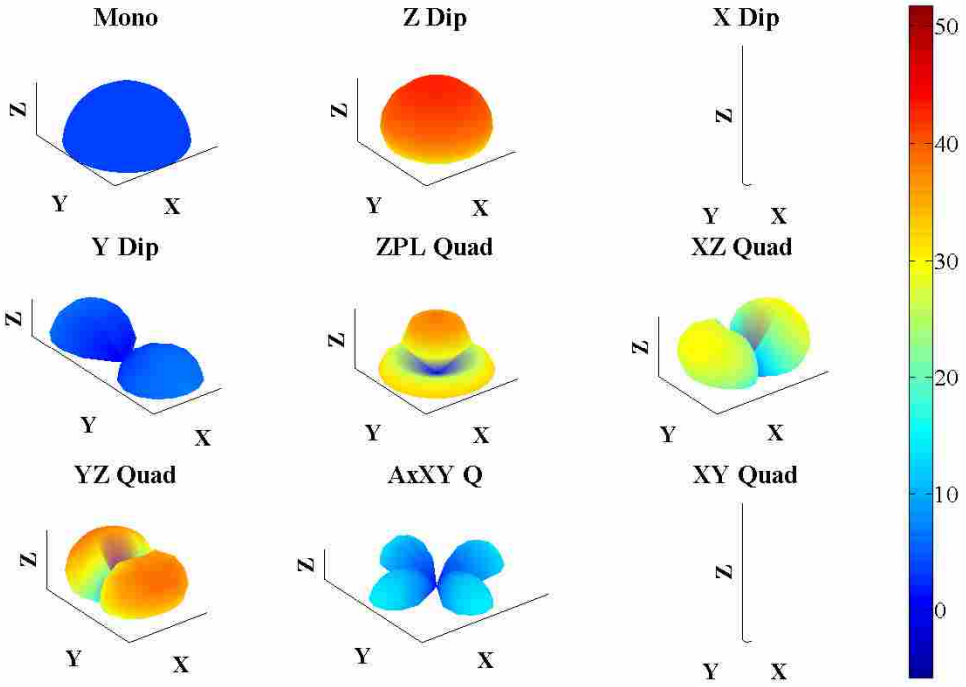

Figure 6-23: The relative contribution of each multipole source in the ME of a theoretically predicted far field at 659 Hz resulting from ANC of the multipolar source. Axes units are in dB ref. 20 µPa.

contribution from each multipole of a second order ME is illustrated in Figure 6-23. In comparison to the relative contributions of the fan without ANC, some of the most dominant multipoles in the expansion, such as the *z*-axis dipole and the pseudo-longitudinal quadrupole, were not theoretically controlled at all. The control sources, in their locations on the *xy*-plane relative to each multipole, theoretically do not acoustically couple to the multipoles whose nodes are located in the plane of the control actuators.

To test this theory further, the theoretical far field pressure was calculated for the same ME model point sources and just two control sources located exactly in the center of the top and bottom lobes, or antinodes, of the *z*-axis dipole. The ME for the theoretical ANC system was calculated and the relative contributions are shown in

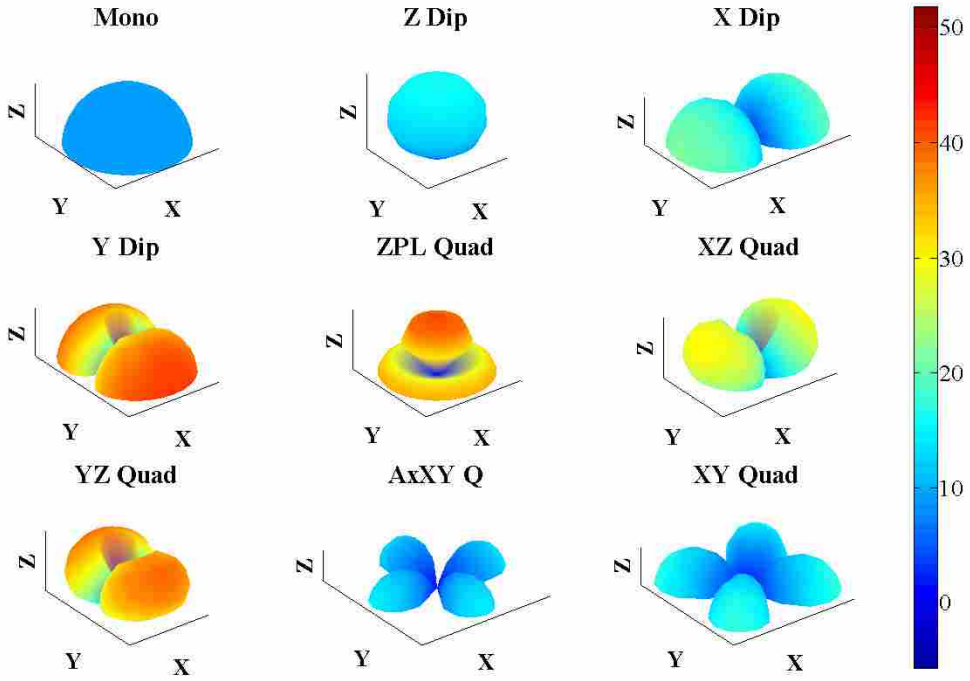

Figure 6-24: The relative contribution of each multipole source in the ME of a theoretically predicted far field at 659 Hz resulting from ANC with two control actuators located on the *z*-axis above and below the origin. Axes units are in dB ref. 20 µPa.

Figure 6-24. As expected, the only multipoles that were reduced were the monopole and *z*-axis dipole.

The principle of acoustic coupling as it applies to multipoles is more clearly illustrated for the case of an acoustic dipole source. Theoretically, if two secondary, or control, sources are placed in near a dipole primary source the prediction of minimum sound power will be zero if the two control sources are placed directly on the pressure null that is created as a result of coupling between the two dipole primary sources. A pressure map of the acoustic near field for this case is shown in Figure 6-25a. A plot of the theoretical minimum sound power for this case over a range of

a)

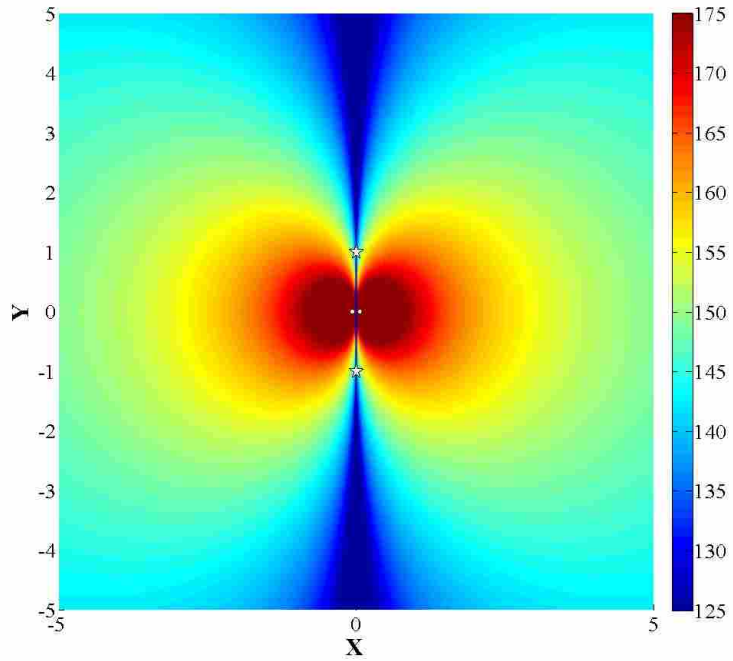

b)

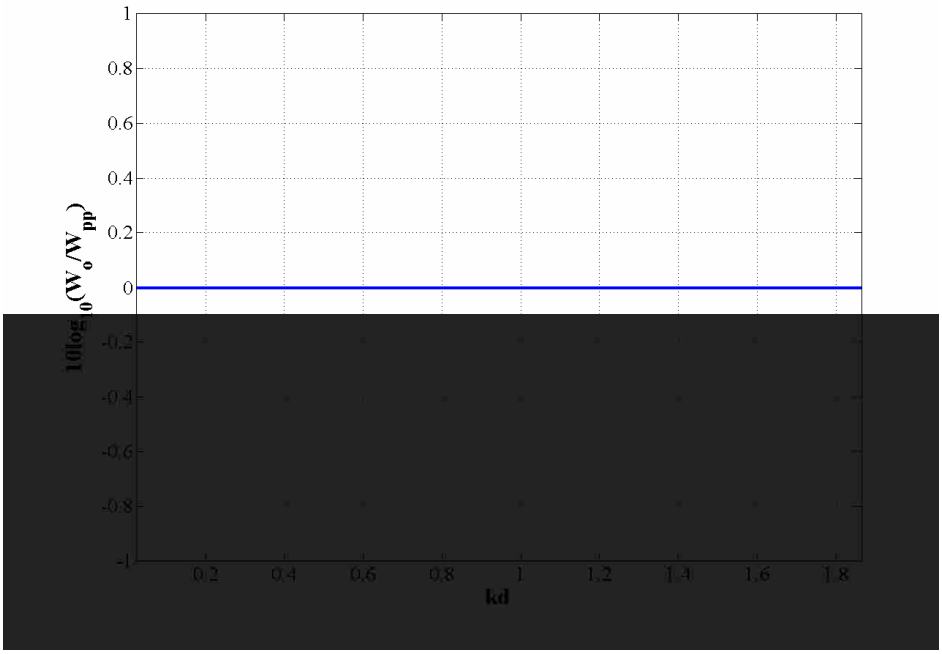

Figure 6-25: Plots of a) the near-field pressure (dB ref. 20μPa) in the plane of ANC for the dipole primary source (1/8″ spacing) at 600 Hz (or *kd* ≈ 0.6) with both control sources located directly on the dipole pressure null and b) the minimum sound power for this case vs. *kd*. Axes units in a) are in inches.

frequencies is shown in Figure 6-25b. Figures 6-26 through 6-30 show the near-field pressure and minimum sound power plots as the two control actuators are rotated out of the dipole pressure null. As shown in the set of figures, the achievable minimum sound power of the ANC configuration increases as the control actuators are moved to locations outside any dipole-induced pressure node.

a)

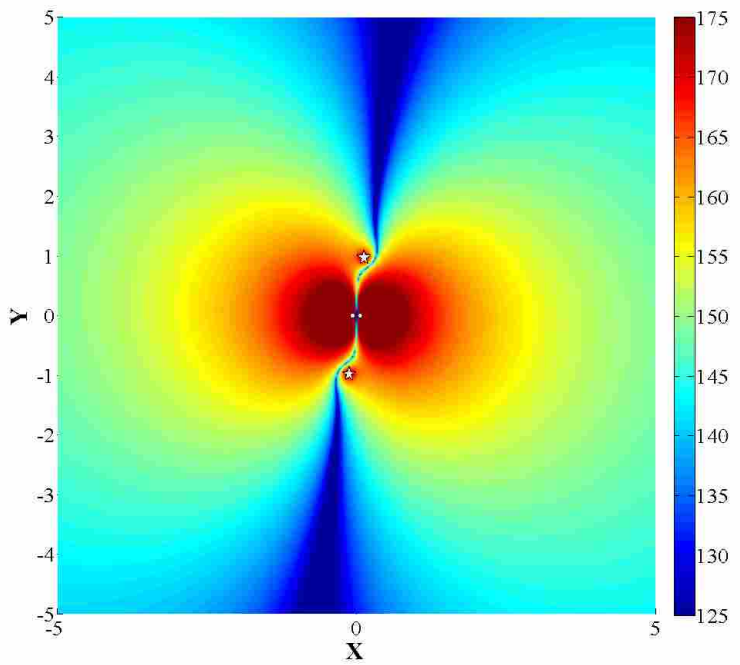

b)

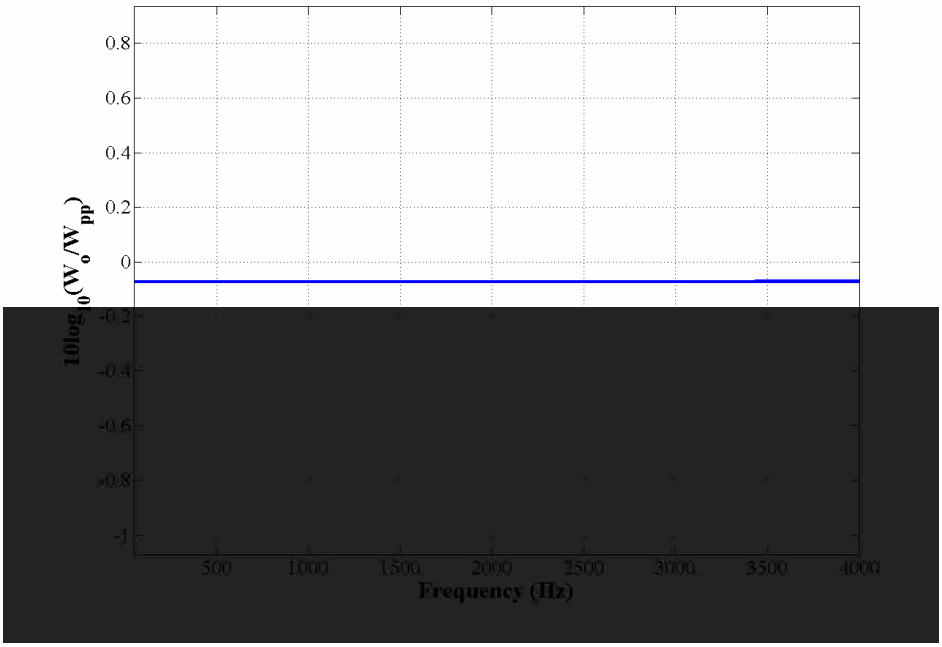

Figure 6-26: Plots of a) the near-field pressure (dB ref. 20μPa) in the plane of ANC for the dipole primary source (1/8″ spacing) at 600 Hz with both control sources rotated 1/8″ off the dipole pressure null and b) the minimum sound power for this case vs. frequency. Axes units in a) are in inches.

a)

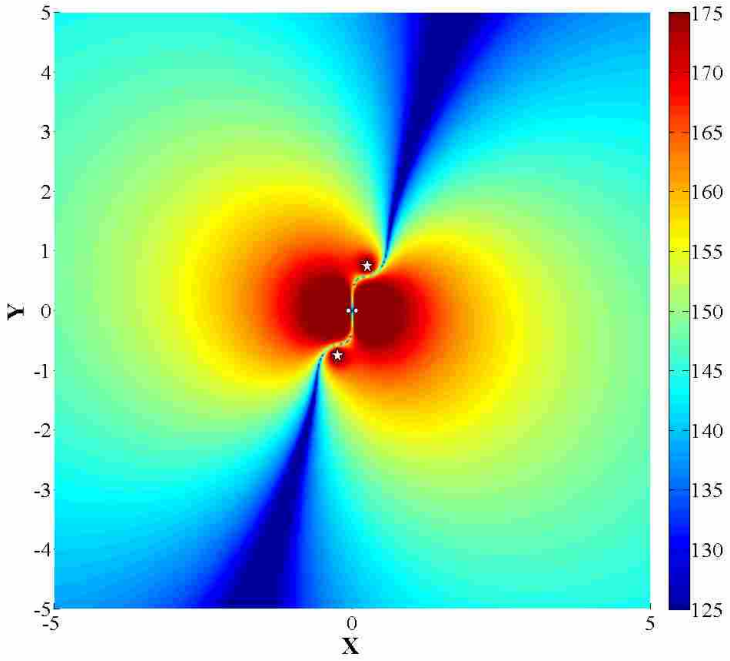

b)

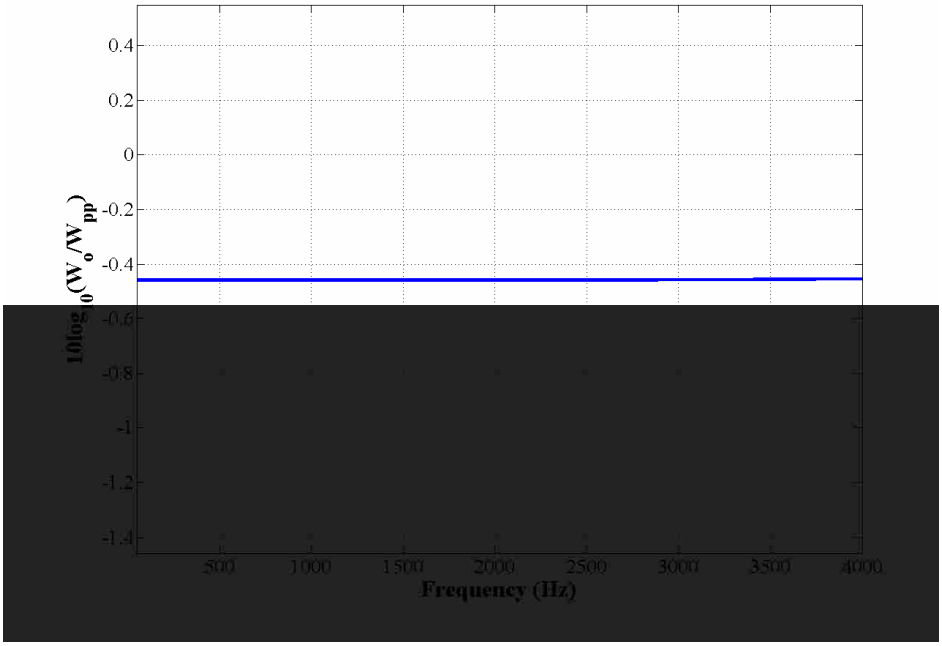

Figure 6-27: Plots of a) the near-field pressure (dB ref. 20μPa) in the plane of ANC for the dipole primary source (1/8″ spacing) at 600 Hz with both control sources rotated 1/4″ off the dipole pressure null and b) the minimum sound power for this case vs. *kd*. Axes units in a) are in inches.

a)

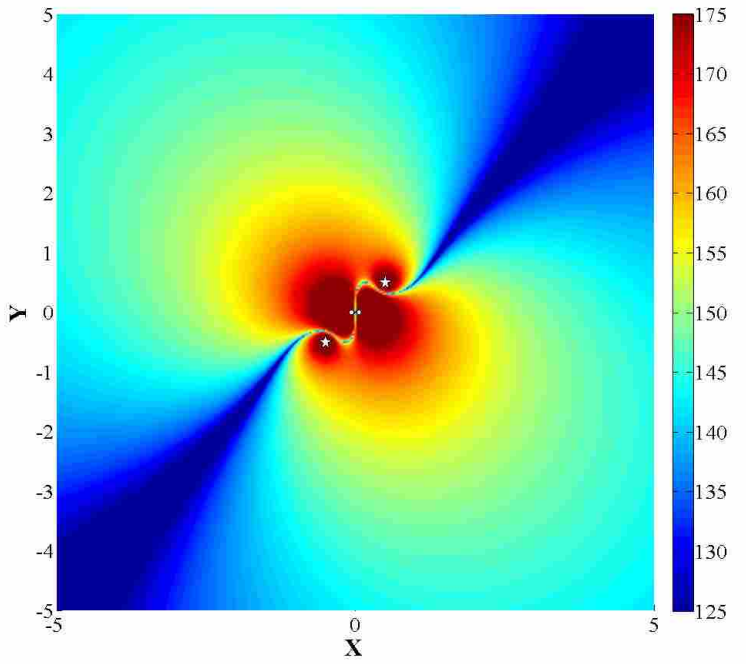

b)

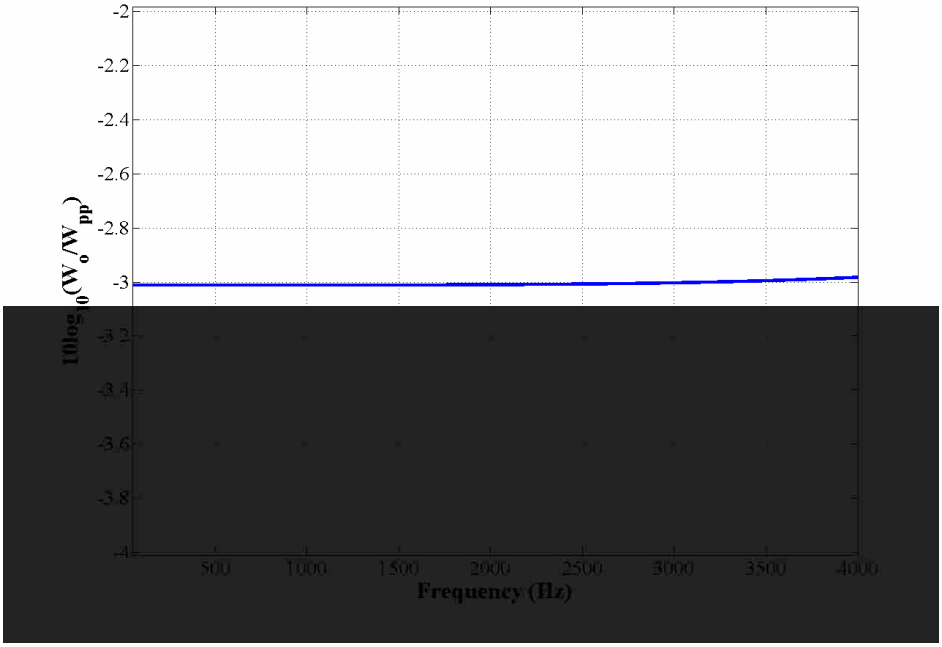

Figure 6-28: Plots of a) the near-field pressure (dB ref. 20μPa) in the plane of ANC for the dipole primary source (1/8″ spacing) at 600 Hz with both control sources rotated 1/2″ off the dipole pressure null and b) the minimum sound power for this case vs. frequency. Axes units in a) are in inches.

a)

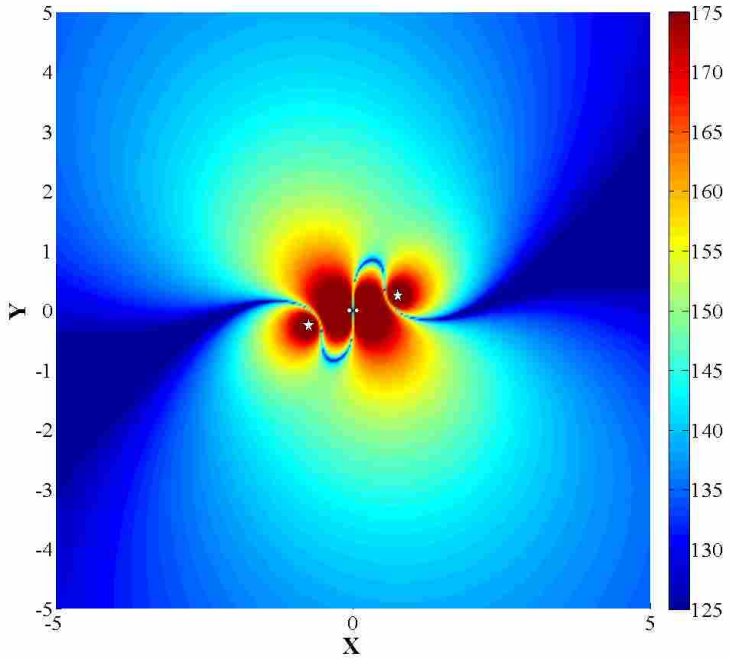

b)

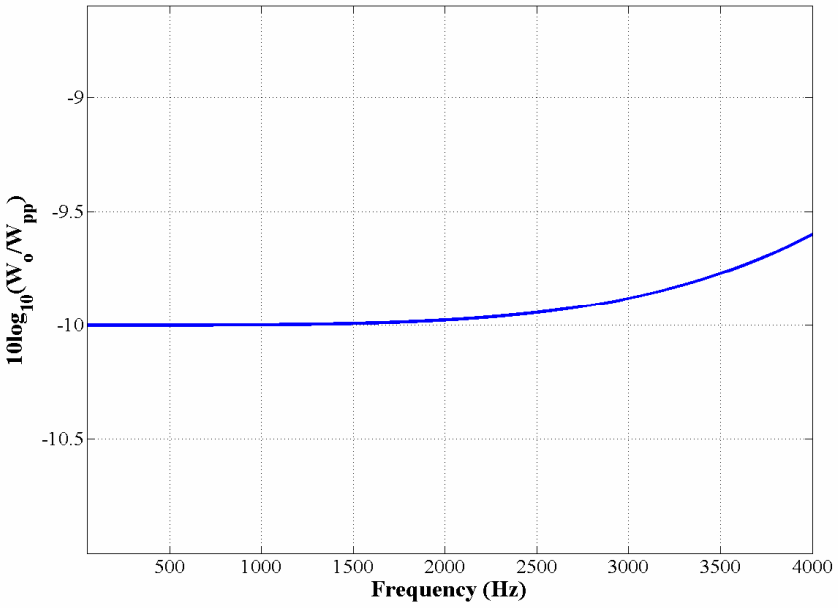

Figure 6-29: Plots of a) the near-field pressure (dB ref. 20μPa) in the plane of ANC for the dipole primary source (1/8″ spacing) at 600 Hz with both control sources located 1/4″ off the dipole anti-node and b) the minimum sound power for this case vs. frequency. Axes units in a) are in inches.

a)

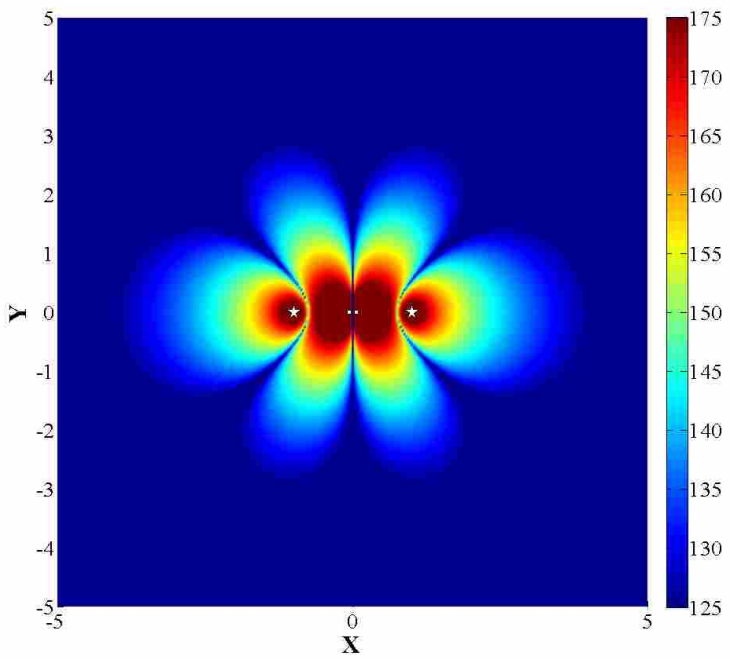

b)

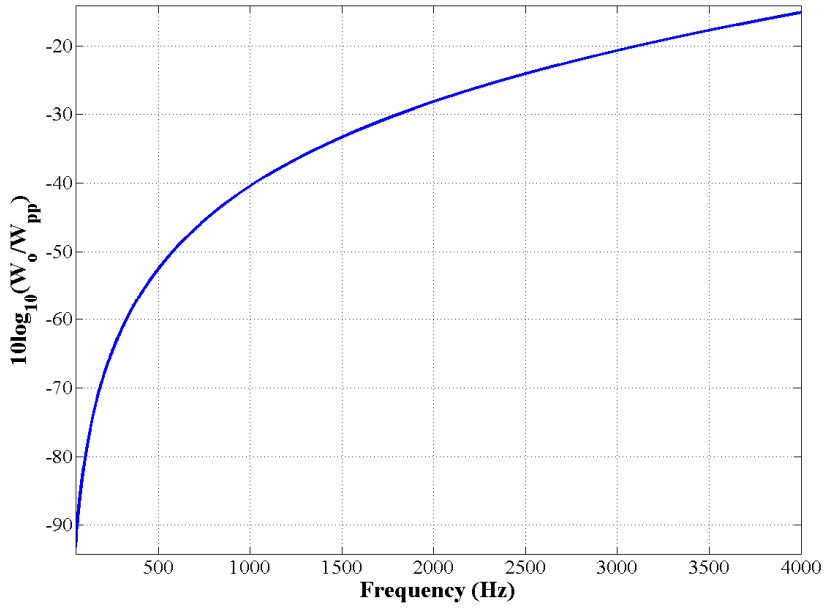

Figure 6-30: Plots of a) the near-field pressure (dB ref. 20μPa) in the plane of ANC for the dipole primary source (1/8″ spacing) at 600 Hz with both control sources located on the dipole anti-node and b) the minimum sound power for this case vs. frequency. Axes units in a) are in inches.

CHAPTER 7

CONCLUSIONS

7.1. NEAR-FIELD ERROR SENSORS

The purpose of near-field ANC measurements was to verify the locations of pressure nulls in the acoustic near field of the primary noise source. These pressure nulls exist based on a condition of theoretically minimized sound power of the primary and secondary sources. In previous experiments, the error sensors have been placed according to the theoretically predicted nulls based on the acoustical coupling between point sources. On the other hand, the process of the ANC system is based on the minimization of the input signals at the error sensor locations. A connection must be made between the ANC process and the acoustic point source coupling.

To explore this connection, three separate cases of ANC were presented for verification: one loudspeaker primary source with two symmetrically located control actuators and two error sensors, the same primary source with four symmetrically located control actuators and four error sensors, and one axial fan primary source with four symmetrically located control actuators and four error sensors. The theoretically predicted pressure nulls for the two-by-two and four-by-four ANC configurations consistently matched the pressure nulls shown in the near-field maps of each ANC measurement.

It is also necessary to understand how such placement affects the global attenuation of the primary source in the far field. Each of the three control cases discussed previously was measured for sound power reductions in the far field as well as two additional error sensor locations. In the first additional location configuration, one of the error sensors was removed from the theoretically predicted pressure null location to a point randomly chosen near the edge of the plate. This had virtually no effect on the sound pressure level reduction achieved by the ANC system. In the second additional configuration, all of the error sensors were placed in locations that were theoretically inappropriate for minimization of sound power. With all the near-field error sensors in non-ideal locations, the mean sound pressure level reduction decreased dramatically in comparison to the ANC system with error sensors in the theoretically predicted pressure nulls. In conclusion, drastic changes in error sensor placement from theoretically appropriate locations to non-ideal locations produce far-field results that are much less desirable.

7.2. MULTIPOLE EXPANSIONS FOR OPTIMIZING SENSOR PLACEMENT

Modeling the axial cooling fan as a multipole noise source did not produce the expected global far-field results. Based on observation, the ME model of fan noise accurately portrays the radiation of a fan in both the acoustic near field and far field. Although the placement of near-field error sensors according to the ME model produced acceptable near-field ANC results, the sound power reduction achieved in the acoustic far field for this case was not optimum. Therefore, it is apparent that there are limitations in the use of the ME model to predict near-field pressure nulls that occur for a theoretical minimization of sound power.

In exploring the limitations of the ME method for error sensor placement, the control sources for the four-by-four ANC system were discovered to be located exactly in the pressure nodes for almost half of the multipoles in the ME of the fan. Theoretically, the control sources in those locations do not acoustically couple to any of those multipoles. Thus, the theoretical prediction did not have the capability of accounting for any near-field pressure nulls that may be created as a result of acoustic coupling with every multipole in the ME for a fan.

7.3. FUTURE WORK

The experimentally achieved sound power reduction for the axial cooling fan was much greater than the theoretical prediction for the ME model. One cause for this arises from the fact the control sources do not acoustically couple with the multipoles that have pressure nodes that occur at the geographic locations of the control sources. The reason why the experimental ANC system is able to achieve results that are so much better than theoretical predictions based on the ME model has not yet been fully determined.

Future exploration of this reason should include an ME of the control actuators in the ANC system. It is important to determine whether or not the control actuators exhibit multipolar characteristics at the BPF and harmonics of the fan. The multipoles that comprise an ME do not give a correct model of the actual coupling between primary and secondary sources. However, it is important to recognize that there are an infinite number of point source configurations within the smallest sphere containing the fan source that could potentially be valid as a representation of fan noise. For example, a more accurate representation of the coupling between primary sources and control actuators in ANC for the fan may be created using equivalent sources located on the smallest sphere

surrounding the multipole primary source. These equivalent sources may represent the acoustic coupling between primary and secondary sources in ANC more accurately because the ME solution for the acoustic pressure inside the smallest sphere surrounding a multipole source is not valid. These issues must be explored further to obtain a more complete understanding of the ME and its application in ANC. There is another possible method for obtaining a model of the fan that acoustically couples to the control sources. If the point sources in the fan noise model are all constrained to remain in the plane of the control sources, a genetic algorithm may be used to determine the complex source strength and locations of a number of point sources in this plane. The genetic algorithm can be programmed to match the measured far-field pressure by minimizing a cost function of the error between the original measurement and the pressure radiated by the equivalent planar point source model at the same far-field location.

APPENDIX

The source strength of individual multipole sources in an ME may be calculated by manipulating the solution to the Helmholtz equation in Eq. 4-6 for a finite order, *N*. The highest order used for this thesis was $N = 2$. For a second order ME, Eq. 4-6 must be used to solve for nine separate multipole source strengths. A general from of this solution is shown in the following equation,

$$\hat{p}(r,\theta,\varphi) = \hat{A}_{mn} \mathrm{Y}_n^m(\theta,\varphi) h_n^{(1)}(kr) \tag{A-1}$$

where $\hat{p}(r,\theta,\varphi)$ is the complex acoustics pressure, $\hat{A}_{mn}$ is the m^{th} and n^{th} spherical harmonic coefficient, $\mathrm{Y}_n^m(\theta,\varphi)$ is the m^{th} and n^{th} spherical harmonic, and $h_n^{(1)}(kr)$ is the spherical Hankel function for the n^{th} order outgoing spherical waves. It is important to note that this solution is only valid on or outside the smallest sphere containing the sound source. The directivity pattern for the multipole sources in a second order ME is shown in Figure 4-1. Section 4.3.1 provides an example of the method for calculated the source strength of the monopole source that results from a second order ME. The source strength of each dipole and quadrupole source in a second order ME is solved in the following paragraphs. An $e^{-i\omega t}$ time dependence is assumed in each solution.

The analytical expression for the $\hat{A}_{01}$ dipole, oriented on the *z*-axis, is

$$\hat{p}_{dz}(r,\theta,\varphi) = \frac{\rho_0 c k^3 \varepsilon}{2\pi} \hat{q}_{dz} \cos\theta \left[-e^{ikr} \left(\frac{1}{kr} + \frac{i}{(kr)^2} \right) \right]. \tag{A-2}$$

The variable ε is the distance from the origin to each point source and the other variables have been defined in the body of this thesis. The equivalent expression for the pressure of an acoustic dipole oriented on the z-axis is

$$\hat{p}_{dz}(r,\theta,\varphi) = \hat{A}_{01} \mathrm{Y}_1^0(\cos\theta) h_1^{(1)}(kr), \tag{A-3}$$

$$\mathrm{Y}_1^0(\cos\theta) = \cos\theta, \tag{A-4}$$

$$h_1^{(1)}(kr) = -e^{ikr} \left(\frac{1}{kr} + \frac{i}{(kr)^2} \right). \tag{A-5}$$

The source strength of each point dipole source may be calculated using the equivalent expressions in Eq. A-3 and Eq. A-2:

$$\hat{q}_{dz} = \frac{2\pi}{\rho_0 c k^3 \varepsilon} \hat{A}_{01}. \tag{A-6}$$

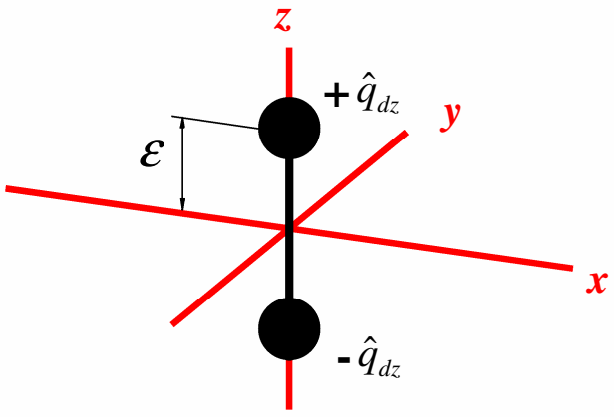

Figure A-1: The orientation and polarity of the z-axis dipole, derived from the spherical harmonic coefficient $\hat{A}_{01}$, in a second order ME.

Figure A-1 illustrates the orientation and polarity of the *z*-axis dipole as well as the separation distance between the dipole point sources.

The analytical expression for the $\hat{A}_{11}$ dipole, oriented on the *x*-axis, is

$$\hat{p}_{dx}(r,\theta,\varphi) = -\frac{\rho_0 ck^3 \varepsilon}{2\pi}\hat{q}_{dx}\sin\theta\cos\varphi\left[-e^{ikr}\left(\frac{1}{kr}+\frac{i}{(kr)^2}\right)\right]. \tag{A-7}$$

The equivalent expression for the pressure of an acoustic dipole oriented on the *x*-axis is

$$\hat{p}_{dx}(r,\theta,\varphi) = -\hat{A}_{11}\mathrm{Y}_1^1(\cos\theta)h_1^{(1)}(kr), \tag{A-8}$$

$$\mathrm{Y}_1^1(\cos\theta) = \sin\theta\cos\varphi. \tag{A-9}$$

The 1st order spherical Hankel function for outgoing waves is defined in Eq. A-5. The source strength of each point dipole source may be calculated using the equivalent expressions in Eq. A-8 and Eq. A-7:

$$\hat{q}_{dx} = \frac{2\pi}{\rho_0 ck^3 \varepsilon}\hat{A}_{11}. \tag{A-10}$$

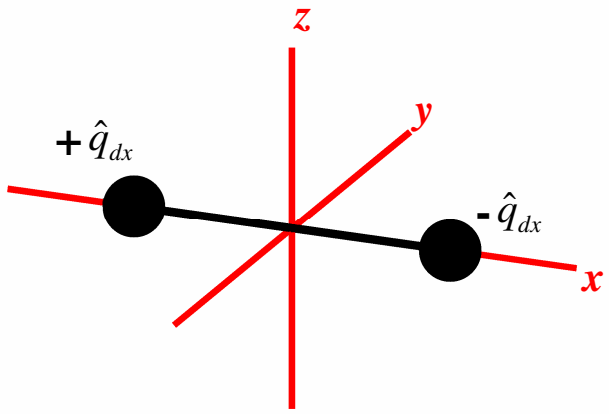

Figure A-2: The orientation and polarity of the *x*-axis dipole, derived from the spherical harmonic coefficient $\hat{A}_{11}$, in a second order ME.

Figure A-2 illustrates the orientation and polarity of the *x*-axis dipole. The separation distance between point sources is similar to that illustrated in Figure A-1, equal to the distance from the origin to either of the point sources.

The analytical expression for the $\hat{B}_{11}$ dipole, oriented on the *y*-axis, is

$$\hat{p}_{dy}(r,\theta,\varphi) = -\frac{\rho_0 ck^3 \varepsilon}{2\pi}\hat{q}_{dy}\sin\theta\sin\varphi\left[-e^{ikr}\left(\frac{1}{kr}+\frac{i}{(kr)^2}\right)\right]. \tag{A-11}$$

The equivalent expression for the pressure of an acoustic dipole oriented on the *y*-axis is

$$\hat{p}_{dy}(r,\theta,\varphi) = -\hat{B}_{11}\mathrm{Y}_1^{-1}(\cos\theta)h_1^{(1)}(kr), \tag{A-12}$$

$$\mathrm{Y}_1^{-1}(\cos\theta) = \sin\theta\sin\varphi. \tag{A-13}$$

The 1st order spherical Hankel function for outgoing waves is defined in Eq. A-5. The source strength of each point dipole source is calculated as

$$\hat{q}_{dy} = \frac{2\pi}{\rho_0 ck^3\varepsilon}\hat{B}_{11}. \tag{A-14}$$

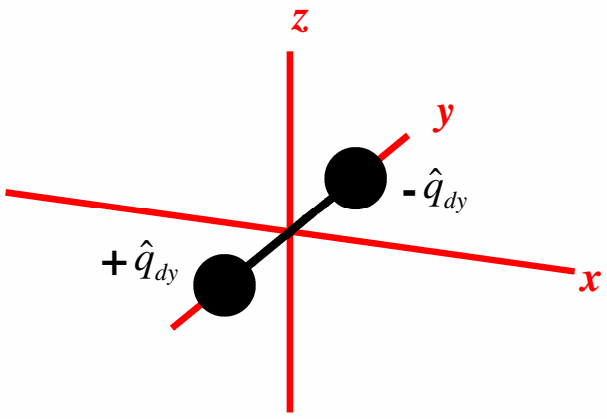

Figure A-3: The orientation and polarity of the *y*-axis dipole, derived from the spherical harmonic coefficient $\hat{B}_{11}$, in a second order ME.

Figure A-3 illustrates the orientation and polarity of the *y*-axis dipole. The separation distance between point sources is similar to that illustrated in Figure A-1, equal to the distance from the origin to either of the point sources.

The first quadrupole in a second order ME has been defined as a pseudo-longitudinal quadrupole oriented on the *z*-axis. The expression for an acoustic longitudinal quadrupole oriented on the *z*-axis is

$$\hat{p}_{zlq}(r,\theta,\varphi) = \frac{i\rho_0 ck^3\varepsilon^2}{4\pi r}\hat{q}_{zlq}\left[\cos^2\theta\left(1+\frac{3i}{kr}-\frac{3}{(kr)^2}\right)-\frac{i}{kr}+\frac{1}{(kr)^2}\right]e^{ikr}. \qquad \text{(A-15)}$$

An equivalent expression for this longitudinal quadrupole cannot be found using solely spherical harmonic coefficients, spherical Hankel functions, and spherical harmonics. A monopole term may be added to the expression in Eq. A-15 that yields an expression which is equivalent to a spherical harmonic. With this extra point monopole $\hat{q}_{mplq}$, located at the origin, the expression for the pseudo-longitudinal quadrupole oriented on the z-axis becomes

$$\hat{p}_{zplq}(r,\theta,\varphi) = \frac{i\rho_0 ck^3\varepsilon^2}{4\pi r}\hat{q}_{zplq}\left[\begin{array}{l}\cos^2\theta\left(1+\dfrac{3i}{kr}-\dfrac{3}{(kr)^2}\right)\\ -\dfrac{i}{kr}+\dfrac{1}{(kr)^2}\end{array}\right]e^{ikr} - \qquad \text{(A-16)}$$

$$\frac{i\rho_0 ck}{4\pi r}\hat{q}_{mplq}e^{ikr}.$$

With the addition of the point monopole centered at the origin, the expression in Eq. A-16 may be manipulated to produce an expression that resembles a spherical harmonic-

type equation. To produce equivalent mathematical expressions in terms of spherical harmonics the extra point monopole source, $\hat{q}_{mplq}$, must be

$$\hat{q}_{mplq} = \frac{(kd)^2}{3}\hat{q}_{zplq}. \tag{A-17}$$

When the expression for $\hat{q}_{mplq}$ is substituted into Eq. A-16 and the appropriate mathematical terms are combined, the equation for the $\hat{A}_{02}$ pseudo-longitudinal quadrupole becomes

$$\hat{p}_{zplq}(r,\theta,\varphi) = \frac{\rho_0 c k^4 \varepsilon^2}{4\pi}\hat{q}_{zplq}\left(\cos^2\theta - 1/3\right)\frac{ie^{ikr}}{kr}\left[1 + \frac{3i}{kr} - \frac{3}{(kr)^2}\right]. \tag{A-18}$$

The equivalent expression for the pressure of a pseudo-longitudinal quadrupole oriented on the *z*-axis, in terms of spherical harmonics and spherical Hankel functions, is

$$\hat{p}_{zplq}(r,\theta,\varphi) = \hat{A}_{02}\mathrm{Y}_2^0(\cos\theta)h_2^{(1)}(kr), \tag{A-19}$$

$$\mathrm{Y}_2^0(\cos\theta) = 3/2\left(\cos^2\theta - 1/3\right), \tag{A-20}$$

$$h_2^{(1)}(kr) = \frac{ie^{ikr}}{kr}\left(1 + \frac{3i}{kr} - \frac{3}{(kr)^2}\right). \tag{A-21}$$

The source strength of the pseudo-longitudinal quadrupole is then calculated as

$$\hat{q}_{zplq} = \frac{6\pi}{\rho_0 c k^4 \varepsilon^2}\hat{A}_{02}. \tag{A-22}$$

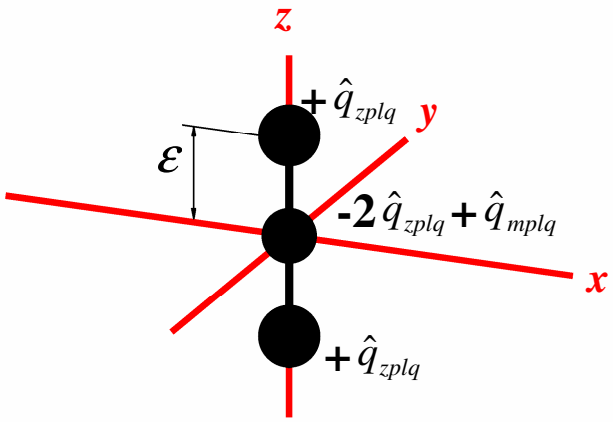

Figure A-4: The orientation and polarity of the pseudo-longitudinal quadrupole, derived from the spherical harmonic coefficient $\hat{A}_{02}$, in a second order ME.

Figure A-4 illustrates the orientation and polarity of the pseudo-longitudinal quadrupole. The distance, ε, between point sources is shown in the figure.

The multipole that corresponds to the $\hat{A}_{12}$ spherical harmonic is a lateral quadrupole located in the *xz*-plane and centered about the origin. The analytical expression for this quadrupole is

$$\hat{p}_{xzq}(r,\theta,\varphi) = -\frac{\rho_0 ck^4\varepsilon^2}{2\pi r}\hat{q}_{xzq}\sin 2\theta\cos\varphi\frac{ie^{ikr}}{kr}\left[1+\frac{3i}{kr}-\frac{3}{(kr)^2}\right]. \qquad \text{(A-23)}$$

The equivalent expression for the pressure of this lateral quadrupole, in terms of spherical harmonics and spherical Hankel functions, is

$$\hat{p}_{xzq}(r,\theta,\varphi) = -\hat{A}_{12}\mathrm{Y}_2^1(\cos\theta)h_2^{(1)}(kr), \qquad \text{(A-24)}$$

$$\mathrm{Y}_2^1(\cos\theta) = \sqrt{3/2}\sin 2\theta\cos\varphi, \qquad \text{(A-25)}$$

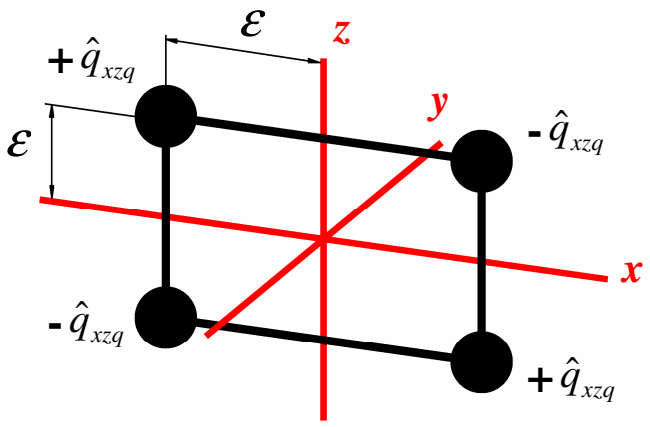

Figure A-5: The orientation and polarity of the *xz*-plane lateral quadrupole, derived from the spherical harmonic coefficient $\hat{A}_{12}$, in a second order ME.

The source strength of the *xz*-plane lateral quadrupole is then calculated as

$$\hat{q}_{xzq} = \frac{3\pi}{\rho_0 c k^4 \varepsilon^2} \hat{A}_{12} . \qquad \text{(A-26)}$$

Figure A-5 illustrates the orientation and polarity of the *xz*-plane quadrupole. The distance value, ε, is shown in the figure.

The $\hat{B}_{12}$ multipole is a lateral quadrupole located in the *yz*-plane and centered about the origin. The analytical expression for this quadrupole is

$$\hat{p}_{yzq}(r,\theta,\varphi) = -\frac{\rho_0 c k^4 \varepsilon^2}{2\pi r} \hat{q}_{yzq} \sin 2\theta \sin\varphi \frac{ie^{ikr}}{kr} \left[1 + \frac{3i}{kr} - \frac{3}{(kr)^2} \right]. \qquad \text{(A-27)}$$

The equivalent expression for the pressure of this lateral quadrupole, in terms of spherical harmonics and spherical Hankel functions, is

$$\hat{p}_{yzq}(r,\theta,\varphi) = -\hat{B}_{12}\mathrm{Y}_2^{-1}(\cos\theta)h_2^{(1)}(kr), \tag{A-28}$$

$$\mathrm{Y}_2^{-1}(\cos\theta) = \sqrt{3}/2 \sin 2\theta \sin\varphi, \tag{A-29}$$

The source strength of the *xz*-plane lateral quadrupole is then calculated as

$$\hat{q}_{yzq} = \frac{3\pi}{\rho_0 c k^4 \varepsilon^2}\hat{B}_{12}. \tag{A-30}$$

Figure A-6 illustrates the orientation and polarity of the *yz*-plane quadrupole. The distance value, ε, follows the same basic pattern as shown in Figure A-5.

The $\hat{A}_{22}$ multipole is a lateral quadrupole similar to the two previously defined; however, it is located on the *xy*-axis. The distance between each point source is, therefore, multiplied by a factor of $\sqrt{2}/2$ in comparison to the two previously defined lateral quadrupoles. This quadrupole has been termed the axial *xy*-plane lateral

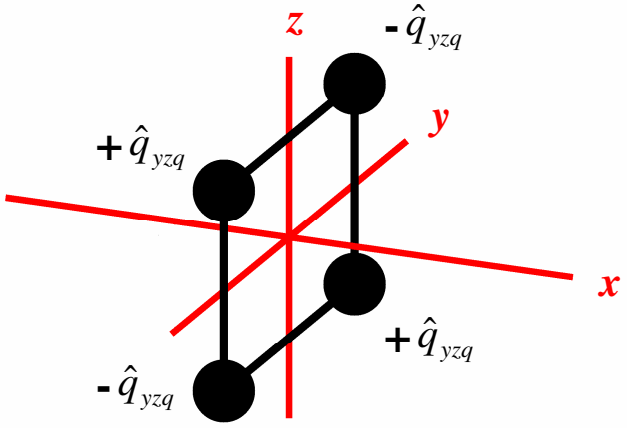

Figure A-6: The orientation and polarity of the *yz*-plane lateral quadrupole, derived from the spherical harmonic coefficient $\hat{B}_{12}$, in a second order ME.

quadrupole. The analytical expression for this quadrupole is

$$\hat{p}_{Axq}(r,\theta,\varphi) = \frac{\rho_0 c k^4 \varepsilon^2}{4\pi r}\hat{q}_{Axq}(1-\cos 2\theta)\sin 2\varphi \frac{ie^{ikr}}{kr}\left[1+\frac{3i}{kr}-\frac{3}{(kr)^2}\right]. \qquad \text{(A-31)}$$

The equivalent expression for the pressure of this quadrupole, in terms of spherical harmonics and spherical Hankel functions, is

$$\hat{p}_{Axq}(r,\theta,\varphi) = \hat{A}_{22}\mathrm{Y}_2^2(\cos\theta)h_2^{(1)}(kr), \qquad \text{(A-32)}$$

$$\mathrm{Y}_2^2(\cos\theta) = 3/2\,(1-\cos 2\theta)\cos 2\varphi. \qquad \text{(A-33)}$$

The source strength of the axial *xy*-plane lateral quadrupole is then calculated as

$$\hat{q}_{Axq} = \frac{6\pi}{\rho_0 c k^4 \varepsilon^2}\hat{A}_{22}. \qquad \text{(A-34)}$$

Figure A-7 illustrates the orientation and polarity of the axial *xy*-plane lateral quadrupole. The distance value, ε, for this multipole is shown in the figure. The $\hat{B}_{22}$ multipole is a lateral quadrupole located in the *xy*-plane and centered about the origin. The analytical

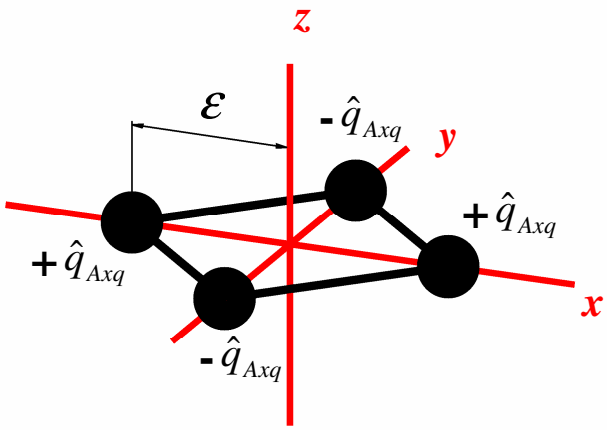

Figure A-7: The orientation and polarity of the axial *xy*-plane lateral quadrupole, derived from the spherical harmonic coefficient $\hat{A}_{22}$, in a second order ME.

expression for this quadrupole is

$$\hat{p}_{xyq}(r,\theta,\varphi) = \frac{\rho_0 c k^4 \varepsilon^2}{4\pi r} \hat{q}_{xyq} (1-\cos 2\theta)\sin 2\varphi \frac{ie^{ikr}}{kr}\left[1+\frac{3i}{kr}-\frac{3}{(kr)^2}\right]. \qquad \text{(A-27)}$$

The equivalent expression for the pressure of this lateral quadrupole, in terms of spherical harmonics and spherical Hankel functions, is

$$\hat{p}_{xyq}(r,\theta,\varphi) = \hat{B}_{22} \mathrm{Y}_2^{-2}(\cos\theta) h_2^{(1)}(kr), \qquad \text{(A-28)}$$

$$\mathrm{Y}_2^{-2}(\cos\theta) = \tfrac{3}{2}(1-\cos 2\theta)\sin 2\varphi, \qquad \text{(A-29)}$$

The source strength of the *xy*-plane lateral quadrupole is then calculated as

$$\hat{q}_{xyq} = \frac{6\pi}{\rho_0 c k^4 \varepsilon^2} \hat{B}_{22}. \qquad \text{(A-30)}$$

Figure A-8 illustrates the orientation and polarity of the *xy*-plane quadrupole. The distance value, ε, follows the same basic pattern as shown in Figure A-5.

Although the polarity of each multipole, when switched, will produce the same directivity, combination of these nine multipoles, each with their specific polarities, was defined to produce the least amount of error between the ME reconstruction and a theoretical multipolar input pressure field.

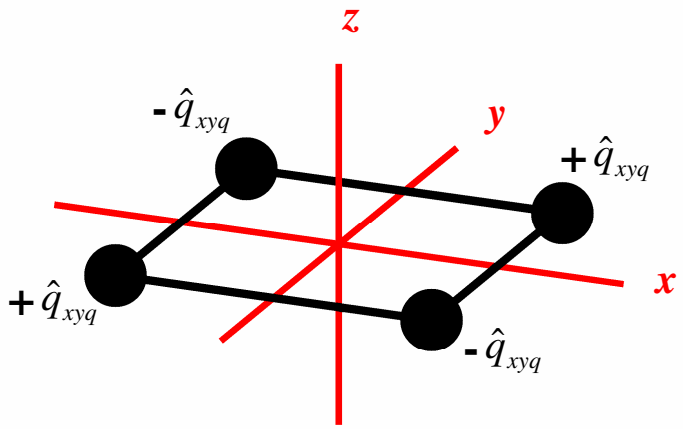

Figure A-8: The orientation and polarity of the *xy*-plane lateral quadrupole, derived from the spherical harmonic coefficient $\hat{B}_{22}$, in a second order ME.

REFERENCES

1. Dan Rutter, "iCute 0408 SL Computer Case," http://www.dansdata.com/images/ic0408sl/inside720.jpg (Accessed September 2, 2007).
2. William J. Strong and George R. Plitnik, *Music Speech Audio, 2nd Ed.*, (BYU Academic Publishing, Provo, Utah, 2005).
3. Cyril M. Harris, Editor in Chief, *Handbook of Acoustical Measurements and Noise Control, 3rd Ed.*, (Acoustical Society of America, Woodbury, New York, 1998).
4. J. P. Bridelance, "Aeroacoustic study of axial fans with small diameter, analysis and suppression of instability noise," *Proceedings of Inter-Noise '86—Cambridge, USA*, 141–146 (1986).
5. Lutz Kaiser and Kurt Wöhrle, "Variable speed blowers—a solution to control the noise of computers," *Proceedings of Inter-Noise '89—Newport Beach, CA, USA*, 157–162 (1989).
6. Cyril M. Harris, Editor in Chief, George C. Maling, Jr. and Andrew L. Boggess, Jr., *Handbook of Acoustical Measurements and Noise Control, 3rd Ed. (Chapter 44—Ventilating Systems for Small Equipment)*, (Acoustical Society of America, Woodbury, New York, 1998).

7. T. Nakahama and F. Ishibashi, "Analysis and visualization of flow around blades of axial fans for large capacity open-type motors," *Proceedings of IEE—Electr. Power Appl.* **151** (1), 70–75 (2004).

8. James M. Fitzgerald and G. C. Lauchle, "Reduction of discrete frequency noise in small, subsonic axial-flow fans," *Journal of the Acoustical Society of America* **76** (1), 158–166 (1984).

9. Cyril M. Harris, Editor in Chief, J. Barrie Graham and Robert M. Hoover, *Handbook of Acoustical Measurements and Noise Control, 3rd Ed. (Chapter 41—Fan Noise)*, (Acoustical Society of America, Woodbury, New York, 1998).

10. Mei Q. Wu, "Active cancellation of small cooling fan noise from office equipment," *Proceedings of Inter-Noise '95—Newport Beach, CA, USA*, 525–528 (1995).

11. Herbach and Rademan Company, Inc., "200 CFM, 110–120 VAC Axial Fan," http://www.herbach.com/Merchant2/graphics/00000001/fan4710.jpg (Accessed September 2, 2007).

12. Allan D. Pierce, *Acoustics: An Introduction to its Physical Principles and Applications* (Acoustical Society of America, Melville, NY, 1989).

13. Heinrich Kuttruff, *Room Acoustics, 4th Ed.* (Taylor and Francis, London, England, 2000).

14. Leo L. Beranek, *Acoustics* (Acoustical Society of America, Woodbury, NY, 1996)

15. Gerald C. Lauchle, John R. MacGillivray, and David C. Swanson, "Active control of axial-flow fan noise," *Journal of the Acoustical Society of America* **101** (1), 341–349 (1997).

16. P.A. Nelson and S.J. Elliott, *Active Control of Sound* (Academic Press, Inc., San Diego, CA, 1992).

17. D.A. Quinlan, "Application of active control to axial flow fans," *Noise Control Engineering Journal* **39** (3), 95–101 (1992).

18. Philip M. Morse and K. Uno Ingard, *Theoretical Acoustics* (Princeton University Press, Princeton, NJ, 1968).

19. Scott D. Sommerfeldt and Peter J. Nashif, "An adaptive filtered-x algorithm for energy-based active control," *Journal of the Acoustical Society of America* **96** (1), 300–306 (1994).

20. Kent L. Gee and Scott D. Sommerfeldt, "A compact active control implementation for axial cooling fan noise," *Noise Control Engineering Journal* **51** (6), 325–334 (2003).

21. Kent L. Gee and Scott D. Sommerfeldt, "Application of theoretical modeling to multichannel active control of cooling fan noise," *Journal of the Acoustical Society of America* **115** (1), 228–236 (2004).

22. Daniel Quinlan, "Active control of noise radiated from small axial flow fans," *Proceedings of Inter-Noise '89—Newport Beach, CA, USA*, 479–482 (1989).

23. T. Martin and A. Roure, "Optimization of an active noise control system using spherical harmonics expansion of the primary field," *Journal of Sound and Vibration* **201** (5), 577–593 (1997).

24. A.J. Kempton, "The ambiguity of acoustic sources—a possibility for active control?," *Journal of Sound and Vibration* **48** (4), 475–483 (1976).

25. A. Berry, X. Qiu, and C.H. Hansen, "Near-field sensing strategies for the active control of the sound radiated from a plate," *Journal of the Acoustical Society of America* **106** (6), 3394–3406 (1999).

26. X. Qiu, C.H. Hansen, and X. Li, "A comparison of near-field acoustic error sensing strategies for the active control of harmonic free field sound radiation," *Journal of Sound and Vibration*, **215** (1), 81–103 (1998).

27. Anthony Gérard, Alain Berry, and Patrice Masson, "Control of tonal noise from subsonic axial fan. Part 1: reconstruction of aeroacoustic sources from far-field sound pressure," *Journal of Sound and Vibration* **288** (4), 1049–1075 (2005).

28. Anthony Gérard, Alain Berry, and Patrice Masson, "Control of tonal noise from subsonic axial fan. Part 2: active control simulations and experiments in free field," *Journal of Sound and Vibration* **288** (4), 1077–1104 (2005).

29. Duck-Joo Lee, Wan-Ho Jeon, and Ki-Hoon Chung, "Development and application of fan noise prediction method to axial and centrifugal fan," *Proceedings of ASME '02—Fluids Engineering Division Summer Meeting, Montreal, Quebec, Canada*, 987–992 (2002).

30. Michel Roger, Stephane Moreau, and Alain Guedel, "Broadband fan noise prediction using single air-foil theory," *Noise Control Engineering Journal* **54** (1), 5–14 (2006).

31. W. Neise, "Review of fan noise generation mechanisms and control methods," *Proceedings of Fan Noise and International INCE Symposium*, 45–56 (1992).

32. L. Mongeau and D.A. Quinlan, "An experimental study of broadband noise sources in small axial cooling fans," *Proceedings of Fan Noise '03*, 119–140 (2003).

33. M.J. Lighthill, “The Bakerian Lecture, 1961. Sound Generated Aerodynamically,” *Proceedings of the Royal Society of London. Series A, Mathematical and Physical Sciences* **267** (1329), 147–182 (1962).

34. Lixi Huang and Jian Wang, “Acoustic analysis of a computer cooling fan,” *The Journal of the Acoustical Society of America* **118** (4), 2190–2200 (2005).

35. George C. Maling, Jr., “Historical developments in the control of noise generated by small air-moving devices,” *Noise Control Engineering Journal* **42** (5), 159–169 (1994).

36. Jian Wang and Lixi Huang, “Quantification and control of noise sources in a small axial-flow fan,” *Noise Control Engineering Journal* **54** (1), 27–32 (2006).

37. Serguei Timouchev, Jean Tourret, Goran Pavic, and Andrey Aksenov, “Numerical 2-D and 3-D methods for computation of internal unsteady pressure field and near-field noise of fans,” *Noise Control Engineering Journal* **54** (1), 15–20 (2006).

38. S. F. Wu and S. G. Su, “Modelling of the noise spectra of axial flow fans in a free field,” *Journal of Sound and Vibration* **200** (4), 379–399 (1997).

39. J. Xie, R. S. Amano, and E. K. Lee, “An evaluation of simulated flow and experimental study through an axial fan,” *Proceedings of DETC ’03—ASME 2003 Design Engineering Technical Conference and Computers and Information in Engineering Conference*, 747–755 (2003).

40. A. Guedel and N. Yazigi, “Influence of blade sweep on the noise of a low-speed tubeaxial fan,” *Proceedings of Fan Noise and International INCE Symposium*, 167–178 (1992).

41. Donald B. Hanson, "Unified analysis of fan stator noise," *The Journal of the Acoustical Society of America* **54** (6), 1571–1591 (1973).

42. Jedryszek Jan, "Mathematical model of acoustic sources for rotor-stator interaction in axial flow fans," *Proceedings of Inter-Noise '79*, 95–98 (1979).

43. I. J. Sharland, "Sources of noise in axial flow fans," *Journal of Sound and Vibration* **1** (3), 302–322 (1964).

44. George B. Arfken and Hans J. Weber, *Mathematical Methods for Physicists* (Academic Press, San Diego, California, 1995).

45. P.A. Nelson and S.H. Yoon, "Estimation of acoustic source strength by inverse methods: part I, conditioning of the inverse problem," *Journal of Sound and Vibration* **233** (4), 643–668 (2000).

46. S.H. Yoon and P.A. Nelson, "Estimation of acoustic source strength by inverse methods: part II, experimental investigation of methods for choosing regularization parameters," *Journal of Sound and Vibration* **233** (4), 669–705 (2000).

47. Earl G. Williams, *Fourier Acoustics* (Academic Press, San Diego, California, 1999).

48. P.A. Nelson, A.R.D. Curtis, S.J. Elliot, and A.J. Bullmore, "The minimum power output of free field point sources and the active control of sound," *Journal of Sound and Vibration* **116** (3), 397–414 (1987).